Carnegie Mellon University

CARNEGIE INSTITUTE OF TECHNOLOGY

THESIS

SUBMITTED IN PARTIAL FULFILLMENT OF THE REQUIREMENTS

FOR THE DEGREE OF Doctor of Philosophy

TITLE High-throughput Screening of Alloy Oxidation Across Al-Fe-Ni and Al-Fe-Ni-Cr Composition Space

PRESENTED BY Matthew Payne

ACCEPTED BY THE DEPARTMENT OF

Chemical Engineering

ANDREW GELLMAN	4/29/16
ANDREW GELLMAN, CO-ADVISOR	DATE
JAMES MILLER	4/29/16
JAMES MILLER, CO-ADVISOR	DATE
LORENZ BIEGLER	4/19/16
LORENZ BIEGLER, DEPARTMENT HEAD	DATE

APPROVED BY THE COLLEGE COUNCIL

VIJAYAKUMAR BHAGAVATULA	4/19/16
DEAN	DATE

High-throughput screening of alloy oxidation across Al-Fe-Ni and Al-Fe-Ni-Cr composition space

Submitted in partial fulfillment of the requirements for

the degree of

Doctor of Philosophy

in

Chemical Engineering

Matthew A. Payne

B.S., Chemical Engineering, West Virginia University

Carnegie Mellon University
Pittsburgh, PA

April, 2016

Acknowledgements

I would like to extend my sincerest gratitude to everyone who has supported me as I have worked towards my Ph.D. over the last five years. I have profoundly enjoyed my time at Carnegie Mellon University, thanks in large part to all of the wonderful people I have had the opportunity to work with.

First, I would like to thank my advisors, Professor Andy Gellman and Professor Jim Miller, for providing invaluable mentorship, guidance, and advice throughout my graduate career. I would also like to thank the other members of my thesis committee, Professor John Kitchin, Professor Paul Sides, Professor Chris Pistorius, and Professor Brian Gleeson, for taking the time to offer input on my project. Thank you also to Professor Bryan Morreale for serving on my proposal committee.

Thanks as well to all of the members of the Gellman research group I have worked with over the years. I would particularly like to acknowledge Dr. Peter Kondratyuk and Dr. Aaron Reinicker for helping to train me in a number of different laboratory procedures and equipment operations.

I would additionally like to acknowledge a number of individuals from outside the research group who have made important contributions to my work. Thanks to Steve Illes and Alex Hallenbeck for assisting me with Raman spectroscopy. Thank you to Martin Oliveros, Geronimo Perez, Cristol Gouvea, Bráulio Archanjo, Carlos Senna, and Carlos Achete of Inmetro in Brazil for collecting FIB-TEM data in support of one of my projects. Thanks to Professor Yoosuf Picard for taking time on several occasions to assist me with EBSD. Thank you to Dr. Paul Jablonski of NETL for preparing bulk alloy samples for one of my studies.

I would be remiss without mentioning that none of this would have been possible without the logistical assistance of the fantastic Chemical Engineering Department support staff. Thanks particularly to Julie Tilton and Janet Latini for helping me on numerous occasions with supply purchasing, travel reimbursements, shipping, etc.

Finally, I would like to thank my family for the unwavering love and support they have provided me throughout my educational career. Thank you to my brother, Chris, my father, Jeff, and especially to my late mother, Retta, who always encouraged me to be curious about the natural world and to love science.

The work in my thesis has been funded through several different sources. Much of the work was funded by NETL through the RES Contract No. DE-FE000400. NSF CBET-0923083 supported the development of the rotatable shadow mask deposition tools used to prepare composition spread alloy films for this work. I also received tuition support for one year from the Bertucci Fellowship awarded through the Carnegie Institute of Technology, and I sincerely thank John and Claire Bertucci for their generosity in establishing this award.

Abstract

The high-temperature oxidation of multicomponent metal alloys involves complex kinetic processes that are not fully understood for many systems. As a result, prospective alloy compositions must typically be screened experimentally during the design of oxidation-resistant alloys. The comprehensiveness with which this can be done has conventionally been limited by the time required to prepare and test large numbers of single-composition alloy samples. This thesis describes the development, implementation, and assessment of a high-throughput methodology for studying the compositional dependence of alloy oxidation using composition spread alloy films (CSAFs), compact samples containing continuous, lateral gradients in composition. High-throughput analyses of the oxidation behavior of many different alloy compositions can be performed with a single CSAF by using spatially resolvable characterization techniques to probe different locations across its surface.

We have used CSAFs to study the oxidation of aluminum-iron-nickel (Al-Fe-Ni) and aluminum-iron-nickel-chromium (Al-Fe-Ni-Cr) alloys. Given a minimum "critical Al concentration", N_{Al}^{*}, these alloys preferentially form a surface layer of Al_2O_3 upon initial exposure to an oxidizing environment, which provides substantial protection to the underlying metal against further oxidation. However, the value of N_{Al}^{*} can vary as a function of both multicomponent composition and the thermochemical identity of the oxidizing environment. By oxidizing CSAFs in dry or humid air at 427 °C, we have identified continuous boundaries through the Al-Fe-Ni and Al-Fe-Ni-Cr composition spaces where phenomenological transitions in oxidation behavior occur, including N_{Al}^{*} boundaries delineating the compositional limits for protective Al_2O_3 formation. The results demonstrate the potential of CSAF-based methods to screen with unprecedented detail the effects of composition on multicomponent alloy oxidation, and offer important fundamental insights into its mechanisms.

Table of contents

List of Tables

List of Figures

Chapter 1. Introduction

1.1. Combinatorial materials science: composition spread alloy films

Experimental screening of alloy properties across composition space traditionally involves systematic testing of single-composition samples. However, the number of samples required to thoroughly screen a composition space in this way quickly becomes impractical as either the number of components or the desired composition resolution increase. Comprehensive measurement of alloy properties across composition space can be greatly expedited through the use of composition spread alloy film (CSAF) sample libraries, i.e. substrate-supported alloy films with continuous, lateral composition gradients. CSAF-based methods[1] are one subset of a diverse range of combinatorial techniques[2,3] applied increasingly in materials science to screen properties across various design-variable spaces.

CSAFs are ideal for combinatorial screening across composition space of any alloy property which can be rapidly measured at discrete locations across a surface. In the case of a ternary alloy, $A_xB_yC_{1-x-y}$ (subscripts designate atomic fractions), it is possible to create a CSAF that contains a continuous spread of all possible compositions ($x = 0 \rightarrow 1$, $y = 0 \rightarrow [1 - x]$) across the surface of a compact substrate. For example, Figure 1 shows a schematic of a full-range $A_xB_yC_{1-x-y}$ CSAF with a triangular gradient geometry. The coupling of such a CSAF with rapid, spatially resolved characterization techniques would allow high-throughput screening of composition-property relationships across the entire ternary composition space.

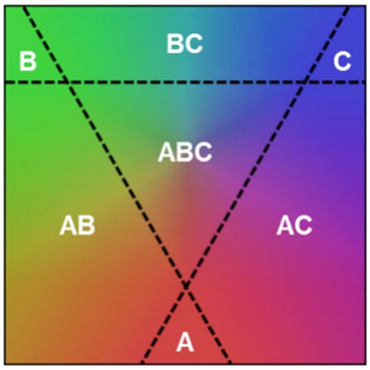

Figure 1. Schematic depiction of a ternary CSAF containing all possible compositions of $A_xB_yC_{1-x-y}$.

1.2. RSM tool for creating CSAFs

A rotatable shadow mask (RSM) CSAF deposition tool[4] was developed previously in our laboratory to create CSAFs. The tool is housed in an ultra-high vacuum (UHV) chamber (~10^{-9} Torr operating pressure) and has four confocal e-beam evaporation sources (*Mantis Deposition*) which may be used to co-deposit up to four elemental components by physical vapor deposition. Rotationally orientable, semi-circular shadow masks are positioned between each evaporator and the deposition substrate. The source-mask-substrate geometry creates line-of-sight shadowing of the flux arriving at the substrate from each evaporator and results in a linear gradient in deposition rate across the width of a band, varying from zero flux at one edge to a maximum flux at the other over a distance of ~7 mm. Figure 2(a) shows a schematic representation of the shadow masking concept as it is used to produce these gradients with the RSM tool. The direction of the gradient for each component is controlled by the orientation of its shadow mask. Using three masks oriented at 120° from one another with appropriate evaporator alignments, the RSM tool allows us to create a full-range ternary CSAF similar to that depicted in Figure 1 on a compact substrate. Figure 2(b) shows a schematic example of shadow mask orientations at which three confocal evaporators produce a CSAF geometry like that shown in Figure 1.

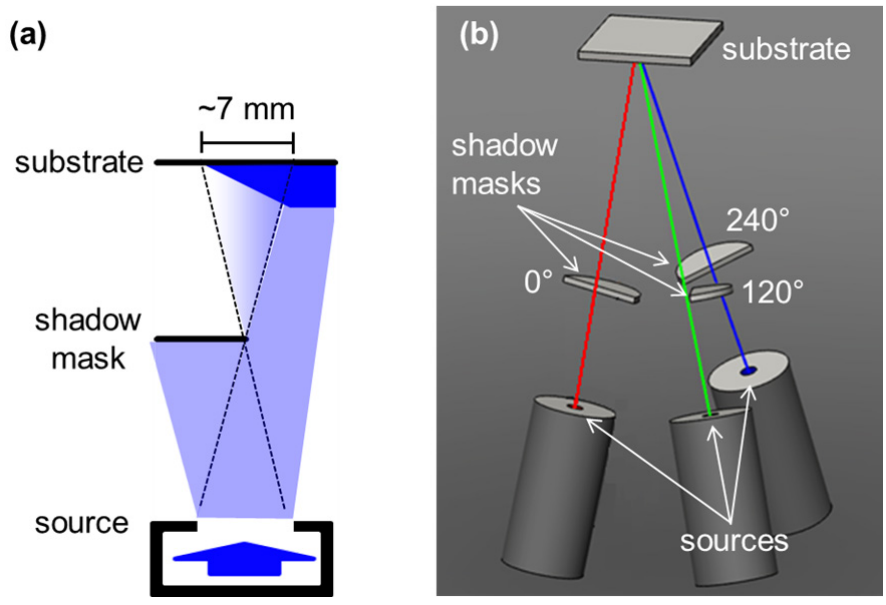

Figure 2. **(a)** Two-dimensional schematic of line-of-sight shadow masking used in the RSM tool to create deposition gradients in elemental components. **(b)** Example of shadow mask orientations and evaporator alignments for depositing a full-range ternary CSAF with a triangular gradient geometry on a substrate.

Substrates are positioned in the RSM tool with a three-axis manipulator and mounted on a holder which allows heating of the sample while temperature is monitored with a thermocouple. The chamber housing the tool is also equipped with a *Varian* ionization gauge for UHV pressure measurement, an *RBD Instruments* ion gun for sputter cleaning the substrate by Ar^+ bombardment, an *SRS* RGA-200 mass spectrometer for analysis of trace gas species, and a *Maxtek* quartz crystal microbalance (QCM) for measurement of deposition fluxes.

1.3. Alumina forming alloys: passivation and the critical Al concentration

"Alumina formers" are a type of metal alloy widely developed for oxidation resistance in high-temperature applications. An alumina former is an alloy that, under operating conditions, preferentially forms a continuous alumina (Al_2O_3) layer or "scale" at or near its surface, creating a diffusion barrier that "passivates" the underlying material against further oxidation, greatly retarding bulk oxidation.[5–9] Passivation of an alloy surface by oxide scale formation is referred to as "external oxidation", while progressive oxidation of the bulk is known as "internal oxidation".[8,10–15] Provided that a sufficiently dense and adherent scale is maintained, Al_2O_3 can remain stable and protective in oxidizing environments at temperatures $>$1280 °C.[5,7,9,13,16,17] The α-phase of Al_2O_3 is the most desirable and protective, but only forms significantly at temperatures $>$950 °C by the conversion of more rapidly growing, pseudo-stable Al_2O_3 structures.[5,18,19]

A minimum "critical Al concentration", N_{Al}^{*}, is required in an alloy for initial establishment of a continuous Al_2O_3 scale; for subcritical Al concentrations, discontinuous Al_2O_3 is formed, leaving diffusion paths that allow continuing oxidation of the bulk.[7,10,13,15,17,20] Depending on their composition, alloys with supercritical Al concentrations may develop a passivating Al_2O_3 scale either at the surface or in the subsurface beneath one or more layers of other oxides.[5,7,9–13,15,21–27] The value of N_{Al}^{*} in an alloy is highly system-dependent, and can vary as a function of both multicomponent composition and the chemical nature of the oxidizing environment.[13,16] Design of alumina-forming alloys is complicated by the fact that increasing Al content tends to mechanically compromise alloys by increasing their brittleness.[11,13,17,22,27,28] For this reason, it is desirable in structural applications to use the lowest Al content possible, while still providing adequate oxidation resistance. Therefore, rational design of any multicomponent alumina

former requires a thorough understanding of how the value of N_{Al}^{*} varies across the viable composition space and in different oxidizing environments.

1.4. AlFeNiCr-based alumina formers

Al, Fe, and Ni are three of the main components in many alumina-forming structural superalloys.[8,21,27,29–31] Cr is typically included as a fourth major component because it lowers the N_{Al}^{*} needed for establishment of an Al_2O_3 scale by what is termed a "third-element effect".[7–9,13,16,29,30] In many oxidation-resistant alloys that do not contain Al (such as traditional stainless steels), Cr is incorporated to allow protective Cr_2O_3 scale formation, but these materials exhibit oxidation resistance at >900 °C that is inferior to that of the alumina formers. This is particularly true in environments containing both H_2O and O_2 due to the formation of volatile Cr-oxyhydroxides, which can result in evaporation of the scale.[6,8,9,13,16,27,29,32,33]

AlCrFeNi-based alloys constitute a class of superalloys that behave as alumina-forming austenitic stainless steels (AFASSs) in various environments at temperatures <900 °C.[8,27,29,30] Increasing the Fe content of an AlCrFeNi-based AFASS decreases raw-material cost and increases the melting point. However, the Ni concentration must be sufficiently high to induce formation of a mechanically robust, austenitic (face-centered cubic) matrix structure.[8,27,29,30] Increasing the Fe, Al, and/or Cr content of the AFASS stabilizes a ferritic (body-centered cubic) matrix structure (observed at <912 °C in pure Fe), which induces brittleness at low temperatures and poor creep resistance at high temperatures.[8,27,29,30] As a consequence, increases in the Al and/or Cr content to improve oxidation resistance requires the replacement of some fraction of Fe with Ni in order to maintain mechanical integrity, making the resulting alloy more expensive and lowering its maximum operating temperature. Thus, as is the case with most alumina formers, accurate knowledge of the dependence of N_{Al}^{*} on composition is central to the design of AFASS alloys.

A significant limitation to determining optimum compositions of high-temperature AlCrFeNi-based alloys is that experimental studies of their properties have focused on single-composition samples.[8,27,29–31] Understanding of the influence of composition on oxidation behavior has been achieved by cumbersome methods using large numbers of samples. Efforts to rigorously maximize the potential of these alloys

must focus on development of materials models for accurate prediction of oxidation behavior as a function of composition. Such models could be significantly improved by knowledge gained from comprehensive experimental measurement of oxidation behavior across continuous, multi-dimensional composition spaces. Because this is prohibitively time consuming when using single-composition alloy samples, it is a seemingly ideal subject for high-throughput, combinatorial screening with CSAF libraries.

1.5. Wagner-Maak model for predicting the critical Al concentration

The only theoretical model commonly applied in an attempt to predict the value of N_{Al}^{*} required for an alloy to establish a passivating Al_2O_3 scale in a given environment is based on a quantitative criterion that was developed for binary alloy systems by Wagner.[34] Wagner's model describes the system in terms of one-dimensional counter-diffusion of oxygen against the alloy component that is oxidized to form the passivating scale (Al in the case of alumina-forming alloys). A significant practical drawback to Wagner's model is that it assumes that only the metal which forms the passivating scale is oxidized, i.e. the oxide of the other alloy component is not stable under the oxidizing conditions. An extension was later applied to the model by Maak in an attempt to account for more practically relevant situations where there is competitive formation of a non-protective oxide of the other metal component.[35] The assumptions and derivation of the Wagner and Wagner-Maak models have been adeptly summarized by other authors.[10,36] We review the derivation of the Wagner-Maak model here, but specifically consider a case involving oxidation of an AlM alloy, where M is a generic metal component which forms a competitive oxide MO_{β}.

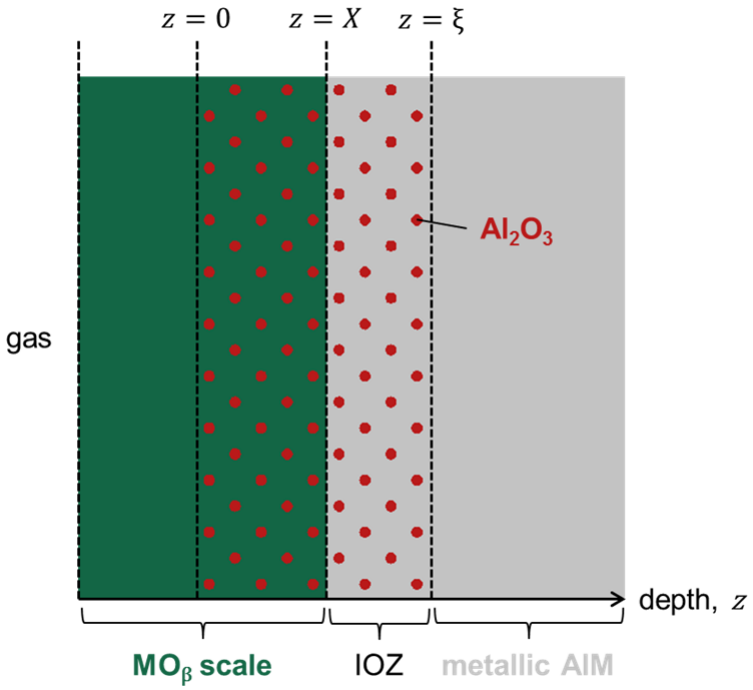

Figure 3. Schematic showing the cross section developed during internal oxidation of an AlM alloy according to the Wagner-Maak model. The original position of the interface between the alloy and gas is $z = 0$. The depth into the alloy bulk to which Al_2O_3 has been precipitated within the internal oxidation zone (IOZ) is $z = \xi$. The depth to which the IOZ has been subsequently overgrown by a competitive MO_β scale is $z = X$.

A schematic showing the cross section of an oxidized AlM alloy as described by the Wagner-Maak model is shown in Figure 3. The model predicts time-dependent advancement in depth into the alloy, z, of two distinct oxidation fronts, where $z = 0$ represents the position of the alloy/gas interface prior to any oxidation. The front at $z = \xi$ is the leading edge of the internal oxidation zone (IOZ) in which all metallic Al is assumed to have been converted to Al_2O_3 precipitates. The front at $z = X$ is the depth of inward advancement of competitive MO_β formation. For scale passivation to be possible, Al_2O_3 must be more thermodynamically stable than MO_β, i.e. Al_2O_3 must be the only oxide that can form once the local oxygen chemical potential decreases below some threshold with increasing depth into the alloy. Thus, the model is only physically meaningful if $\xi > X$. The two oxidation fronts are assumed to advance according to parabolic rate laws of the form

$$X^2 = 2k_c t \qquad (1.1)$$

$$\xi^2 = 4\gamma^2 D_O t \quad (1.2)$$

where t is time, k_c is a rate constant for the inward part of the competitive MO_β scale growth from $z = 0$, D_O is the diffusion coefficient of oxygen in metallic M, and γ is a dimensionless parameter related to a rate constant for advancement of the IOZ. The metallic M matrix is assumed to be immobile. Concentration profiles for Al and oxygen are determined by applying the one-dimensional diffusion equations

$$\frac{\partial N_O}{\partial t} = D_O \frac{\partial^2 N_O}{\partial z^2} \quad (1.3)$$

$$\frac{\partial N_{Al}}{\partial t} = D_{Al} \frac{\partial^2 N_{Al}}{\partial z^2} \quad (1.4)$$

where N_O and N_{Al} are the mole fractions of oxygen and Al, respectively, and D_{Al} is the diffusion coefficient of Al in metallic M. Based on the assumptions of the model, the boundary conditions are

$$N_{Al} = N_{Al}^{(0)} \quad \text{for} \quad z \geq 0,\ t = 0 \quad (1.5)$$

$$N_O = 0 \quad \text{for} \quad z \geq \xi,\ t > 0 \quad (1.6)$$

$$N_{Al} = 0 \quad \text{for} \quad z \leq \xi,\ t > 0 \quad (1.7)$$

$$N_O = N_O^{(s)} \quad \text{for} \quad z = X,\ t > 0 \quad (1.8)$$

where $N_O^{(s)}$ is the initial ($t = 0$) equilibrium oxygen solubility (in mole fraction) in metallic M at the alloy/gas interface ($z = 0$) and $N_{Al}^{(0)}$ is the Al concentration (mole fraction) in the bulk alloy. The boundary condition in Equation 1.5 stipulates that, prior to oxidation, the alloy is uniform in composition at all depths. The remaining boundary conditions are defined based on the positions of the oxidation fronts, X and ξ, which are time dependent. The boundary conditions in Equations 1.6 and 1.7 establish the assumptions that no

oxygen is present in the alloy at $z \geq \xi$, and that all metallic Al has been depleted at $z \leq \xi$ (by conversion to Al_2O_3). Finally, the boundary condition in Equation 1.8 states that the initial mole fraction of oxygen in M at the alloy surface is maintained at the advancing front of the MO_β scale, i.e. that the competitive oxide acts as an infinitely fast "short-circuit" route for oxygen diffusion to the MO_β/IOZ interface, allowing equilibrium with the oxygen partial pressure in the gas phase to be maintained at $z = X$ for all t. The solutions for the oxygen and Al mole fraction profiles based on Equations 1.1-1.8 are given by

$$N_{\mathrm{O}} = N_{\mathrm{O}}^{(\mathrm{s})} \frac{\mathrm{erf}(\gamma) - \mathrm{erf}\left(\frac{z}{2\sqrt{D_{\mathrm{O}} t}}\right)}{\mathrm{erf}(\gamma) - \mathrm{erf}(u)} \qquad \text{for} \qquad X \leq z \leq \xi \qquad (1.9)$$

$$N_{\mathrm{Al}} = N_{\mathrm{Al}}^{(0)} \left[1 - \frac{\mathrm{erfc}\left(\frac{z}{2\sqrt{D_{\mathrm{Al}} t}}\right)}{\mathrm{erfc}\left(\gamma\sqrt{\varphi}\right)}\right] \qquad \text{for} \qquad z \geq \xi \qquad (1.10)$$

where u and φ are defined as

$$u = \sqrt{\frac{k_c}{2D_{\mathrm{O}}}}$$

$$\varphi = \frac{D_{\mathrm{O}}}{D_{\mathrm{Al}}} \qquad .$$

The Wagner-Maak model assumes that all precipitation of Al_2O_3 occurs at ξ and, thus, that the molar fluxes of oxygen and Al arriving at ξ as a result of diffusion must satisfy this stoichiometry. This is expressed mathematically as

$$\lim_{\varepsilon \to 0}\left(-D_{\mathrm{O}}\left(\frac{\partial N_{\mathrm{O}}}{\partial z}\right)_{z=\xi-\varepsilon}\right) = \lim_{\varepsilon \to 0}\left(\nu D_{\mathrm{Al}}\left(\frac{\partial N_{\mathrm{Al}}}{\partial z}\right)_{z=\xi+\varepsilon}\right) \qquad (1.11)$$

where ν is the stoichiometric constant describing the oxygen-to-Al ratio in the Al oxide that is being formed (in an ideal case where Al is oxidized only to Al_2O_3, $\nu = 1.5$). Equation 1.11 can be solved by substituting Equations 1.9 and 1.10 to obtain

$$\frac{N_{\mathrm{O}}^{(\mathrm{S})}}{\nu N_{\mathrm{Al}}^{(0)}} = \frac{\mathrm{erf}(\gamma)-\mathrm{erf}(u)}{\mathrm{erf}(\gamma)} \frac{\mathrm{G}(\gamma)}{\mathrm{F}(\gamma\varphi^{1/2})} \qquad (1.12)$$

where $\mathrm{G}(\gamma)$ and $\mathrm{F}(\gamma\varphi^{1/2})$ are defined as

$$\mathrm{G}(\gamma) = \pi^{1/2}\gamma \exp(\gamma^2)\,\mathrm{erf}(\gamma)$$

$$\mathrm{F}\left(\gamma\varphi^{1/2}\right) = \pi^{1/2}\gamma\varphi^{1/2} \exp(\gamma^2\varphi)\,\mathrm{erfc}(\gamma\varphi^{1/2}) \qquad .$$

Equation 1.12 describes only an ongoing internal oxidation process as shown in Figure 3. The Wagner-Maak model is used to predict N_{Al}^{*} by first writing a mass balance on the Al contained in the Al_2O_3 (i.e. AlO_ν) that is precipitated at ξ of the form

$$N_{\mathrm{AlO}_\nu}\left(\frac{\mathrm{d}\xi}{\mathrm{d}t}\right) = \lim_{\varepsilon\to 0}\left(D_{\mathrm{Al}}\frac{\partial N_{\mathrm{Al}}}{\partial z}\right)_{z=\xi+\varepsilon} \qquad (1.13)$$

where N_{AlO_ν} is a constant mole fraction of AlO_ν precipitated in the IOZ. Equation 1.13 can be solved by substituting Equations 1.2 and 1.10 to obtain

$$N_{\mathrm{AlO}_\nu} = \frac{N_{\mathrm{Al}}^{(0)}}{\mathrm{F}\left(\gamma\varphi^{1/2}\right)} \qquad (1.14).$$

An “enrichment factor” of Al is defined as

$$\alpha = \frac{N_{\mathrm{AlO}_\nu}}{N_{\mathrm{Al}}^{(0)}} = \frac{1}{\mathrm{F}\left(\gamma\varphi^{1/2}\right)} \qquad (1.15).$$

The crucial assumption made by Wagner is that one can define a quantity, g^*, describing a critical volume fraction of AlO_v forming in the IOZ, above which inward oxygen diffusion will be "sufficiently reduced" (due to blocking by the Al_2O_3 precipitates) such that lateral growth begins to dominate and a continuous, passivating Al_2O_3 layer is established. Wagner related g^* to N_{AlO_v} by the expression

$$N_{\mathrm{AlO}_v} = g^* \left(\frac{V_{\mathrm{M}}}{V_{ox}}\right) \tag{1.16}$$

where V_{M} and V_{ox} are the molar volumes of M and AlO_v, respectively. Thus, N_{Al}^* is given by the value of $N_{\mathrm{Al}}^{(0)}$ which yields a value of N_{AlO_v} (Equation 1.14) that satisfies Equation 1.16. Equations 1.15 and 1.16 are combined to obtain

$$N_{\mathrm{Al}}^* = g^* \left(\frac{V_{\mathrm{M}}}{V_{ox}}\right) \mathrm{F}(\gamma\varphi^{1/2}) \tag{1.17}$$

which is posed simultaneously with Equation 1.12 (with N_{Al}^* substituted for $N_{\mathrm{Al}}^{(0)}$)

$$\frac{N_{\mathrm{O}}^{(\mathrm{s})}}{\nu N_{\mathrm{Al}}^*} = \frac{\mathrm{erf}(\gamma)-\mathrm{erf}(u)}{\mathrm{erf}(\gamma)} \frac{\mathrm{G}(\gamma)}{\mathrm{F}(\gamma\varphi^{1/2})} \tag{1.18}$$

to yield the final mathematical form of the Wagner-Maak model. Equations 1.17 and 1.18 can be solved simultaneously for any two of the variables N_{Al}^*, $N_{\mathrm{O}}^{(\mathrm{s})}$, D_{O}, D_{Al}, g^*, k_c, V_{M}, V_{ox}, ν, and γ, given appropriate values of the others. Ideally, given values for the physically defined quantities $N_{\mathrm{O}}^{(\mathrm{s})}$, D_{O}, D_{Al}, g^*, k_c, V_{M}, V_{ox}, and ν, one could solve for γ (which is defined only by the model) and then predict the value of N_{Al}^*. The strict physical picture of the Wagner-Maak model is that an AlM alloy with $N_{\mathrm{Al}}^{(0)} < N_{\mathrm{Al}}^*$ will experience ongoing internal oxidation with a morphology like that shown in Figure 3, while an alloy with $N_{\mathrm{Al}}^{(0)} \geq N_{\mathrm{Al}}^*$ will develop a passivating Al_2O_3 scale instead, i.e. that an exact value of N_{Al}^* can be defined.

1.6. Thesis objective and outline

The objectives of the work reported herein were to develop, implement, and assess high-throughput methods for screening the oxidation behavior of Al-Fe-Ni and Al-Fe-Ni-Cr alloys across composition space using combinatorial CSAF libraries prepared using the RSM tool. Our particular interest was to determine whether a CSAF which was exposed to a given oxidizing environment could be used to measure the value of N_{Al}^{*} as a function of multicomponent composition. Experimental constraints associated with the RSM tool limit the maximum achievable CSAF thickness to ~100 nm. This, in turn, has forced us to limit the temperature of the oxidizing environments in our studies to 427 °C (experimental issues begin to arise at higher temperatures due to film instability and the increased rate of oxidation). With regards to practical applications, oxidation at 427 °C is very transient (i.e. early-stage) compared to that typically considered for alumina formers, where bulk alloys may be oxidized in environments at 600 to 1200 °C for hundreds or thousands of hours, sometimes resulting in passivation mechanisms with total oxide layer thicknesses >10 μm.[7,15,22,27] In principle, the ability to prepare much thicker CSAFs would allow high-throughput methods similar to ours to be applied to studies of alloy oxidation at much higher temperatures of direct industrial relevance, but this is beyond our current capabilities. Accepting this limitation, the following Chapters explore the potential of CSAF-based methods for high-throughput screening of the effects of alloy composition on the oxidation of alumina-forming alloys.

Chapter 2 describes a model developed to estimate the composition of CSAFs produced with the RSM tool as a continuous function of real-space position on their substrates. This is critical for determining the alloy compositions corresponding to any set of property measurements made in real space at discrete locations across a CSAF surface. The model is based on the unique characteristics of the gradients of the alloy components produced by the RSM tool (see Figure 2), and is used in the work described in Chapters 3, 4, 5, and 6.

Chapter 3 describes a study of the oxidation of $Al_xFe_yNi_{1-x-y}$ CSAFs ($x = 0 \rightarrow 1$, $y = 0 \rightarrow [1 - x]$) in dry air at 427 °C. Energy-dispersive X-ray spectroscopy (EDX), Raman spectroscopy, and X-ray photoemission spectroscopy (XPS) depth profiling were used to characterize oxidation behavior across the entire $Al_xFe_yNi_{1-x-y}$ composition space. Four phenomenologically different types of oxidation behavior were identified for different CSAF composition ranges, and a continuous N_{Al}^{*} boundary was identified,

separating compositions which formed a passivating Al_2O_3 from those that did not. The content of Chapter 3 is also described in published work.[37]

Chapter 4 describes a study of the oxidation of $Al_xFe_yNi_{1-x-y}$ CSAFs ($x = 0 \rightarrow 1$, $y = 0 \rightarrow [1 - x]$) in a 10% H_2O/air mixture at 427 °C, with the primary goal of comparing the results to those from Chapter 3 to determine how humidity in the oxidizing environment influences the value of N_{Al}^* across $Al_xFe_yNi_{1-x-y}$ composition space. Four types of oxidation behavior were identified, and found to be qualitatively identical to those observed on $Al_xFe_yNi_{1-x-y}$ CSAFs oxidized in dry air. However, across much of composition space, the N_{Al}^* boundary for oxidation in the humid air was shifted to higher Al contents than for oxidation in dry air. Physical insights from the observed differences in N_{Al}^* are considered using a modified version of the Wagner-Maak model introduced in Chapter 1.5. The content of Chapter 4 is also described in published work.[38]

Chapter 5 describes work performed to critically assess two aspects of the CSAF-based methodology used for our high-throughput studies of $Al_xFe_yNi_{1-x-y}$ oxidation in Chapters 3 and 4: the sensitivity of CSAF oxidation behavior to variations in composition and the differences between the oxidation behavior of CSAFs and that of bulk alloys. This was done by focusing specifically on Al_xFe_{1-x} and Al_xNi_{1-x} oxidation in dry air at 427 °C. Transitions between phenomenologically distinguishable types of oxidation behavior were found to occur over CSAF composition ranges of <2 at.%. The oxidation of Al_xFe_{1-x} CSAFs was very similar to that of bulk Al_xFe_{1-x} alloys, but some minor differences between CSAF and bulk behavior were observed for Al_xNi_{1-x}. The content of Chapter 5 is also described in work submitted for publication.[39]

Chapter 6 describes the development of methods for preparing, characterizing, and collecting data across quaternary CSAFs prepared with the RSM tool. This was done by preparing an $(Al_xFe_yNi_{1-x-y})_{\sim 0.8}Cr_{\sim 0.2}$ CSAF and studying its oxidation in dry air at 427 °C to identify N_{Al}^*. For most fixed Fe-to-Ni ratios, the value of N_{Al}^* was found to be significantly lower in the $(Al_xFe_yNi_{1-x-y})_{\sim 0.8}Cr_{\sim 0.2}$ CSAF than in $Al_xFe_yNi_{1-x-y}$ CSAFs oxidized in dry air at 427 °C (described in Chapter 3). The content of Chapter 6 is also described in work submitted for publication.[40]

Chapter 7 provides an overall summary of the thesis and recommendations for follow-up work.

Chapter 2. Composition distribution model for CSAFs produced with the RSM tool

To facilitate our ability to perform high-throughput screening of alloy properties across composition space using CSAFs produced by the RSM tool, a composition distribution model (CDM) was developed to describe CSAF composition as a continuous function of real-space position. The CDM provides a quantitative basis for estimating composition continuously at all locations across a CSAF from a set of discrete measurements, and is based on simplifying assumptions regarding the evaporative flux profiles produced by the RSM tool (see Figure 2). Specifically, for each CSAF component, i, the CDM describes the relative molar amount of i per unit surface area, A_i, accumulated across the substrate as the height of a simple geometric surface above the plane of the substrate. For shadow-masked components, previous work from our group has shown[4] that A_i is well approximated by a "linear wedge", as shown in Figure 4.

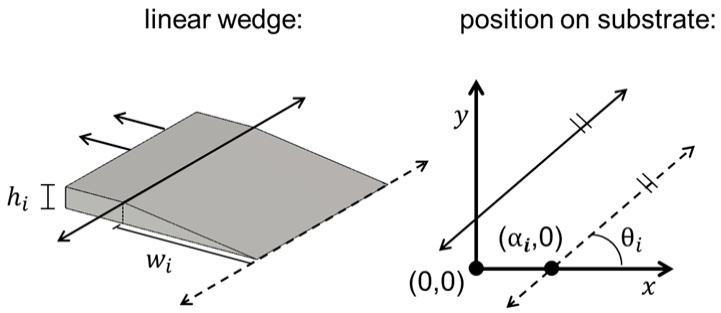

Figure 4. Linear wedge surface (left) used to in the CDM to predict the molar amount across the substrate of any alloy component deposited from a shadow-masked source in the RSM tool. The wedge is defined relative to an (x, y) plane on the substrate surface (right) using the four geometric parameters h_i, w_i, α_i, and θ_i. The relative molar amount of the component is modeled as the height of the wedge surface above the plane defined by the substrate surface.

Uniquely describing a linear wedge relative to the plane of the substrate requires 4 geometric parameters. We define these parameters as h_i, w_i, α_i, and θ_i based on an orthogonal (x, y) coordinate system used to define position across the surface of the substrate. The geometric significance of each parameter is shown in Figure 4: h_i (unitless) is the maximum height of the wedge, w_i (mm) is the width of the wedge, α_i (mm) defines the wedge position as the intersection of the zero-flux edge with the x-axis, and θ_i (degrees) describes the wedge orientation as the angle of rotation of the zero-flux edge with

respect to the x-axis. Given these definitions, $A_i(x,y)$ can be calculated for any specified values of h_i, w_i, α_i, and θ_i as

$$A_i(x,y) = \begin{cases} \begin{cases} h_i, & y < Y_{m,i} \\ h_i\left(\frac{y-Y_{0,i}}{Y_{m,i}-Y_{0,i}}\right), & Y_{m,i} \le y \le Y_{0,i}\,,\ \cos\theta_i < 0 \\ 0, & y > Y_{0,i} \end{cases} \\ \begin{cases} 0, & y < Y_{0,i} \\ h_i\left(\frac{y-Y_{0,i}}{Y_{m,i}-Y_{0,i}}\right), & Y_{0,i} \le y \le Y_{m,i}\,,\ \cos\theta_i > 0 \\ h_i, & y > Y_{m,i} \end{cases} \end{cases} \qquad (2.1)$$

where

$$Y_{0,i}(x) = (x-\alpha_i)\tan\theta_i$$

$$Y_{m,i}(x) = \frac{w_i}{\cos\theta_i} + (x-\alpha_i)\tan\theta_i \quad .$$

Alternatively, one or more components in the RSM tool may be deposited with the shadow mask removed (or rotated continuously at a constant rate). In this case, A_i should be essentially constant across the substrate. However, previous work from our group has shown[4] that the A_i across a substrate of material deposited from an unmasked source actually varies slightly, but with an approximately planar trend (arising because the evaporators in the RSM tool are tilted at 15° relative to the substrate normal). For this reason, we fit the A_i of any unmasked component in the CDM as the height of a plane above the substrate surface, described by 3 geometric parameters. Relative to an orthogonal (x,y) coordinate system used to define position on the surface of the substrate, we defined these parameters as $A_i(1,11)$, $A_i(11,11)$, and $A_i(6,1)$, i.e. the values of A_i at three (x,y) points on the substrate. For any specified values of $A_i(1,11)$, $A_i(11,11)$, and $A_i(6,1)$, $A_i(x,y)$ can then be calculated as

$$A_i(x,y) = \frac{(x-1)a+(y-11)b+100A_{\mathrm{Cr}}(1,11)}{100} \qquad (2.2)$$

where

$$a = 10\big(A_i(11,11) - A_i(6,1)\big) - 10(A_i(1,11) - A_i(6,1))$$

$$b = 5\big(A_i(1,11) - A_i(6,1)\big) + 5(A_i(11,11) - A_i(6,1)) \quad .$$

Upon defining $A_i(x,y)$ for each of j total components, the mole fraction of each component in the CSAF, N_i, can be trivially calculated as

$$N_i(x,y) = \frac{A_i(x,y)}{\sum_j A_j(x,y)} \quad (2.3).$$

For a CSAF created in the RSM tool with m alloy components deposited from a shadow-masked source ($A_i(x,y)$ described by Equation 2.1) and u components deposited from an unmasked source ($A_i(x,y)$ described by Equation 2.2), the values of $(4m + 3u)$ parameters are required to evaluate $N_i(x,y)$ across the CSAF surface using the CDM. Parameter values defining a best-fit CDM for a given CSAF can be determined by performing a least-squares regression of N_i values predicted by the CDM, N_i^{CDM} (defined by Equation 2.3), compared to N_i values measured at a set of discrete locations, N_i^{msrd}. The accuracy of best-fit CDMs in describing $N_i(x,y)$ for CSAFs produced with the RSM tool is about ±2 at.%, as will be discussed on a case-by-case basis for the studies described in the following Chapters.

Chapter 3. $Al_xFe_yNi_{1-x-y}$ CSAF oxidation in dry air at 427 °C

3.1. Introduction

In the work described in this Chapter, we use $Al_xFe_yNi_{1-x-y}$ CSAF libraries to develop an experimental methodology for high-throughput assessment of oxidation across alloy composition spaces. Basic types of oxidation behavior relevant to AFASS alloys and other alumina formers of interest can be observed in the ternary $Al_xFe_yNi_{1-x-y}$ system. Of particular interest are the $Al_xFe_yNi_{1-x-y}$ composition regions that establish a protective Al_2O_3 scale in a given oxidizing environment. $Al_xFe_yNi_{1-x-y}$ CSAFs spanning all of ternary composition space ($x = 0 \rightarrow 1$, $y = 0 \rightarrow [1 - x]$) were created and used for high-throughput, oxidation experiments. The CSAFs were prepared targeting a triangular gradient geometry, like that shown in Figure 1. Experimental constraints limited the thickness of the CSAFs to ~100 nm. Therefore, we have focused on the early oxidation mechanisms occurring in CSAFs exposed to dry air at 427 °C for ≤4 h (relatively mild conditions for alumina formers). The goal was to locate boundaries between composition regions that exhibit different types of internal and external oxidation behavior, particularly the boundary defining the critical Al concentration for establishment of a passivating Al_2O_3 scale, N_{Al}^{*}. Provided an Al_2O_3 scale is initially established in an alumina former, further oxidation by scale thickening occurs with a slow parabolic growth rate.[7,13,19] Using AlNi alloys, Pettit showed that a second critical Al concentration, N_{Al}^{**}, is required for an alloy to supply sufficient Al to maintain this slow parabolic growth and ensure long-term scale stability, but his findings suggest that N_{Al}^{**} is only greater than N_{Al}^{*} at temperatures >630 °C.[41] Thus, the limiting edge of the composition range for which an Al_2O_3 scale is present on an $Al_xFe_yNi_{1-x-y}$ CSAFs after oxidation in dry air at 427 °C should directly represent the continuous N_{Al}^{*} boundary through composition space.

The location of the N_{Al}^{*} boundary in composition space was probed by performing spatially resolved characterizations of oxidized $Al_xFe_yNi_{1-x-y}$ CSAFs which were able to reveal whether or not an Al_2O_3 scale was present at different locations, i.e. whether the Al concentration in the CSAF at that location was supercritical or subcritical. Initial characterization of $Al_xFe_yNi_{1-x-y}$ CSAF composition gradients was performed in a scanning electron microscope (SEM) by automated composition mapping using EDX. For CSAFs exposed to dry air at 427 °C, visual analyses of oxidation-induced color changes

on their surfaces were sufficient to identify oxidation behavior boundaries in real-space, which were converted to boundaries in composition space using a CDM (see Chapter 2) fit based on the EDX composition mapping. Additional EDX measurements were used to measure oxygen uptake across the CSAFs following exposure to dry air at 427 °C. Raman spectroscopy was used to identify oxide phases formed in different regions of a CSAF. Finally, XPS depth profiles were performed at select locations (i.e. compositions) on a CSAF to elucidate specific oxidation behavior by providing information on the cross-sectional composition of metallic and oxidized components. The combination of these techniques allows a single $Al_xFe_yNi_{1-x-y}$ CSAF to be used for comprehensive characterization of early oxidation behavior across a ternary composition space for a given set of oxidation conditions. We find that, after 4 h of exposure to dry air at 427 °C, $Al_xFe_yNi_{1-x-y}$ composition space can be subdivided into four regions exhibiting different types of oxidation behavior: 1) surface passivation by exclusive Al_2O_3 scale formation; 2) passivation by formation of a continuous subsurface Al_2O_3 scale; 3) passivation by a subsurface Al_2O_3 scale beneath a variable-thickness α-Fe_2O_3 surface layer; and finally, 4) a region that exhibits internal oxidation.

3.2. Experimental methods

3.2.1. $Al_xFe_yNi_{1-x-y}$ CSAF preparation

Two $Al_xFe_yNi_{1-x-y}$ CSAFs were deposited using the RSM tool[4] (described in Chapter 1.2). The CSAFs were deposited on the 14×14 mm^2 surfaces of 2.5 mm-thick, polycrystalline-Mo substrates purchased from *SPAWR Industries* and polished to a root mean squared roughness <1.5 nm by *Valley Design Corp Operations*. Before each CSAF deposition, the substrate was cleaned by gently swabbing the deposition surface with isopropyl alcohol and then loaded into the CSAF deposition chamber. The chamber was then evacuated and the substrate was annealed at 477 °C for 2 h prior to bake-out. Once the post-bake-out operating pressure was achieved, the deposition surface was sputtered by a defocused, 2 kV Ar^+ beam (~5 μA sample current) for 20 min to remove any oxide or adsorbed contaminants and the substrate was annealed at 477 °C for 1 h and allowed to cool to room temperature in UHV. Another 20 min of Ar^+ sputtering was performed immediately preceding CSAF deposition. Appropriate e-beam evaporator power settings were determined by calibrating component fluxes using

QCM measurements of deposition rate. The highest achievable deposition rate for Ni in regions of maximum flux was ~0.2 nm/min (~3×10^{-9} mol/cm^2/min). Evaporator power settings for Al and Fe were chosen to yield molar deposition rates similar to that of the Ni. The $Al_xFe_yNi_{1-x-y}$ CSAFs were each deposited for 500 min, producing a film thickness of ~100 nm. Substrate temperature increased to ~50 °C during deposition due to radiative heating by the evaporation sources. Following deposition, the substrate was annealed in UHV for 2 h at 427 °C to crystallize the CSAF and then cooled to ambient temperature in UHV. The chamber was then vented and the sample was transferred to a *Tescan* Vega3 SEM operated at ~10^{-4} Torr for composition gradient mapping using EDX. The only oxidizing environment experienced by the CSAF prior to its preliminary characterization was ambient air for the period of ~15 min required for its transfer from the deposition chamber into the SEM.

3.2.2. EDX mapping of $Al_xFe_yNi_{1-x-y}$ CSAF composition gradients

Initial mapping of the $Al_xFe_yNi_{1-x-y}$ CSAF composition gradients was performed in the SEM by EDX using an *Oxford Instruments* X-max 80 mm^2 detector. The samples were mounted on a computer-controlled stage allowing automated, high-throughput measurements. Using the software package INCA Energy, spectra were acquired from a 13×13 square grid of points spanning the 12×12 mm^2 region in the middle of the 14×14 mm^2 substrate (169 total points). A secondary electron image (1000× magnification) was captured at each location and inspected to ensure that no foreign debris or other abnormalities were present. EDX spectra were obtained from 0-10 keV (10 eV binning) by rastering the 11.24 kV SEM beam over a 50×50 μm^2 area centered on each grid point and measuring emitted X-rays for 40 s livetime while operating at ~45% detector deadtime. The 50×50 μm^2 size was chosen to minimize artifacts arising from any small defects or microstructures while still maintaining sufficient resolution in composition space (the concentration of each component in the CSAF changes by <1 at.% across 50 μm). The CSAF thickness was ~100 nm, but the characterization depth of 11.24 kV EDX in Al, Fe, Ni, and Mo is >300 nm.[42] Thus, conventional quantification of the EDX spectra was inappropriate, as the accuracy of the algorithm built into INCA Energy is critically dependent on the assumption that the entire sampled volume is homogenous. In reality, the sampled volumes on the CSAFs consist of two distinct layers: a roughly homogenous $Al_xFe_yNi_{1-x-y}$ film on top of an effectively infinite thickness of Mo. The *Oxford Instruments*

software package INCA ThinFilmID accounts for the effects of layered samples and was used to quantify the EDX spectra obtained in INCA Energy to determine accurate CSAF compositions. Three separate EDX measurements of CSAF composition were made at each point and the results were averaged to reduce noise. The results of the initial composition mapping were also used to determine parameter values describing a best-fit CDM for each $Al_xFe_yNi_{1-x-y}$ CSAF (see Chapter 2), where A_{Al}, A_{Fe}, and A_{Ni} were each modeled using a linear wedge (Figure 4, Equation 2.1).

3.2.3. Oxidation and visual analysis of $Al_xFe_yNi_{1-x-y}$ CSAFs

Elevated-temperature oxidation of the two $Al_xFe_yNi_{1-x-y}$ CSAFs was performed by placing the samples in a ceramic boat in the center of a quartz tube furnace (~60 cm long, 2 cm diameter) with one end open to atmosphere and the other end connected to a cylinder of lab-grade dry air. A regulator was used to apply a continuous flow of ~1 slpm of the dry air through the furnace. The furnace and boat were preheated to 427 °C with the air flowing. The CSAF samples were then positioned in the boat such that only the non-CSAF side of the substrate was in contact with the boat. It takes ~5 min for the temperature of a loaded CSAF to rise to within 20 °C of the furnace temperature. After total exposure times, t_{ox}, of 1, 2, and 4 h, the samples were removed from the furnace and the non-CSAF sides were placed in contact with aluminum foil to quickly dissipate heat, cooling them to near room temperature in ~2 min. The CSAFs were then photographed and loaded into the SEM for further characterization.

Composition-dependent changes in the surface coloration of $Al_xFe_yNi_{1-x-y}$ CSAFs occur during oxidation, and we have used visual analysis of this phenomenon as a tool to identify boundaries between regions exhibiting different oxidation behavior. Using images of the oxidized CSAF surfaces after $t_{ox} = 4$ h, real-space locations of boundaries between visually distinct regions can be converted to composition space boundaries using the best-fit CDMs. Visual analysis, in combination with spectroscopic characterization techniques that revealed the phenomenological significance to visually identifiable regions, was used to determine continuous boundaries between regions of ternary composition space having different oxidation behavior.

3.2.4. EDX, Raman, and XPS characterization of oxidized $Al_xFe_yNi_{1-x-y}$ CSAFs

Alloy oxidation kinetics are often studied by measuring weight gain per unit surface area of the alloy as a function of time using bulk, single-composition alloy samples.[7,21,22,27,43] Because spatially resolved gravimetric analysis of CSAFs is infeasible, a high-throughput, spatially resolved, EDX-based method was developed as an alternative for measuring oxygen uptake across the CSAFs. For an SEM accelerating voltage of 20 kV, the effective probing depths in Al, Fe, Ni, and Mo are all about an order of magnitude greater than the ~100 nm thickness of the CSAFs.[42] As a result, Mo accounts for >85% of the raw signal in the 20 kV EDX spectra obtained from the $Al_xFe_yNi_{1-x-y}$ CSAFs on Mo substrates. As will be shown later, the depth of oxygen penetration after $t_{ox} = 4$ h does not exceed the thickness of the CSAFs, even in the most heavily oxidized regions. Since the thickness of the layer containing Al, Fe, Ni, and oxygen is much smaller than the total sampled thickness, it is reasonable to assume that the oxygen EDX signal will scale linearly with the amount of oxygen present without significantly affecting the Mo signal and, therefore, that the total molar oxygen content at any point in the CSAF is proportional to the oxygen signal scaled by the Mo signal. Thus, the ratio of O-to-Mo EDX signals serves as a metric that is proportional to the total oxygen mass per unit surface area traditionally measured using gravimetric analysis of bulk alloy samples. Using this EDX-based method, the local oxygen content, $C_O(x, y)$, was measured quantitatively at $t_{ox} = 0$, 1, 2, and 4 h across the two $Al_xFe_yNi_{1-x-y}$ CSAFs. The distribution of measurement points across each CSAF was chosen with guidance from the best-fit CDM to ensure a high-density sampling of most of ternary composition space. The CSAF compositions at the selected points were measured using the same EDX/ThinFilmID procedures as were used for the initial mapping of the CSAF composition gradients. After this initial measurement of the CSAF composition at each point using EDX at 11.24 kV, C_O was determined at each point from additional EDX spectra obtained with the SEM accelerating voltage increased to 20 kV, as described above. After $t_{ox} = 0$, 1, 2, and 4 h, three independent measurements of C_O were made at each location and averaged to reduce noise. In this way, oxygen uptake was determined with high resolution across $Al_xFe_yNi_{1-x-y}$ composition space.

A Raman spectrum was obtained at 61 locations across one of the oxidized CSAFs ($t_{ox} = 4$ h) to identify specific oxide phases present. A *Horiba-Jobin Yvon* LabRam HR Raman system, equipped with a 200 mW green laser (532 nm wavelength) which was filtered to ~50% intensity, was used for the

measurements. The aperture size was 100 μm and an *Olympus* BX-30-LWD confocal microscope with a 50× long working distance objective was used for focusing, resulting in a beam diameter of ~30 μm at the surface. Initial calibration of the CCD detector was performed using Si. The Raman-shift spectrum in the range 100-1500 cm^{-1} was obtained at each location on the CSAF by averaging ten consecutive acquisitions of 5 s each. A de-spike procedure was run on each spectrum using NGSLabSpec software. The resulting spectra indicated the presence of α-Fe_2O_3, NiO, and $NiFe_2O_4$ in various regions across the oxidized CSAF.

XPS depth profiling was used to determine the cross-sectional composition through the CSAF used for the Raman analysis at select sites of interest. XPS depth profiling is a destructive technique involving alternating cycles of XPS measurements and removal of surface material from the measurement site by Ar^+ etching. This allows the composition of thin (~1 nm) layers to be determined as a function of depth into a sample. The XPS studies were performed using a *ThermoFisher* ThetaProbe instrument (Al K_α X-rays, ~200 μm measurement spot size, hemispherical energy analyzer). Survey scans across a binding energy range of 100-1200 eV with a 0.25 eV step size, 0.2 s dwell time, and 200 eV pass energy were used to confirm that no unexpected chemical species were present on the CSAF. Subsequent scans used for quantification were obtained over 10-14 eV ranges around the non-overlapping Al 2s, Fe $2p_{1/2}$, Ni $2p_{3/2}$, and Mo $3p_{3/2}$ peaks. These scans were performed with a 0.05 eV step size, 0.2 s dwell time, and 100 eV pass energy. Between each set of measurements, the CSAF was uniformly excavated across an ~16 mm^2 region containing the XPS analysis site(s) by rastering a focused Ar^+ beam operated at 3 kV and 1 μA with a backfilled Ar pressure of ~4×10^{-3} Pa. *Thermo* Avantage processing software was used to subtract XPS backgrounds (using the *Thermo* "Smart" background), fit peaks (using a fixed 30% Lorentzian/Gaussian shape), and calculate peak areas. Wagner sensitivity factors were used to adjust peak areas to determine relative atomic composition. Oxidation of the metal species increased their peak binding energies by ~2 eV. In cases where chemical shifts caused peak splitting due to the presence of both oxidized and metallic states of one of the components, the ratio of oxidized to metallic species was estimated by fitting the spectra using two peaks with the metallic peak location and FWHM held constant for all spectra from that measurement site. Further assignment of the oxide peaks to specific oxidation states was not attempted.

3.3. Results

3.3.1. Spatial maps of $Al_xFe_yNi_{1-x-y}$ CSAF composition gradients

A thorough quantification of the composition distribution across a CSAF is required for translation of real space analysis locations on the CSAF into composition space. EDX was used to map $Al_xFe_yNi_{1-x-y}$ composition across a 12×12 mm^2 region in the center of each of the two CSAFs. Figure 5 shows atomic composition contours of Al, Fe, and Ni in real space on one of the CSAFs. The contours are fit to spatially resolved EDX measurements of composition taken on a 13×13 grid of points. The corresponding set of 169 measured $Al_xFe_yNi_{1-x-y}$ compositions is plotted in the ternary composition diagram of Figure 5. Because CSAFs are comprised of continuous composition gradients, any point in composition space located between any three of the sampled points must be present at some location on the CSAF. All of $Al_xFe_yNi_{1-x-y}$ composition space with Al content, $x < 0.95$ was present within the 12×12 mm^2 region that was analyzed. Compositions with $x > 0.95$ did not fall within this region of the CSAF, but were present closer to the edge of the 14×14 mm^2 substrate. Despite slightly different gradient geometries, full coverage of composition-space was also obtained with the second CSAF.

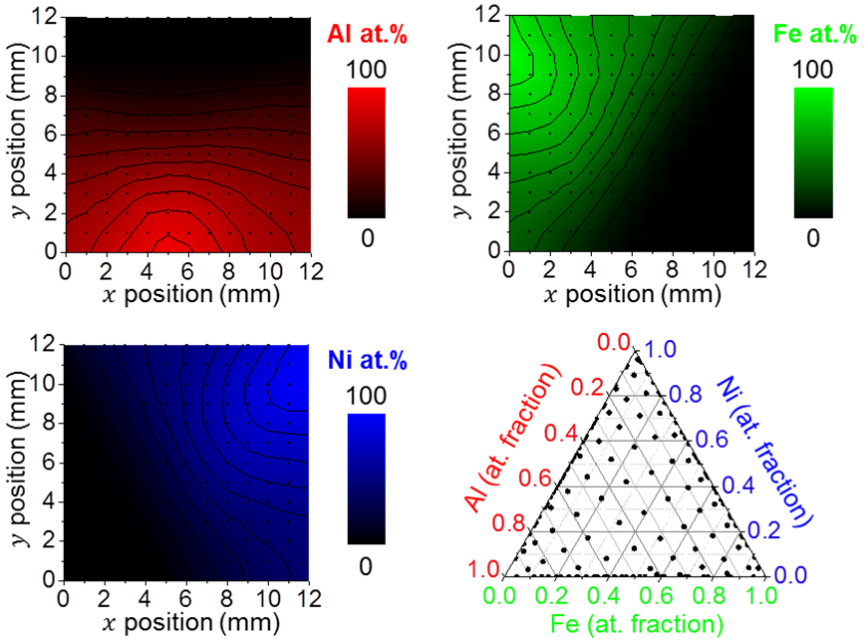

Figure 5. Contour plots of the concentrations of Al, Fe, and Ni in one of the CSAFs as obtained from EDX measurements taken on a 13×13 grid of real-space locations over a 12×12 mm^2 area centered on the 14×14 mm^2 substrate. The ternary composition diagram shows the discrete $Al_xFe_yNi_{1-x-y}$ compositions measured at the 169 points. Nearly complete coverage of the composition space is demonstrated. Compositions from 95-100 at.% Al are also present on the substrate, but fell just outside the plotted region.

EDX is most quantitatively accurate when the spectral-processing routine is calibrated using a known standard that is as close as possible in composition to the unknown. Because we measured $Al_xFe_yNi_{1-x-y}$ compositions spanning the entire ternary composition space, selection of a single-composition standard was impossible. Therefore, EDX spectra were processed without any sample-specific calibration, and indirect comparisons have been used to assess the quantification accuracy. EDX-measured binary compositions were found to agree to within 2 at.% with bulk samples of $Al_{0.05}Ni_{0.95}$, $Al_{0.10}Ni_{0.90}$, $Fe_{0.15}Ni_{0.85}$, and $Fe_{0.30}Ni_{0.70}$ alloys. Based on three independent sets of EDX composition measurements taken at 301 locations on one of the CSAFs, the average measurement-to-measurement variability for each component was found to have a standard deviation of $\sigma = 1$ at.%. Rough estimates of bulk composition obtained from XPS depth profiles performed on unoxidized CSAFs (annealed for 2 h after deposition at 427 °C and cooled to room temperature in UHV) agree with EDX-measured composition to ±5 at.% for each component. These depth profiles also confirmed that the layering

assumption used for quantification in INCA ThinFilmID is reasonable; i.e. that the $Al_xFe_yNi_{1-x-y}$ composition is homogenous across the CSAF thickness and no significant interdiffusion between the CSAF and the Mo substrate occurs as a result of annealing.

3.3.2. Visual identification of $Al_xFe_yNi_{1-x-y}$ CSAF oxidation behavior boundaries

Visually observable changes in the coloration of $Al_xFe_yNi_{1-x-y}$ CSAFs become evident during their oxidation. Figure 6(a, b) shows images of one of the CSAFs taken at $t_{ox} = 0$ and $t_{ox} = 4$ h in dry air at 427 °C. The most significant coloration changes are observed on the upper region of the CSAF at low-Al compositions, while little change is observed across a large fraction of the Al-rich lower region of the CSAF. The majority of the visual transformation had occurred by $t_{ox} = 1$ h with only minor additional change observable after $t_{ox} = 2$ and 4 h. Figure 6(c) shows an image of the second CSAF after $t_{ox} = 4$ h and reveals the high degree of reproducibility of the visual patterns. Bearing in mind the fact that the positions of the CSAF gradients on the two Mo substrates are not identical, the reproducibility of the various features on the oxidized CSAFs is remarkable.

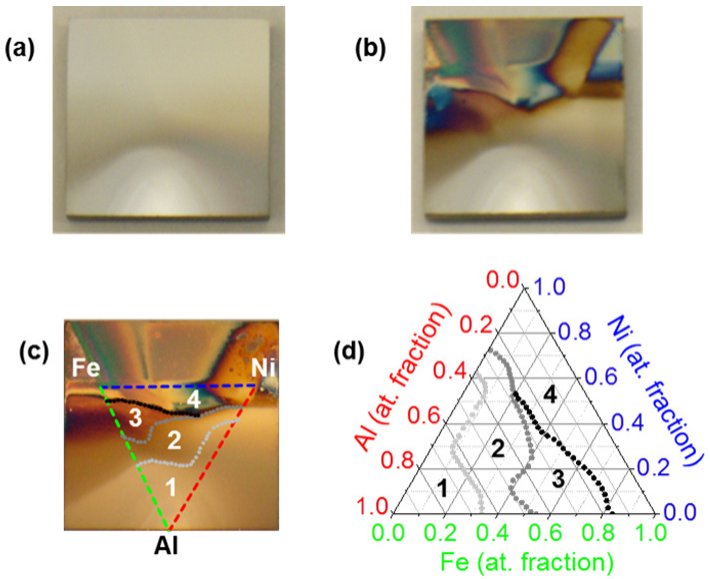

Figure 6. **(a)** Image of one of the $Al_xFe_yNi_{1-x-y}$ CSAFs after deposition, UHV annealing at 427 °C for 2 h, and brief (~15 min) exposure to atmosphere under ambient conditions. **(b)** Image of the same CSAF after oxidation in dry air for 4 h at 427 °C. **(c)** Cropped image (different lighting) of the second, identically oxidized $Al_xFe_yNi_{1-x-y}$ CSAF showing boundaries identified in real-space around "visually distinct" regions. The estimated location of the ternary triangle based on the best-fit CDM is also shown for reference. **(d)** Boundaries plotted in composition space via the best-fit CDM.

The $Al_xFe_yNi_{1-x-y}$ composition at any point on an oxidized CSAF can be estimated by transforming its real-space location into composition space using the best-fit CDM fit to the sample based on its initial composition mapping (see Chapter 2). Likewise, visually observable boundaries can be transformed into continuous composition-space boundaries. Three visually observable boundaries were identified on each of the two CSAFs after $t_{ox} = 4$ h delineating four composition regions that were common to both samples. Figure 6(c, d) shows these real-space boundaries defined on one of the CSAFs and in composition space. The boundaries separate four increasingly discolored regions of the CSAFs, labeled 1-4. The boundary between regions 1 and 2 becomes difficult to discern visually as the Ni-to-Fe ratio increases, but can be readily observed in SEM contrast, which was used to verify that the appropriate trajectory of this boundary was identified (this will be discussed in more detail in Chapter 4.3.2). EDX, Raman, and XPS analyses were used to correlate the boundaries between these regions with transitions between different types of oxidation behavior.

Visual analysis of CSAFs has the potential to allow rapid, high-throughput mapping into composition space of phenomena causing reproducible and distinguishable optical changes in CSAFs, but it is limited by the accuracy of the CDM used to translate from real space into composition space. The accuracy of one of the best-fit CDMs was analyzed by comparing EDX-measured compositions at interpolated, real-space locations to the CDM predictions. At 220 such locations, the CDM-predicted atomic fractions of each CSAF component i, N_i^{CDM}, were compared to the EDX-measured fractions, N_i^{msrd}, and the differences, $\varepsilon_i = N_i^{CDM} - N_i^{msrd}$, were calculated. The average differences were $\bar{\varepsilon}_{\mathrm{Al}} = 0.5$ at.%, $\bar{\varepsilon}_{\mathrm{Fe}} =$ -0.2 at.%, and $\bar{\varepsilon}_{\mathrm{Ni}} =$ -0.3 at.% with standard deviations of $\sigma_{\mathrm{Al}} = 1.8$ at.%, $\sigma_{\mathrm{Fe}} = 1.7$ at.%, and $\sigma_{\mathrm{Ni}} = 1.6$ at.%. We believe that the fit of the CDM to the real space composition distribution is the most substantial source of error in estimating the composition at any location on the surface. Error arising from determination of the real space coordinates of visual features from images is estimated to be ±0.1 mm (corresponding to <2 at.% for each component) and should be comparable to the CDM error. As illustrated in Figure 6(b, c), the two $Al_xFe_yNi_{1-x-y}$ CSAFs developed very similar visual appearances after $t_{ox} = 4$ h. Figure 7(left) shows a comparison of the composition-space boundaries separating the four regions on the two CSAFs shown in Figure 6(b, c). The results appear to be reproducible to within the expected accuracy of the visual analyses. Figure 7(right) shows an average of the two sets of boundaries

which will be used as the basis for subsequent discussion of the composition-dependent transitions between different types of oxidation behavior in dry air at 427 °C.

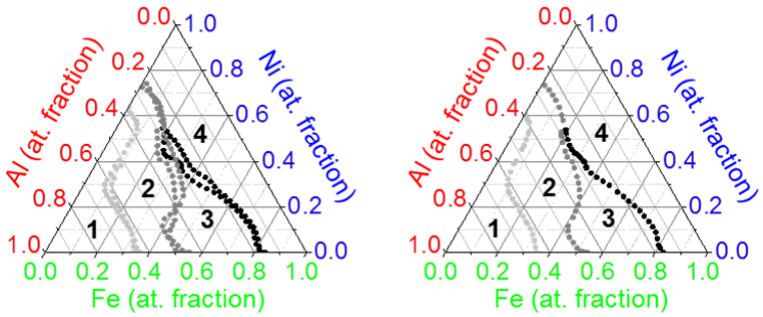

Figure 7. Left: Comparison of composition-space boundaries defining similar, visually distinguishable regions on the two oxidized $Al_xFe_yNi_{1-x-y}$ CSAFs as determined by visual analysis. **Right:** Average position of the three boundaries.

3.3.3. EDX measurement of oxygen uptake during $Al_xFe_yNi_{1-x-y}$ CSAF oxidation

EDX was used for high-throughput analysis of the oxygen uptake that occurred across the CSAFs during each exposure to dry air at 427 °C. Determining an appropriate set of real-space measurement points required the ability to predict compositions at locations that had not been previously analyzed. Therefore, the best-fit CDM for each CSAF was used to select 301 points that yielded a high-density coverage of composition space, and these were used for oxygen content measurements. EDX/ThinFilmID analysis at each point was used to determine its precise composition for subsequent plotting of all oxygen content data. SEM imaging of the Al-rich ($N_{\mathrm{Al}} > 0.85$) regions of the CSAFs revealed evidence of film dewetting upon annealing, so this region was not used for analysis of oxygen uptake.

A relative measure of oxygen content was obtained using the ratio of the O-to-Mo EDX signals at the selected locations on each CSAF after t_{ox} = 0, 1, 2, and 4 h total oxidation time in dry air at 427 °C. The oxygen content (C_{O}) and change in oxygen content (ΔC_{O}) after t_{ox} = 0, 1, and 4 h total oxidation time are shown in Figure 8 for the CSAF imaged in Figure 6(c). The data for 2 h are not shown because the oxygen uptake from 1 to 4 h was very slow. Since the specific value of the ratio of the O-to-Mo EDX

signals is simply proportional to the absolute oxygen content, C_{O} and ΔC_{O} are plotted using arbitrary units on a scale from 0 to the maximum C_{O} value measured on either CSAF. The three composition maps on the left present the total C_{O} in the CSAF after oxidation for $t_{ox} = 0$, 1, and 4 h. The two maps on the right represent ΔC_{O} in the intervals from 0 to 1 h and from 1 to 4 h. Cursory inspection of Figure 8 reveals oxygen uptake trends that appear to correlate with the visually identified regions 1-4 in composition space. The CSAF exposed to air for 15 min at 25 °C ($t_{ox} = 0$ h) exhibits only a small, measurable C_{O} with a maximum at $N_{\mathrm{Al}} \cong 0.60$. However, from $t_{ox} = 0$ to 1 h, there is a significant ΔC_{O} across all of composition space except region 1, and especially in the Fe-rich side of region 4. Further oxidation to $t_{ox} = 4$ h resulted in a negligible ΔC_{O} across regions 1, 2, and 3. The total C_{O} after $t_{ox} = 4$ h is clearly higher in regions 2 and 3 than in region 1; however, the maps of ΔC_{O} indicate that this oxygen uptake primarily occurred in the first hour of exposure and the CSAF appears to be effectively passivated for $t_{ox} > 1$ h.

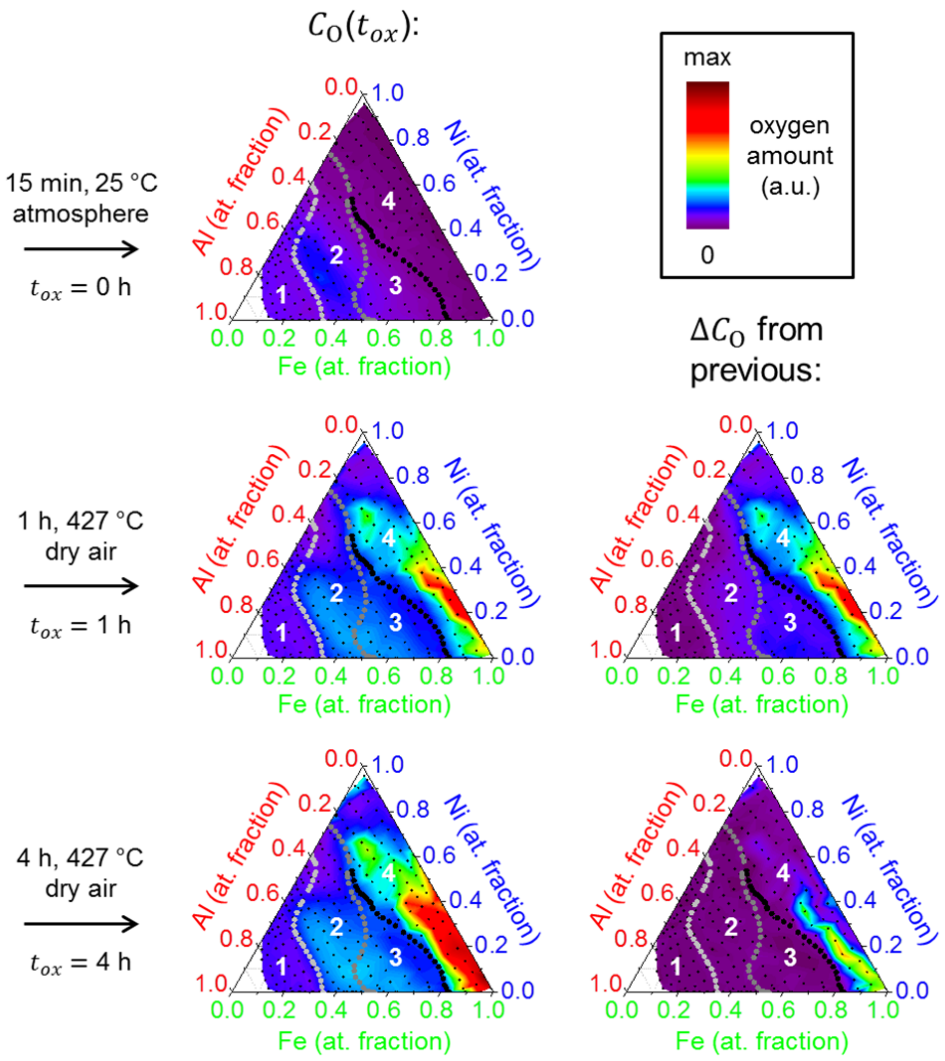

Figure 8. EDX-measured oxygen content (C_O, left) and the change in oxygen content from the previous exposure (ΔC_O, right) plotted in composition space for one of the $Al_xFe_yNi_{1-x-y}$ CSAFs after t_{ox} = 0, 1, and 4 h. The regions identified by visual analysis are overlaid for reference.

EDX allows reproducible measurement of C_O across composition space using a single CSAF. Three independent measurements of C_O were made for t_{ox} = 0, 1, 2, and 4 h at each of the 301 analysis points on the CSAF and used to calculate an average, $\bar{C}_O$. For the $C_O(t_{ox}$ = 4 h) data shown in Figure 8, the average measurement-to-measurement variability of C_O (normalized by $\bar{C}_O$) was found to have a standard deviation of σ = 7%. The values displayed at each point on the composition-space plots are $\bar{C}_O$. Because the reported values of C_O are normalized by the Mo EDX signal, they can be compared between the two CSAFs. Figure 9 shows the comparison of the final $C_O(t_{ox}$ = 4 h) measured in the CSAFs shown

in Figure 6(b, c). The oxygen content maps from the two CSAFs are very similar, indicating good reproducibility and validating the methodology.

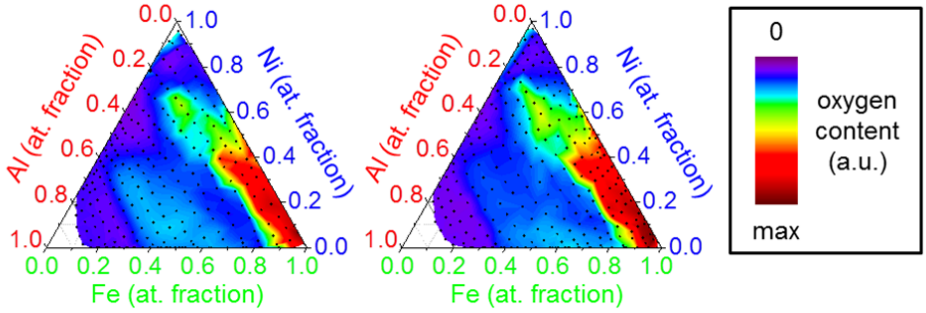

Figure 9. Comparison of EDX-measured oxygen content, C_O, across composition space for the two $Al_xFe_yNi_{1-x-y}$ CSAFs after oxidation in dry air for 4 h at 427 °C. The results appear to be very reproducible despite slight differences between the gradient geometry, thickness, and sampling compositions of the two CSAFs.

3.3.4. Raman and XPS characterization of $Al_xFe_yNi_{1-x-y}$ CSAF oxidation

Raman spectroscopy was used to identify oxide phases that formed in different regions of the CSAF imaged in Figure 6(c) after $t_{ox} = 4$ h. At each location, we observed one of only five characteristic Raman spectra, indicating the presence of NiO, $NiFe_2O_4$ spinel, α-Fe_2O_3, a mixture of $NiFe_2O_4$ spinel and α-Fe_2O_3, or no Raman-active oxides; representative spectra are shown in Figure 10(left). Figure 10(right) shows the distribution of oxide phases in ternary composition space for the 61 $Al_xFe_yNi_{1-x-y}$ compositions at which Raman spectra were obtained. Phases were identified by qualitative comparison of the measured Raman spectra with those for known Al, Fe, and Ni oxide phases.[44–54] FeO does not form below ~570 °C, so it was not considered.[43,55] Ranges of reported peak locations for possible phases are summarized in Table 1.[44–54] Raman spectra characteristic of Fe_3O_4, $FeAl_2O_4$, or $NiAl_2O_4$ were not observed on the CSAF. The known Raman spectra of NiO, $NiFe_2O_4$ spinel, and α-Fe_2O_3 were sufficient to allow assignment of all 61 spectra obtained from the oxidized $Al_xFe_yNi_{1-x-y}$ CSAF. It is important to note that the results in Figure 10 correspond only to the Raman-active oxide phases present in detectable quantities at a given location. This is not necessarily a complete listing of all the oxides phases that could have formed. For instance, while α-Al_2O_3 exhibits characteristic Raman scattering, amorphous Al_2O_3 and

γ-Al_2O_3 do not.[48,56] Given the oxidation temperature of 427 °C, it is expected that any pure Al oxide formed would be amorphous Al_2O_3 and/or γ-Al_2O_3.[5,11,22,57] Because Al oxidizes more readily than Fe and Ni, Al_2O_3 is likely to be present; however, as the transition to α-Al_2O_3 at temperatures <900 °C is negligibly slow, it is likely to remain in the amorphous Al_2O_3 or γ-Al_2O_3 forms and, therefore, be undetectable by Raman.[5,18,56] The results of the Raman analysis show that the four regions identified on the basis of visual inspection contain different oxide phases. Regions 1 and 2 do not contain detectable quantities of any Raman-active oxides, but have probably formed Al_2O_3. Region 3 contains α-Fe_2O_3 as the only Raman-detectable oxide phase. Region 4 contains NiO, $NiFe_2O_4$ spinel, and α-Fe_2O_3.

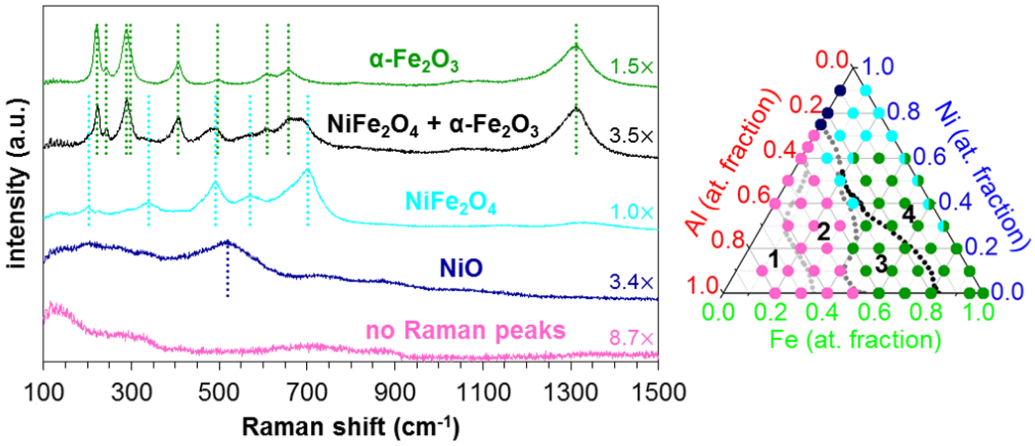

Figure 10. Left: Characteristic examples of the five types of Raman spectra observed at 61 locations across one of the $Al_xFe_yNi_{1-x-y}$ CSAFs after t_{ox} = 4 h in dry air at 427 °C. The spectra have been offset and magnified by the indicated factors for ease of viewing and are labeled with the oxide phases to which they are assigned. Characteristic peak locations are marked for NiO at 518 cm^{-1}; for $NiFe_2O_4$ at 202, 338, 491, 570, and 701 cm^{-1}; and for α-Fe_2O_3 at 221, 243, 289, 297, 407, 496, 610, 658, and 1313 cm^{-1}. **Right:** A ternary composition diagram showing the composition regions in which each type of spectrum was observed. The $NiFe_2O_4$ + α-Fe_2O_3 spectrum is indicated by the combination of $NiFe_2O_4$ and α-Fe_2O_3 markers. The boundaries identified by visual analysis are overlaid for reference.

Table 1. Ranges of major peak locations observed for Raman shifts (cm^{-1}).[44–54]

α-Fe_2O_3	Fe_3O_4	NiO [a]	$NiFe_2O_4$	$FeAl_2O_4$	$NiAl_2O_4$
220-227	298-306	510-518	200-207	~200	~320
236-247	533-550		325-340	~800	~370
282-293	662-696		483-491		~560
295-299			555-574		~600
396-412			695-704		~690
492-498					~720
596-613					~770
651-659					~810
1304-1322					~830

[a] The single NiO peak was reported by authors studying nanocrystalline samples.

XPS depth profiling was performed on the CSAF imaged in Figure 6(c) in order to determine both the composition and chemical state of the alloy as a function of depth into the CSAF. Fifteen locations were chosen near the boundaries identified by visual inspection. Comparison of cross-sectional composition and chemical state of the CSAF at points on opposite sides of a boundary reveals whether the boundary demarcates a transition in oxidation behavior. It is important to note that XPS depth profiles obtained from CSAFs that had been annealed in vacuum but only exposed to air during transfer to the XPS instrument (i.e. for conditions corresponding to $t_{ox} = 0$ h) confirm that the initial distribution of components across the film thickness was homogeneous. After $t_{ox} = 4$ h, the distribution becomes extremely inhomogeneous at many compositions. The image in Figure 11(upper left) shows the depth profile locations on the CSAF. Figure 11(a-g) shows the depth profiles at seven of these locations. The total Ar^+ sputter time is explicitly measured during the depth profiles and shown across the top of each plot. Approximate depths are shown at the bottom of each plot assuming an etch rate of 2 nm/min, which was estimated based on CSAF thicknesses determined from QCM measurements of deposition fluxes. The XPS spectra were used to estimate the composition of the oxidized CSAF versus depth at each point in terms of Al, Fe, and Ni in both their metallic and oxidized states and Mo. At no point was any Mo oxide detected. Given the relative sensitivities of the XPS peaks, the detection limits are estimated to be ~4, 1, 0.5, and 1 at.% for Al, Fe, Ni, and Mo, respectively. The depth profiles from various points on the CSAF indicate that there are four phenomenologically distinct types of alloy oxidation behavior whose $Al_xFe_yNi_{1-x-y}$ composition dependence is delineated by the three boundaries that were identified visually. Region 1 XPS depth profiles, Figure 11(a, b), appear to show a continuous layer of oxidized Al at the

CSAF surfaces with no detectable oxidized Fe or oxidized Ni at any depth. Depth profiles from region 2, Figure 11(c, d), reveal a thin surface layer containing oxidized Fe and/or Ni with a subsurface enrichment of oxidized Al, below which oxidized Fe and Ni are no longer detected. Region 3 depth profiles, Figure 11(e, f), are similar to those in region 2, but with less pronounced subsurface enrichment of oxidized Al, below which some oxidized Fe is observed. Finally, region 4 depth profiles, Figure 11(g), reveal extensive oxidation of all alloy components across the CSAF thickness.

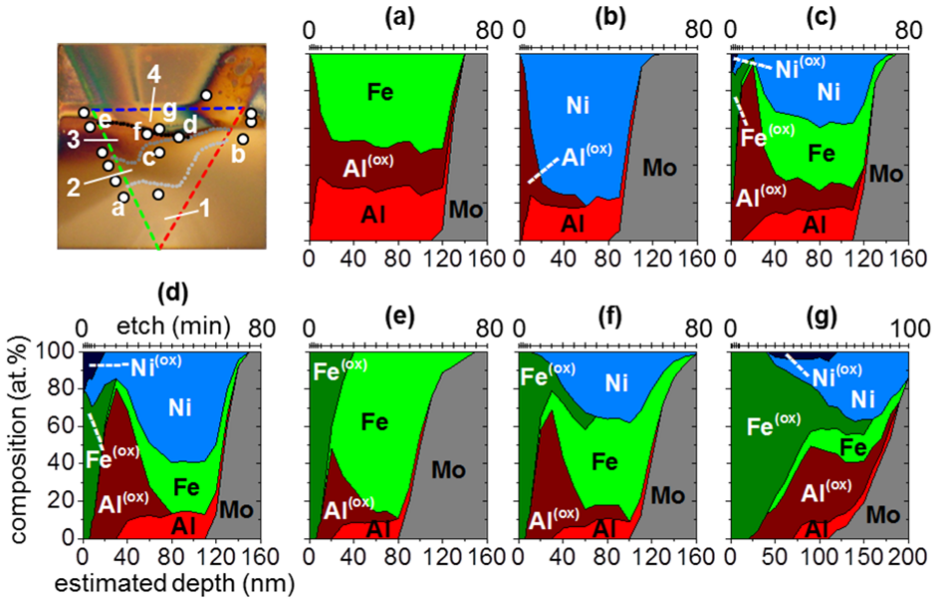

Figure 11. Upper left: The 15 locations (white circles) on an $Al_xFe_yNi_{1-x-y}$ CSAF (on a Mo substrate) at which XPS depth profiles were obtained after t_{ox} = 4 h in dry air at 427 °C. **(a)-(g)** The depth profiles obtained at the correspondingly labeled locations show the relative atomic concentrations of Al, Fe, Ni, and Mo in metallic or oxidized states as measured by XPS after Ar^+ etch times marked by the hashes above each plot. Similar oxidation profiles are observed within each of the visually identified regions 1-4. Increasing oxidation of Fe and/or Ni has occurred on moving from region 1 to region 4.

3.4. Discussion

The primary interest of this study was to determine the N_{Al}^{*} required for establishment of a continuous Al_2O_3 scale during the initial stages of oxidation in dry air at 427 °C. Based on Pettit's study of AlNi, we expect that $N_{Al}^{*} > N_{Al}^{**}$ in $Al_xFe_yNi_{1-x-y}$ at 427 °C, i.e. the Al concentration required for initial establishment of an Al_2O_3 scale is higher than the Al concentration required to maintain its steady-state

growth.[41] Thus, the compositions along the boundary between passivated and non-passivated regions of our $Al_xFe_yNi_{1-x-y}$ CSAFs define the trajectory of N_{Al}^{*} through the composition space. Identification of passivated regions in the $Al_xFe_yNi_{1-x-y}$ CSAFs was aided by the oxygen content data collected with EDX; alloy compositions with a passivating Al_2O_3 scale did not exhibit measurable oxygen uptake after the continuous Al_2O_3 layer was established. Based on the oxygen uptake data presented in Figure 8, it appears that passivation occurs within the first hour of oxidation in dry air at 427 °C (by $t_{ox} = 1$ h), after which large portions of the composition space experience no further measurable oxygen uptake through 4 h total exposure time (see ΔC_O from $t_{ox} = 1$ to 4 h, Figure 8(lower right)).

Oxidation behavior was assessed continuously across $Al_xFe_yNi_{1-x-y}$ composition space by correlating the visually identified regions 1-4 with the data obtained from EDX, Raman, and XPS depth profiling. Region 1 corresponds to passivation by exclusive formation of a continuous, surface Al_2O_3 scale, as shown schematically in Figure 12. The depth profiles obtained from this region (Figure 11(a, b)) show that the surface is covered by a continuous layer of oxidized Al that is ~2-4 nm in thickness with some additional oxidized Al in the subsurface; no other oxidized species are detected. As noted earlier, given the oxidation conditions used in this work, the Al oxide is likely to be amorphous Al_2O_3 and/or γ-Al_2O_3.[5,11,22,57] Oxygen uptake measurements (Figure 8) show $\Delta C_O \cong 0$ across region 1 from $t_{ox} = 0$ to 1 h in dry air at 427 °C, suggesting that the Al_2O_3 formation primarily occurred during the brief exposure to air at room temperature that occurred on removal from the RSM tool deposition chamber. Passivation of region 1 is indicated by the continued lack of detectable oxygen uptake during heating at 427 °C for up to 4 h (i.e. $\Delta C_O \cong 0$ from $t_{ox} = 1$ to 4 h). $C_O(t_{ox} = 4\text{ h})$ is the lowest of the four regions because oxygen is only present in the thin Al_2O_3 scale at the surface and any trace Al_2O_3 beneath it. As expected, the Raman spectra (Figure 10) do not show peaks in this region since neither amorphous Al_2O_3 nor γ-Al_2O_3 are Raman active and no other oxides are present.

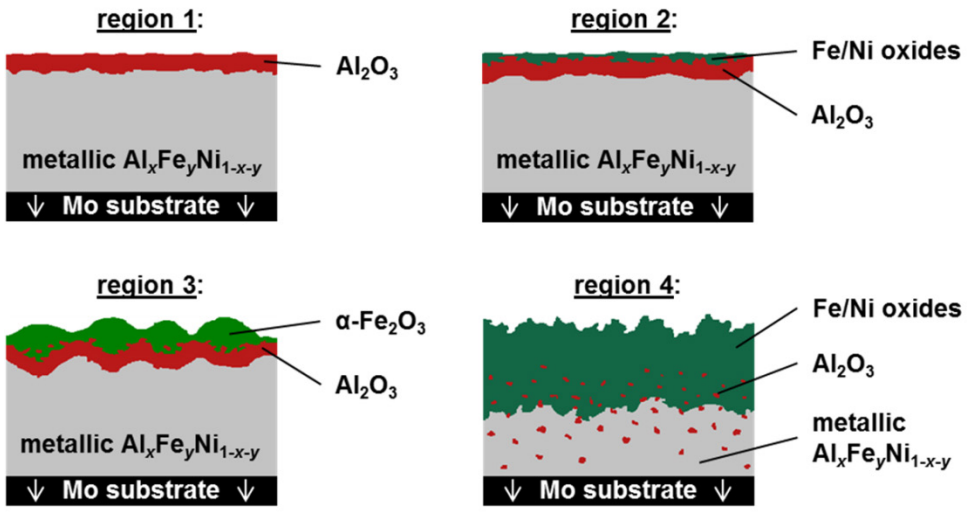

Figure 12. Schematic representations of the types of oxidation behavior proposed for regions 1-4 on the $Al_xFe_yNi_{1-x-y}$ CSAFs exposed to dry air for 4 h at 427 °C. The composition-space boundary of region 4 appears to define N_{Al}^*, the critical threshold for establishment of a passivating Al_2O_3 scale. The boundary between regions 1 and 2 demarcates a transition in the continuous Al_2O_3 scale from the surface to the subsurface.

Oxidation of the CSAF in region 2 appears to have resulted in the formation of a continuous, subsurface Al_2O_3 scale underneath a thin layer of Fe and/or Ni oxides (Figure 12). The depth profiles (Figure 11(c, d)) show formation of ~5-10 nm of Fe and/or Ni oxides under which there is extensive enrichment of oxidized Al. If the subsurface enrichment of oxidized Al corresponds to a continuous Al_2O_3 scale of comparable thickness (~3 nm) to the surface Al_2O_3 scale observed in region 1, it is quite likely that the depth profiles missed the point of continuous, 100% oxidized Al because of the coarse spacing (~10 nm) of the sampling at this depth. The lack of Fe or Ni oxides below the subsurface layer of oxidized Al suggests that it is, in fact, a continuous Al_2O_3 scale. This is further supported by the oxygen uptake data (Figure 8) which shows $\Delta C_O \cong 0$ from $t_{ox} = 1$ to 4 h, indicating passivation. The small, detectable ΔC_O from $t_{ox} = 0$ to 1 h and the slight visual discoloration that occurred during this exposure indicate that, unlike region 1, the passivation of region 2 was not completely developed during the room temperature exposure to air. $C_O(t_{ox} = 4\text{ h})$ is higher than that in region 1 due to the oxygen present in the Fe and/or Ni oxides at the surface. Raman spectra (Figure 10) do not show peaks across most of region 2 despite the presence of Fe and/or Ni oxides, most likely because the layers are too thin to be detected.

The oxidation behavior of region 3 is more difficult to interpret than those of regions 1 and 2. The $C_O(t_{ox} = 4\text{ h})$ in region 3 is similar to region 2 (Figure 8) and $\Delta C_O \cong 0$ from $t_{ox} = 1$ to 4 h, both suggesting that region 3 is passivated, yet the depth profiles (Figure 11(e, f)) seem to suggest that there is only partial subsurface enrichment of oxidized Al. Below this layer there appears to be some penetration of Fe oxide into the CSAF. One model that is consistent with the data is the growth of Fe oxide nodules during initial oxidation interrupting an otherwise laterally continuous Al_2O_3 scale (Figure 12), a well-known phenomenon in binary AlFe alloys.[7,11,43] The growth of nodules with Fe_2O_3 shells and Fe_3O_4 cores at an AlFe alloy surface can retard establishment of a continuous Al_2O_3 layer, but Al_2O_3 can ultimately form beneath the nodules, preventing their further growth and passivating the alloy bulk against further oxidation. Such behavior could lead to a continuous but "wrinkled" subsurface scale, consistent with the observed depth profiles; no plane parallel to the surface contains 100% oxidized Al, and the bottoms of nodules yield some Fe oxide signal below the depth of greatest oxidized Al enrichment, but not extending deep into the alloy. Raman analysis (Figure 10) revealed the presence of α-Fe_2O_3 across region 3, consistent with this description of the alloy oxidation behavior and its morphology. Fe_3O_4 was not observed with Raman and may not have formed during the early oxidation, though it could be present in undetectable quantities.

The CSAF oxidation behavior in region 4 is consistent with internal oxidation of the alloy (Figure 12). The depth profiles (Figure 11(g)) show extensive penetration of oxides deep into the CSAF. Raman (Figure 10) reveals the presence of NiO, $NiFe_2O_4$, and/or α-Fe_2O_3 depending on the atomic ratio of Ni and Fe. The highest values of $C_O(t_{ox} = 4\text{ h})$ are observed across much of region 4 (Figure 8) and, with the exception of compositions from ~70-95 at.% Ni, measureable oxygen uptake continues up to 4 h (i.e. $\Delta C_O > 0$ from $t_{ox} = 1$ to 4 h). Based on the depth profiles and Raman spectra, the compositions in region 4 with ~70-95 at.% Ni appear to be "pseudo-passivated" by a layer of $NiFe_2O_4$ (most likely due to its slow growth rate at 427 °C), but do not exhibit Al_2O_3-based passivation.

By combining all the results from the CSAF studies, early oxidation of $Al_xFe_yNi_{1-x-y}$ alloys in 427 °C dry air can be described in terms of four types of behavior (Figure 12) that subdivide composition space into regions. Regions 1, 2, and 3 are passivated by a surface Al_2O_3 scale, a subsurface Al_2O_3 scale, and a subsurface Al_2O_3 scale with interspersed Fe oxide nodules, respectively. The boundary of

region 4 defines the trajectory of N_{Al}^{*} across the ternary composition space. This boundary follows a complex path from $Al_{0.26}Ni_{0.74}$ to $Al_{0.17}Fe_{0.83}$, with a maximum N_{Al}^{*} at $Al_{0.29}Fe_{0.26}Ni_{0.45}$ and a minimum N_{Al}^{*} at $Al_{0.15}Fe_{0.74}Ni_{0.11}$. It is difficult to compare these results with work done by others, partly because of the relatively low temperature of our study, and partly because the full $Al_xFe_yNi_{1-x-y}$ composition space has never before been investigated comprehensively. A few relevant comparisons have been found, however.[11,22,41] Figure 13 summarizes our results and related data from the literature. The previously published boundaries were reported from studies using bulk alloy samples, dry oxygen, and oxidation temperatures at least 173 °C higher than the 427 °C used in our study. Based on a study of 19 single-composition $Al_xFe_yNi_{1-x-y}$ alloys, Sakiyama describes three regions of oxidation behavior at 600 °C for $N_{\mathrm{Fe}} > 0.40$ that are qualitatively similar to our observations for regions 2-4, but reports significantly different boundary locations in composition space.[22] This discrepancy might be explained by the difference in oxidation temperature between studies. Prescott reports in a review of AlFe oxidation that the minimum Al atomic fraction needed for "complete protection" against Fe oxide nodule formation is 0.10 at 1000 °C, but 0.21 at 600 °C, and Pettit found that N_{Al}^{*} in AlNi is 0.10 at 1100 °C, but 0.17 at 900 °C.[11,41] These findings indicate that Al content must be increased as oxidation temperature is decreased in order to maintain a given level of oxidation resistance in both binary AlFe and AlNi alloys, which is consistent with the differences between the boundary locations determined from our $Al_xFe_yNi_{1-x-y}$ CSAF results and those from the higher-temperature studies.

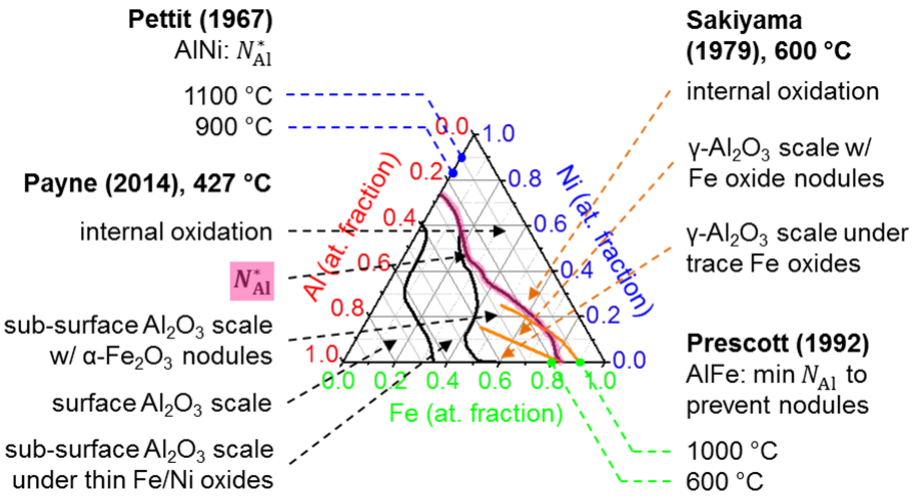

Figure 13. Summary of $Al_xFe_yNi_{1-x-y}$ oxidation behavior observed in this study after 4 h at 427 °C in dry air, and a comparison with similar results reported by other authors. Sakiyama describes behavior transitions at compositions >40 at.% Fe that are very phenomenologically similar to those observed in this study, but finds different locations for the boundaries demarcating these transitions. The results reported by Pettit and Prescott show Al content must be increased with decreasing temperature to maintain oxidation resistance, possibly explaining the differences in boundary locations between studies at different temperatures.

While our high-throughput techniques have allowed determination of a composition-space map of early oxidation behavior and the N^*_{Al} trajectory across composition space in $Al_xFe_yNi_{1-x-y}$ CSAFs, the degree to which these results are representative of bulk alloy oxidation is not clear from this work. This topic will be further explored in Chapter 5.

3.5. Conclusions

Using a combination of EDX, Raman spectroscopy, and XPS analyses of $Al_xFe_yNi_{1-x-y}$ CSAFs, early oxidation behavior in dry air at 427 °C was characterized across composition space for alumina-forming $Al_xFe_yNi_{1-x-y}$ alloys. Every possible $Al_xFe_yNi_{1-x-y}$ composition was found to undergo either internal oxidation or one of three distinguishable external oxidation events involving passivation by an Al_2O_3 scale. The value of N^*_{Al} was observed to decrease from 0.26 in binary AlNi to 0.17 in binary AlFe, taking a complex path through ternary composition space, and reaching a maximum at $Al_{0.29}Fe_{0.26}Ni_{0.45}$ and a minimum at $Al_{0.15}Fe_{0.74}Ni_{0.11}$. The boundaries separating the composition regions exhibiting the three different external oxidation mechanisms were similarly complex.

Compared to traditional alloy oxidation studies, the high-throughput methodologies developed in the course of this work increase by orders of magnitude the speed with which composition space can be sampled. This enables comprehensive studies of the dependence of the value of N_{Al}^{*} on composition in ternary alloys. Similar methods could be applied to CSAFs with compositions describing single planes through quaternary or higher-order alloy composition spaces. While the sub-micron thickness of the CSAFs created with the RSM tool has limited our investigations to early oxidation behavior, there is no reason why other methods could not be used to prepare much thicker CSAFs for high-throughput study of alloy oxidation at higher temperatures. More importantly, the continuous nature of the results obtained from CSAF oxidation studies can serve as a valuable tool for developing a fundamental understanding of key factors influencing the intricate dependence of oxidation kinetics on composition in ternary or higher-order alloys.

Chapter 4. $Al_xFe_yNi_{1-x-y}$ CSAF oxidation in 10% H_2O/air mixture at 427 °C

4.1. Introduction

A significant challenge in the design of alumina-forming alloys is that the value of N_{Al}^* can vary, not only as a function of multicomponent composition, but also based on the chemical nature of the oxidizing environment.[13,16] An example of particular practical importance is that that the presence of H_2O vapor is frequently found to be detrimental to the oxidation resistance of scale-forming alloys.[8,15,29,32,58,59] In both Fe- and Ni-containing alumina formers, it has been directly observed that N_{Al}^* is higher in the presence of H_2O vapor than in dry environments, but the physical origin of this phenomenon has yet to be definitively determined.[8,15,29,32,58] Developing an improved understanding of the effects of H_2O vapor in the oxidizing environment is critically important to the rational design of next-generation alumina formers.

In Chapter 3, we described a high-throughput methodology for assessing oxidation behavior across all possible compositions of $Al_xFe_yNi_{1-x-y}$ CSAFs using EDX, Raman spectroscopy, and XPS.[37] The results of our analyses allowed us to characterize phenomenologically the oxidation behavior occurring across all of $Al_xFe_yNi_{1-x-y}$ composition space in dry air at 427 °C, and to identify the continuous N_{Al}^* boundary defining the minimum Al content for which a passivating Al_2O_3 scale was established. The goals of the work reported in this Chapter were to apply the same high-throughput methodology to study the oxidation of $Al_xFe_yNi_{1-x-y}$ in a mixture of air and H_2O vapor at 427 °C, to identify any observable effects of H_2O vapor on the oxidation behavior or on the trajectory of N_{Al}^*, and finally, to consider the physical origins of any observed differences. As mentioned earlier, oxidation at 427 °C is very early/transient compared to that generally studied for alumina formers in much higher temperature environments. The primary intent of this Chapter is to demonstrate the potential value of high-throughput methods as a tool for screening environmental effects on alloy oxidation; to this end, $Al_xFe_yNi_{1-x-y}$ at 427 °C serves as a model system. Potential insights that such "early oxidation" of $Al_xFe_yNi_{1-x-y}$ CSAFs might offer into the oxidation of bulk alloys at higher temperatures will be discussed later.

4.2. Experimental methods

4.2.1. $Al_xFe_yNi_{1-x-y}$ CSAF preparation

Two $Al_xFe_yNi_{1-x-y}$ CSAFs were prepared using the RSM tool[4] (see Chapter 1.2) for the studies described in this Chapter. The preparation methodology was identical to that described in Chapter 3.2.1. The CSAFs were each deposited on the 14×14 mm^2 face of a 2.5 mm-thick polycrystalline-Mo substrate polished to a root mean squared roughness <1.5 nm. The substrate was sputtered under UHV conditions (~10^{-9} Torr base pressure) with a defocused 2 kV Ar^+ beam, annealed at 477 °C for 1 h, and then allowed to cool to room temperature. The Ar^+ sputtering was repeated immediately before deposition of the $Al_xFe_yNi_{1-x-y}$ CSAF. Al, Fe, or Ni pieces of ≥99.98% purity were used as source materials in the e-beam evaporators. The QCM was used to monitor deposition rates and determine the power setting required for each evaporator to achieve a target flux for its respective metal. The targeted deposition rates were chosen to yield an $Al_xFe_yNi_{1-x-y}$ CSAF thickness of ~100 nm while the three metals were co-deposited for 500 min. Immediately upon conclusion of a deposition, the CSAF was annealed to 427 °C for 2 h and then cooled to room temperature in UHV. We have previously performed XPS depth profiling which shows that this preparation results in a homogeneous distribution of Al, Fe, and Ni across the CSAF cross section, with no significant concentration of contaminants detected within the film. Each CSAF remained under UHV until the chamber was vented, at which point it was exposed to ambient air for a period of ~15 min while it was transferred to a *Tescan* Vega3 SEM operated at ~10^{-4} Torr.

4.2.2. EDX mapping of $Al_xFe_yNi_{1-x-y}$ CSAF composition gradients

After deposition, EDX spectra obtained in the SEM were used to map $Al_xFe_yNi_{1-x-y}$ composition as a function of position on each CSAF. The experimental procedure for doing so was developed as part of the work described in Chapter 3. EDX measurements of $Al_xFe_yNi_{1-x-y}$ composition were taken at discrete locations across the 12×12 mm^2 region in the center of the 14×14 mm^2 CSAF surface. The measurements were spaced by 1 mm on a 13×13 square grid. The EDX spectra (0-10 keV, 10 eV binning, >300,000 total counts per spectrum) were collected from 50×50 μm^2 area scans with the SEM beam operating at 11.24 kV. The $Al_xFe_yNi_{1-x-y}$ composition of the CSAF was determined from each spectrum by quantification using the *Oxford Instruments* software package INCA ThinFilmID, which was

used to account for the compositional inhomogeneity with depth in the beam interaction volume. The assumption used for processing the spectra was that the $Al_xFe_yNi_{1-x-y}$ was present as a flat, homogenous layer on the Mo substrate, which we have previously confirmed to be reasonably accurate via XPS depth profiling. The EDX measurements of CSAF composition were repeated three times at each grid location, and the results were averaged to reduce noise. The results of this composition mapping were also used to determine parameter values defining a best-fit CDM for each $Al_xFe_yNi_{1-x-y}$ CSAF (see Chapter 2), where A_{Al}, A_{Fe}, and A_{Ni} were each modeled using a linear wedge (Figure 4, Equation 2.1).

4.2.3. Oxidation and visual analysis of $Al_xFe_yNi_{1-x-y}$ CSAFs

The $Al_xFe_yNi_{1-x-y}$ CSAFs were oxidized at an elevated temperature in a ceramic boat in the center of a quartz tube furnace (~60 cm long, 2 cm diameter) with one end open to atmosphere and the other end connected to a gas-introduction manifold. A regulator was used to maintain a continuous flow of ~1 slpm from a cylinder of lab-grade dry air, which was bubbled through a series of two ~1 L heated H_2O baths before being introduced into the furnace tube via the manifold. The H_2O temperature in the first bath in the series was maintained at 61±1 °C, while the second was maintained at 46±1 °C. The gas-flow lines between the first and second baths and between the second bath and the entrance to the furnace were heated and maintained at >61 °C. The air was introduced near the bottom of each bath through a microporous, stainless-steel fitting which broke the air stream into small bubbles. As a result of humidification in the baths, we estimate that the gas entering the furnace contained an H_2O partial pressure of ~75 Torr, the equilibrium vapor pressure at 46 °C. Thus, the gas feed to the furnace was ~10% H_2O in air by volume. Henceforth in this text, this gas feed will simply be referred to as “humid air”. Prior to oxidation of an $Al_xFe_yNi_{1-x-y}$ CSAF, the furnace and ceramic boat were preheated until the temperature was stable at 427±1 °C while the humid air was flowing. The boat was then pulled to the open end of the furnace, the CSAF was quickly loaded such that only the underside of the Mo substrate was in direct contact with the ceramic, and the boat/CSAF were pushed back to the center of the furnace. In three cycles, after total exposure times to the furnace environment, t_{ox}, of 1, 2, and 4 h, the CSAF was removed from the furnace and the bottom of the Mo substrate was placed in contact with aluminum foil to

quickly dissipate heat, cooling the sample to near room temperature in ~2 min. On each such occasion, the CSAF was photographed and then loaded into the SEM for further characterization.

Oxidation of $Al_xFe_yNi_{1-x-y}$ CSAFs at 427 °C causes visually observable changes in their surface coloration which can vary markedly with composition, i.e. with real-space location on the surface. Sharp transitions in surface coloration can sometimes be shown to correlate to a measurable transition in the oxidation behavior that has occurred in two neighboring regions of $Al_xFe_yNi_{1-x-y}$ composition space, as shown by our previous studies of $Al_xFe_yNi_{1-x-y}$ CSAF oxidation in dry air at 427 °C (Chapter 3). Photographs of the CSAFs after each oxidation stage allow such visually distinguishable regions to be accurately defined in real space, which is useful in determining locations on the CSAF on which to focus more time-intensive spectroscopic techniques used to characterize oxidation behavior. Any such data collected in real space can also be rapidly translated into $Al_xFe_yNi_{1-x-y}$ composition space by applying the best-fit CDM for the CSAF.

4.2.4. EDX, Raman, and XPS characterization of $Al_xFe_yNi_{1-x-y}$ CSAF oxidation

In Chapter 3, we describe the development of a methodology for the high-throughput characterization of oxidation behavior across CSAFs using a combination of EDX, Raman spectroscopy, and XPS depth profiling.[37] The same techniques were applied in studies described in this Chapter, but were used to characterize the oxidation of $Al_xFe_yNi_{1-x-y}$ CSAFs exposed to humid air instead of dry air at 427 °C. With a few minor exceptions (which will be explicitly stated), the experimental procedures for the various spectroscopic measurements made in this work were identical to those described in Chapter 3.

EDX was used to monitor oxygen uptake at a large number of locations (261 on one sample and 335 on the other) across the CSAFs as a function of t_{ox} (total exposure time to humid air at 427 °C in the furnace). The real-space coordinates of these locations were chosen (with guidance from the CDM fit to each CSAF) such that a high-density sampling of $Al_xFe_yNi_{1-x-y}$ composition space was obtained from each sample. The precise $Al_xFe_yNi_{1-x-y}$ film composition at each location was first measured by EDX procedures identical to those used in the initial mapping of the composition gradients on the samples. Measurements of the total oxygen content at each location (i.e. the total amount of oxygen present in the entire CSAF cross section), $C_O(x, y)$, were then obtained from additional EDX scans after each $t_{ox} = 0$, 1,

2, and 4 h. These scans were used to collect spectra (0-10 keV, 10 eV binning, >250,000 total counts per spectrum) across 50×50 μm^2 areas with the SEM beam operating at 30 kV, for which the C_O of the CSAF is approximately proportional to the oxygen EDX signal scaled by the (much larger) Mo signal from the substrate. For this proportionality approximation to be accurate, the depth sensitivity of EDX must significantly exceed the thickness of the CSAF, which was demonstrated to be the case for EDX measurements made with the SEM beam operating at 20 kV, as described in Chapter 3.2.4. For the work described in this Chapter, EDX measurements of C_O were made using a beam voltage of 30 kV (the maximum possible for our instrument) instead of 20 kV. This was done to further increase the EDX depth sensitivity and, therefore, the accuracy of the proportionality approximation; however, from a practical standpoint, we have not observed any significant difference between using 30 kV and 20 kV spectra to determine C_O when the results are compared on a normalized scale. The EDX measurements of C_O were repeated three times at each location for each sampled t_{ox}, and the results were averaged to reduce noise.

Raman spectroscopy was used to analyze one of the $Al_xFe_yNi_{1-x-y}$ CSAFs after $t_{ox} = 4$ h. A green laser (532 nm wavelength, 200 mW, 100 μm aperture with 50× focusing lens resulting in ~30 μm spot size) was used for excitation, and the Raman-shift spectrum in the range 100-1500 cm^{-1} was measured at 69 locations across the surface using a CCD detector calibrated with Si. The collected spectra were de-spiked using NGSLabSpec software. To focus on transitions between visually distinct regions, the locations for obtaining Raman spectra were chosen in real space based on the appearance of the oxidized surface. Spectra characteristic of an α-Fe_2O_3 and/or $NiFe_2O_4$ phase were observed in some regions, while the spectra in other regions did not reveal any significant Raman scattering.

XPS depth profiling was used to characterize 12 spatially resolved locations on one of the oxidized $Al_xFe_yNi_{1-x-y}$ CSAFs after $t_{ox} = 4$ h. A set of XPS measurements (Al K_α X-rays, ~200 μm measurement spot size, hemispherical energy analyzer) followed by uniform etching of the analysis area with a rastered Ar^+ beam (3 kV, 1 μA) was performed in 65 identical cycles at each of the locations. For each set of XPS measurements, four different spectra were acquired across 10-14 eV binding-energy ranges containing the non-overlapping Al 2s, Fe $2p_{1/2}$, Ni $2p_{3/2}$, and Mo $3p_{3/2}$ peaks. The spectra were measured using a 0.05 eV step size and 0.2 s dwell time, with a detector pass energy of 100 eV. The

spectral data were quantified by peak fitting with *Thermo* Avantage (v4.88) processing software using the *Thermo* "Smart" background subtraction. The results were used to construct a cross-sectional profile of elemental composition at each location with additional designation of the fraction of each species in an oxidized (as opposed to metallic) chemical state. The XPS peak-fitting procedure was slightly more sophisticated than that used for the XPS depth profiles in Chapter 3. Geometric parameters defining a unique shape for the metallic Al, Fe, Ni, and Mo peaks were determined from measurements made on pure standards that were Ar^+ sputtered with the same settings used for the depth profiling. Under these conditions, the peaks for metallic Al, Fe, and Ni were found to exhibit slight tailing at high binding energies which is captured by the peak-fitting parameters. Oxidation of the metal species in the CSAFs was found to increase the binding energy of the monitored peaks by ~2-5 eV. Geometric fitting parameters were determined for oxidized Al, Fe, Ni, and Mo peaks such that, after fitting, the sum of the metallic and oxidized peaks reasonably reflected the measured spectra for all cycles and locations. This was accomplished by defining a single oxidized peak for Al, Fe, and Mo, but two oxidized peaks were required for Ni. Assignment of the oxidized peaks to specific oxidation states was not attempted. The specific peak-fitting constraints used in the *Thermo* Avantage software are presented in Table 2. Figure 14 shows examples of resulting peak fits obtained using these constraints for spectra collected during the depth profiles. Examples of spectra containing metallic-only peaks (first row), metallic and oxidized peaks (second row), and oxidized-only peaks (third row) are provided for each Al 2s (first column), Fe $2p_{1/2}$ (second column), and Ni $2p_{3/2}$ (third column). The overall elemental composition at each location/cycle was calculated by normalizing the total peak area for each species by Wagner sensitivity factors. The oxidized-to-metallic ratio for each element was estimated to be equal to the ratio of the area of the oxidized peak(s) to the area of the metallic peak.

Table 2. Fitting constraints for XPS peaks used in *Thermo* Avantage software.

peak	peak binding energy (eV)	FWHM (eV)	L/G mix product (%)	tail mix (%)	tail height (%)	tail exponent
Al	117.35-117.45	1.36	30	50.50	0	0.0341
$Al^{(ox)}$	119.0-121.0	2.4-2.6	30	100	0	0
Fe	719.7-720.2	2.00	30	30.00	0	0.0420
$Fe^{(ox)}$	723.0-725.0	0.5-3.5	30	100	0	0
Ni	852.4-853.4	1.22	84	51.27	0	0.1411
$Ni^{(ox)}$ (#1)	854.4-855.6	2.80	30	100	0	0
$Ni^{(ox)}$ (#2)	856.6-857.0	0.5-3.5	30	100	0	0
Mo	393.7-394.0	0.5-3.5	88	100	0	0
$Mo^{(ox)}$	397.0-398.5	0.5-3.5	30	100	0	0

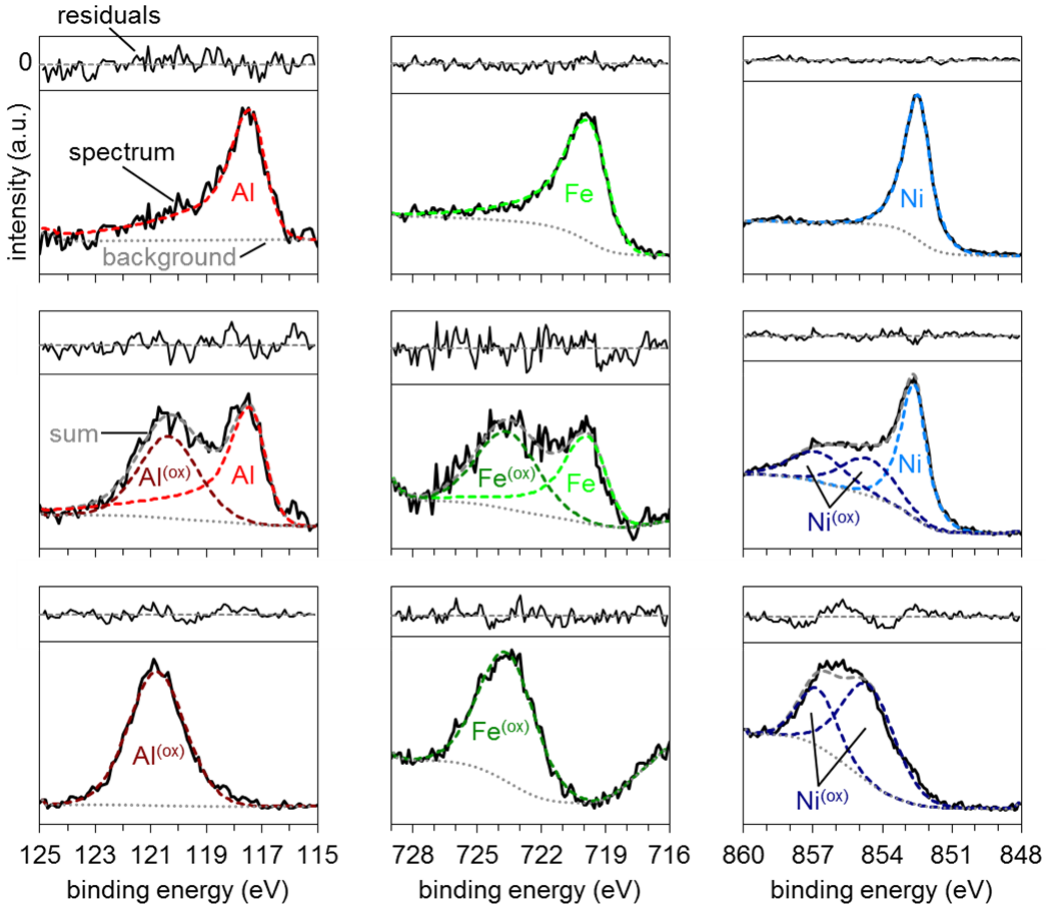

Figure 14. The bottom sections of the plots show examples of the metallic/oxidized peak fitting for various Al 2s, Fe $2p_{1/2}$, and Ni $2p_{3/2}$ XPS spectra obtained during depth profiles of an $Al_xFe_yNi_{1-x-y}$ CSAF. Fitting of a *Thermo* "Smart" (modified Shirley) background was performed in each case and is included on the plots. The top section of each plot shows the residuals of the overall fit with the value of zero indicated by the horizontal dashed line.

4.3. Results

4.3.1. Spatial maps of $Al_xFe_yNi_{1-x-y}$ CSAF composition gradients

$Al_xFe_yNi_{1-x-y}$ composition was measured using EDX at discrete points on a 13×13 grid covering the 12×12 mm^2 region in the center of each of the two CSAFs. Figure 15 shows real-space contour plots of the relative composition of Al, Fe, and Ni in one of the two CSAFs. The 169 discrete $Al_xFe_yNi_{1-x-y}$ compositions that were measured are plotted as points in the ternary composition diagram of Figure 15. Because the composition gradients in the CSAF are continuous, all possible compositions within the range of the discretely plotted points on this diagram are also present within the 12×12 mm^2 region. A similar composition map was measured for the other CSAF used in this study. Both CSAFs spanned the full $Al_xFe_yNi_{1-x-y}$ composition space within the 14×14 mm^2 bounds of the surface. The measurement precision of the compositions plotted in Figure 15 is about ±0.5 at.%. Additional discussion regarding the accuracy of EDX as a technique for measuring CSAF composition may be found in Chapter 3.3.1.

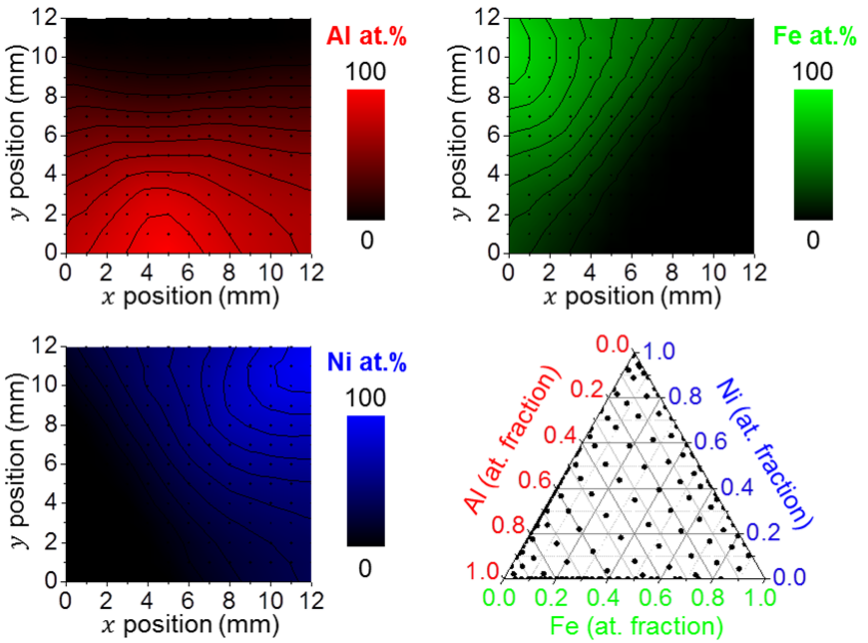

Figure 15. Real-space contour plots of the relative Al, Fe, and Ni concentrations in one of the CSAFs as determined by EDX measurements taken at the marked locations on a square grid. The set of discrete $Al_xFe_yNi_{1-x-y}$ compositions measured from the grid locations are plotted as points in the ternary composition diagram. Nearly complete coverage of $Al_xFe_yNi_{1-x-y}$ composition space is observed within the plotted region of the CSAF surface.

4.3.2. Visual identification of $Al_xFe_yNi_{1-x-y}$ CSAF oxidation behavior boundaries

Distinct changes in the surface coloration of $Al_xFe_yNi_{1-x-y}$ CSAFs occur during oxidation. The images in Figure 16(a, b) show one of the CSAFs after $t_{ox} = 0$ and $t_{ox} = 4$ h in humid air at 427 °C. The approximate location of the pure-component corners and triangular ternary-composition area (determined using the CDM fit to the CSAF) are overlaid on the images for reference. The most significant changes in surface coloration tend to occur on portions of the CSAF with low Al content, while little change is observable across much of the region of the CSAF with high Al content. The visual appearance of the CSAF at $t_{ox} = 4$ h, shown in Figure 16(b), was largely established by $t_{ox} = 1$ h. The only notable change from $t_{ox} = 1$ to 2 h and 2 to 4 h was a gradual darkening of the brown area surrounding the pure-Ni corner of the ternary-composition area.

A number of boundaries between distinctly colored regions can be readily observed on the oxidized $Al_xFe_yNi_{1-x-y}$ CSAF in Figure 16(b). Simple visual inspection of the sample can be used to determine the real-space trajectory of any such boundaries, which can then be translated into $Al_xFe_yNi_{1-x-y}$ composition space using the CDM. Three boundaries are identified and marked on the CSAF in Figure 16(b). These boundaries subdivide the triangular ternary-composition area into four increasingly discolored regions, labeled 1-4. Figure 16(c) shows an image of the other $Al_xFe_yNi_{1-x-y}$ CSAF used in this study after $t_{ox} = 4$ h. The discoloration patterns that were developed on the surfaces of the two CSAFs are quite similar. Equivalent boundaries to those marked on the CSAF in Figure 16(b) were identified and are shown on the second CSAF in Figure 16(c). On each CSAF, the boundaries separating regions 2, 3, and 4 were identified purely on the basis of visual analysis, but the boundary between regions 1 and 2 was identified with partial guidance from SEM imaging. Figure 16(d) shows a low-magnification SEM image (secondary-electron detection) of a large portion of the surface of the CSAF shown in Figure 16(c). The boundary between region 1 (which is not discolored as a result of oxidation) and region 2 (which is lightly discolored as a result of oxidation), while fairly obvious near the AlFe binary compositions of the CSAF, becomes difficult to distinguish visually near the AlNi binary compositions of the CSAF. However, the transition from region 1 to 2 exhibits clear contrast in the SEM image across the entire CSAF. SEM imaging was used to ensure that the boundary between regions 1 and 2 was identified correctly near the AlNi binary compositions of the CSAFs.

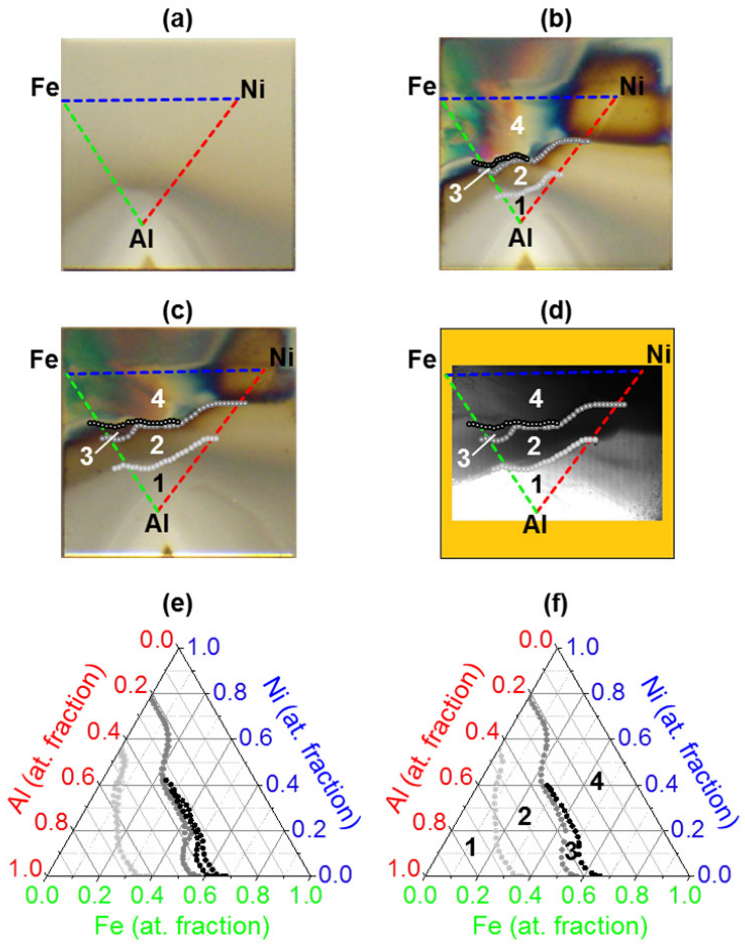

Figure 16. **(a)** Photograph of one of the $Al_xFe_yNi_{1-x-y}$ CSAFs after deposition, UHV annealing (427 °C for 2 h), and brief (~15 min) exposure to ambient atmosphere. The location of the ternary-composition area as estimated by the CDM is shown for reference. **(b)** Photograph of the same CSAF after oxidation in humid air (10 mol% H_2O) for 4 h at 427 °C. The overlaid boundaries subdivide the surface into visually differentiable real-space regions 1-4. **(c)** Photograph of the second $Al_xFe_yNi_{1-x-y}$ CSAF used in the study after oxidation in humid air for 4 h at 427 °C. Boundaries are marked around regions that are qualitatively equivalent to those identified in (b). **(d)** Low-magnification SEM image of a large portion of the surface of the CSAF shown in (c). The transition from region 1 to region 2 appears clearly as an abrupt shift in contrast from light to dark. **(e)** Composition-space comparison of the boundaries identified in (b) and (c) after conversion by the respective best-fit CDM for each CSAF. **(f)** Average of the two sets of boundaries shown in (e).

Figure 16(e) shows a superimposition of the results of the visual analyses from Figure 16(b, c) upon conversion of the real-space boundaries to composition space using the respective CDM for each CSAF. As discussed in Chapter 3.3.2, the CDM accurately predicts CSAF composition (as would be measured with EDX) at interpolated real-space locations to about ±2 at.% for each alloy component. Thus, Figure 16(e) demonstrates that the results of the visual analyses from the two samples were

reproduced to within the expected precision of the technique. Figure 16(f) shows an average of the two sets of boundaries in Figure 16(e). These will be used as the basis for subsequent discussion of the spectroscopic analyses used to characterize the oxidation behavior of the $Al_xFe_yNi_{1-x-y}$ CSAFs in different regions of composition space.

4.3.3. EDX measurement of oxygen uptake during $Al_xFe_yNi_{1-x-y}$ CSAF oxidation

EDX was used to make high-throughput measurements of the total, relative oxygen content at discrete $Al_xFe_yNi_{1-x-y}$ compositions across each CSAF after t_{ox} = 0, 1, 2, and 4 h total oxidation time in humid air at 427 °C. This was done at a large number of points to provide a dense sampling of ternary space; however, the Al-rich ($N_{\mathrm{Al}} > 0.85$) regions of the CSAF were excluded because SEM imaging revealed that these portions of the film were dewetted from the substrate during the initial UHV annealing. Figure 17 shows the oxygen content (C_{O}) and change in oxygen content (ΔC_{O}) after t_{ox} = 0, 1, and 4 h as measured across the CSAF shown in Figure 16(c). The data from t_{ox} = 2 h was not included because oxygen uptake from 1 to 4 h was very slow. C_{O} was calculated as the ratio of the O-to-Mo EDX signals and is plotted on an arbitrary, linear scale from 0 to the maximum value measured on either CSAF. The three composition maps on the left display the total C_{O} measured across the CSAF after t_{ox} = 0, 1, and 4 h. The two maps in the center show ΔC_{O} during the intervals from 0 to 1 h and from 1 to 4 h. The map on the right shows the ΔC_{O} data from t_{ox} = 1 to 4 h with the scale amplified by a factor of 4.5× to accentuate the important features. The visually determined boundaries from Figure 16(f) are plotted on each of the maps. The data in Figure 17 reveal several important correlations between trends in oxygen uptake and the visually distinct regions 1-4. Small values of C_{O} were measured across $Al_xFe_yNi_{1-x-y}$ composition space at t_{ox} = 0 h (after exposure of the sample to ambient air at room temperature for ~15 min), which reach a maximum at $N_{\mathrm{Al}} \cong 0.60$. From t_{ox} = 0 to 1 h, the ΔC_{O} plot shows that measurable oxygen uptake occurred across all of composition space except in region 1, but the uptake in region 4 was much larger than in either region 2 or 3. Oxygen uptake from t_{ox} = 1 to 4 h is only detectable in region 4. The total C_{O} after t_{ox} = 4 h is slightly higher in regions 2 and 3 than in region 1, but clearly is significantly higher in region 4 than in any of the other three regions.

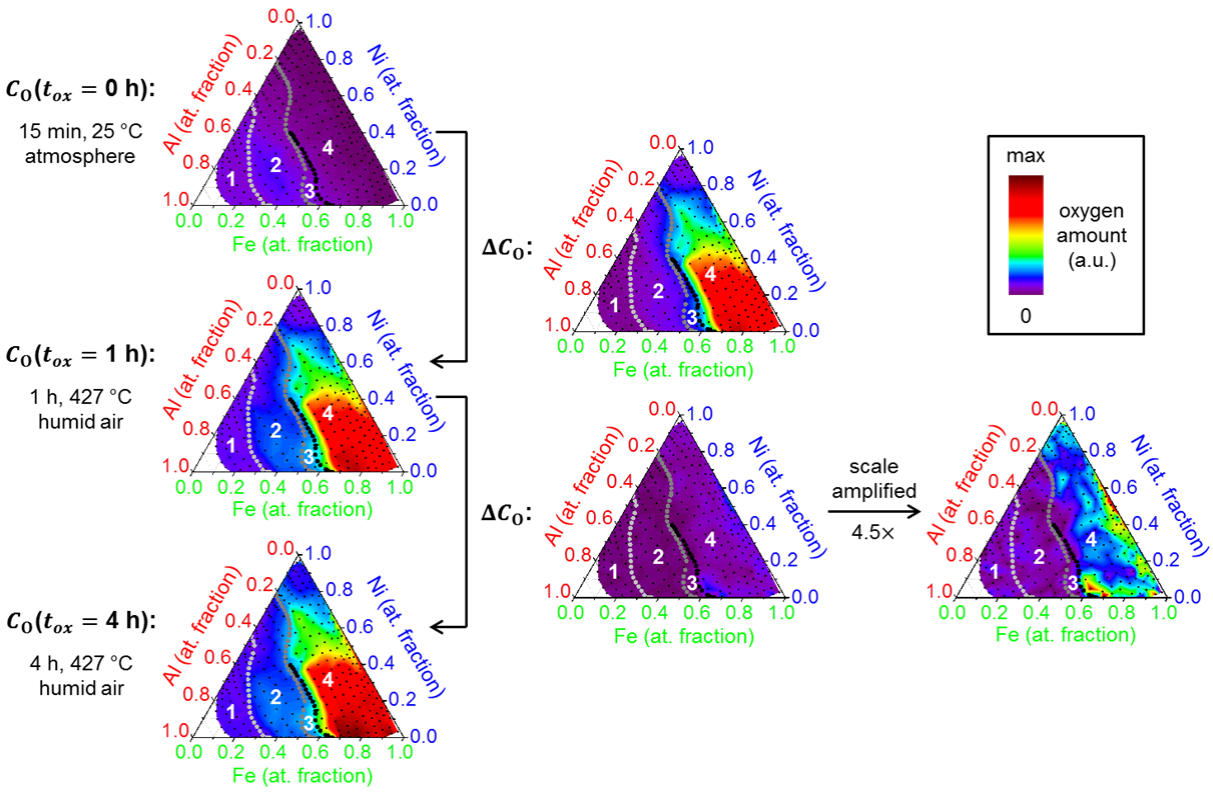

Figure 17. EDX-measured oxygen content (C_O, left) and the change in oxygen content (ΔC_O, middle) plotted in composition space for one of the $Al_xFe_yNi_{1-x-y}$ CSAFs based on data collected after t_{ox} = 0, 1, and 4 h exposure to humid air (10 mol% H_2O) at 427 °C. The right-most composition map shows the ΔC_O data between 1 and 4 h replotted using an amplified (4.5×) scale. The regions identified by visual analysis are overlaid on each of the composition maps for reference. No significant uptake of additional oxygen is detectable in composition regions 1, 2, or 3 for $t_{ox} > 1$ h.

Additional information regarding the measurement-to-measurement variability when using EDX to determine C_O may be found in Chapter 3.3.3. The measurement precision for the C_O values plotted in Figure 17 is about ±4%. We have also found oxygen uptake data collected from CSAFs using EDX to be very reproducible between samples. Figure 18 shows a comparison of the $C_O(t_{ox} = 4$ h) from Figure 17 with that measured from the other CSAF shown in Figure 16(b). A unique set of $Al_xFe_yNi_{1-x-y}$ compositions was sampled on each CSAF but, due to the high-density coverage of ternary space, it is clear that the maps are very similar.

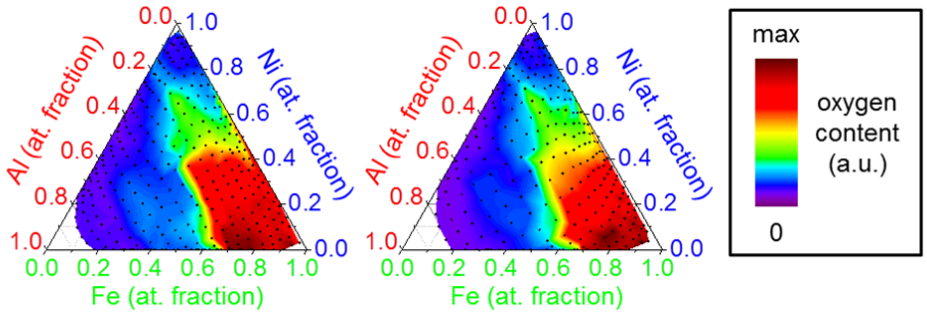

Figure 18. Composition-space comparison of EDX-measured oxygen content (C_O) in the two $Al_xFe_yNi_{1-x-y}$ CSAFs used in the study after exposure to humid air for 4 h at 427 °C. Although a different set of compositions was sampled in each case, the results are well reproduced between CSAFs.

4.3.4. Raman characterization of oxide phases formed in an $Al_xFe_yNi_{1-x-y}$ CSAF

Raman spectra were acquired at 69 locations across the CSAF imaged in Figure 16(c) (t_{ox} = 4 h in humid air at 427 °C). The locations were chosen to emphasize the transitions between the visually distinct regions 1-4. At each location, one of four characteristic Raman spectra was observed, consistent with either 1) $NiFe_2O_4$ spinel, 2) α-Fe_2O_3, 3) both $NiFe_2O_4$ spinel and α-Fe_2O_3, or else 4) showing no observable Raman scattering activity; representative examples of each of these four types of spectra are shown in Figure 19(left). Figure 19(right) shows the points in $Al_xFe_yNi_{1-x-y}$ composition space at which the different types of spectra were obtained. Phase assignments were made by qualitative comparison to known Raman peak locations for various Al, Fe, and Ni oxide phases. The phases considered were the same as discussed for the dry-air oxidation study in Chapter 3.3.4 (the phases and their expected Raman peak locations are listed in Table 1). The expected peak positions for $NiFe_2O_4$ and/or α-Fe_2O_3 were sufficient to assign all observable peaks in 63 of the 69 spectra. The remaining 6 spectra, which are marked with an asterisk in Figure 19, contained (either additionally or exclusively) low-intensity peaks that could not be assigned to either $NiFe_2O_4$ or α-Fe_2O_3. The 5 marked points along the FeNi binary axis contained a weak set of peaks with a primary feature at ~202 cm^{-1} that may be attributable to a MoO_2 phase,[60] while the single marked point near the pure-Fe corner contained a weak doublet peak at ~929/937 cm^{-1} which may be indicative of β-$FeMoO_4$.[61] Such species might have been formed by oxidation of the Mo substrate, but as these points were all located far from the transitions between the numbered regions (and at very low or zero Al content), the details of their origin were not considered

further. Figure 19 shows that there are evident correlations between the visually distinct regions 1-4 and the results of the Raman analysis. No significant Raman scattering was observed across the majority of regions 1 and 2. Spectra characteristic of α-Fe_2O_3 were observed exclusively across region 3. In region 4, a transition from spectra characteristic of α-Fe_2O_3, to spectra characteristic of $NiFe_2O_4$, to spectra exhibiting minimal Raman scattering is observed as the Ni-to-Fe ratio increases. It is important to keep in mind that while Raman spectroscopy can allow identification of specific oxide phases at different locations across the CSAF, it does not exclude the possibility of oxides which are not detectable using Raman or are present in small, undetectable quantities. Based on the results of the dry-air oxidation study described in Chapter 3, it is expected that Raman-inactive (γ- or amorphous) Al_2O_3 was formed at all compositions for which no Raman peaks were observed. In addition, it is possible that trace amounts of Fe or Ni oxides may have formed at some of these compositions as well.

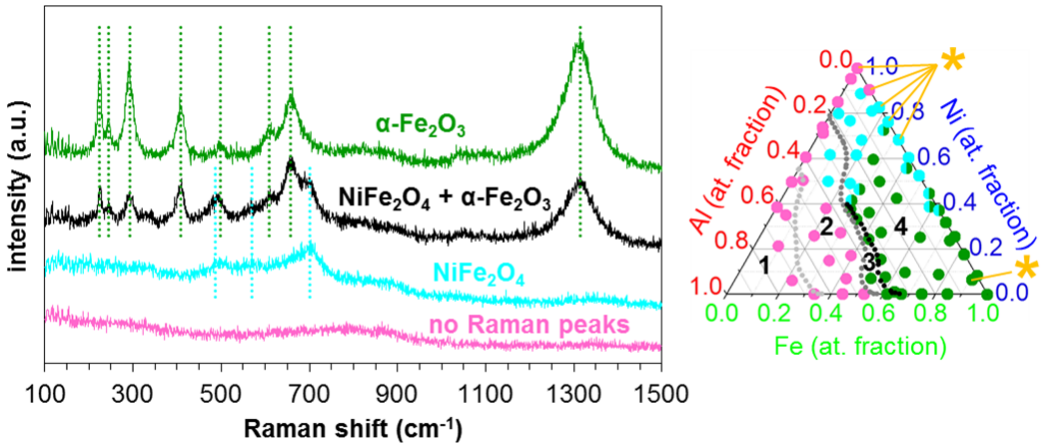

Figure 19. Left: Representative examples of the four primary types of Raman spectra observed at 69 locations across one of the $Al_xFe_yNi_{1-x-y}$ CSAFs after t_{ox} = 4 h in humid air at 427 °C. The spectra are offset and labeled with the oxide phases to which they are assigned. Characteristic peak locations are marked for $NiFe_2O_4$ at 486, 570, and 701 cm^{-1}; and for α-Fe_2O_3 at 224, 245, 292, 409, 498, 609, 657, and 1315 cm^{-1}. **Right:** A ternary diagram showing the compositions of the $Al_xFe_yNi_{1-x-y}$ CSAF where the different types of spectra were observed. The boundaries identified by visual analysis are overlaid for reference. The $NiFe_2O_4$ + α-Fe_2O_3 spectrum is indicated by a combination of $NiFe_2O_4$ and α-Fe_2O_3 markers. The 6 spectra obtained at the compositions marked with an asterisk also contained weak, unassigned peaks, possibly attributable to trace Mo oxide phases having formed by interaction with the substrate.

4.3.5. XPS depth profiling of oxidized $Al_xFe_yNi_{1-x-y}$ CSAF

XPS depth profiling was used to measure cross-sectional profiles of elemental composition and chemical state at 12 locations across the CSAF imaged in Figure 16(c). The locations were chosen to sample both binary and ternary compositions on the CSAF in each of the visually distinct regions 1-4. Figure 20 shows the 12 real-space locations that were analyzed and the resulting depth profiles obtained at 9 of these locations. The locations are shown on both a photograph of the CSAF (upper left) and a low-magnification SEM image of a portion of the surface (upper right); in both cases, the location of the triangular ternary-composition area and the boundaries separating regions 1-4 are shown for reference. The horizontal axes of the profiles show the total Ar^+ etch time prior to each set of XPS measurements, which were used to determine the relative atomic concentrations shown on the vertical axes. While increasing Ar^+ etch time (which is explicitly measured) correlates with increasing sampling depth into the CSAF, it should be noted that this relationship is not expected to be directly proportional for an inhomogeneous cross section due to potentially different etch rates of the various metal and oxide species. Keeping this limitation in mind, the time at which the Mo signal begins to appear can be used to establish an approximate length scale for the horizontal axis, as shown on the plot in Figure 20(b), since the initial film thickness is roughly known based on the QCM calibrations performed prior to the CSAF deposition. The XPS signal from the Mo substrate had appeared and was increasing with each additional Ar^+ etch cycle near the end of all but one of the depth profiles shown in Figure 20(a-i), indicating that the $Al_xFe_yNi_{1-x-y}$ CSAF was almost completely sputtered away at these locations and, therefore, that the profiles are representative of almost the entire CSAF cross section. XPS depth profiles measured on $Al_xFe_yNi_{1-x-y}$ CSAFs for $t_{ox} = 0$ h (before oxidation at elevated temperature) have shown that the initial distribution of elemental components is homogeneous across the film cross section. The profiles in Figure 20(a-i) show that the distribution has become very *in*homogeneous by $t_{ox} = 4$ h.

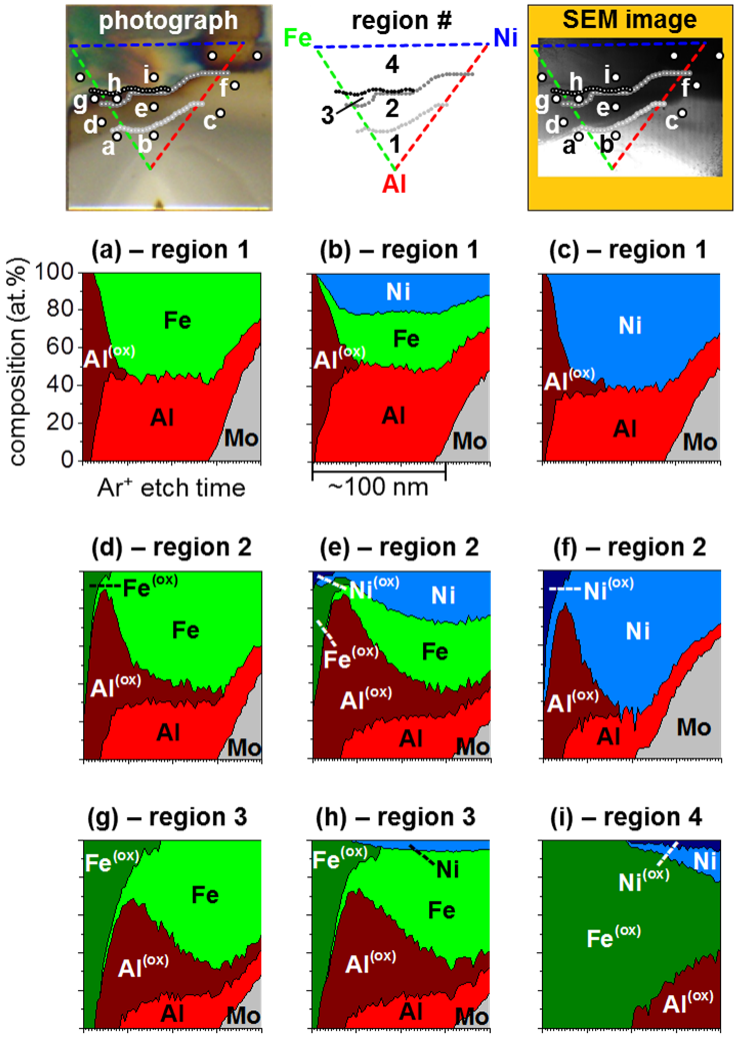

Figure 20. Top row: The 12 locations (white circles) at which XPS depth profiles were obtained shown on a photograph and an SEM image of an $Al_xFe_yNi_{1-x-y}$ CSAF (Mo substrate) after t_{ox} = 4 h in humid air at 427 °C. The triangular ternary-composition area with the regions identified by visual analysis is overlaid on each for reference. **(a)-(i)** The depth profiles obtained at the correspondingly labelled locations on the images. The plots show the relative atomic concentration of Al, Fe, Ni, and Mo in a metallic or oxidized state as determined from XPS spectra measured after each of the total Ar^+ etch times marked by the hashes on the horizontal axes. Qualitatively similar profiles were obtained within each of the visually distinct regions 1-4. The extent of oxidation appears to increase with increasing region number.

Important phenomenological distinctions can be made between the XPS depth profiles obtained in each of the regions 1-4. The profiles obtained in region 1, Figure 20(a, b, c), show a thin, continuous layer of oxidized Al at the CSAF surface, but no detectable oxidized Fe or Ni at any depth. The profiles from region 2, Figure 20(d, e, f), appear to show a very thin or partial layer of oxidized Fe and/or Ni at the

CSAF surface, below which there is a significant subsurface enrichment of oxidized Al. Below the point of greatest oxidized-Al enrichment, oxidized Fe and Ni are no longer present and the ratio of oxidized-to-metallic Al drops rapidly. The region 3 profiles, Figure 20(g, h), suggest a continuous layer of Fe oxide at the CSAF surface with subsurface enrichment of oxidized Al that is slightly less pronounced than in region 2. A small concentration of oxidized Fe was also detected in both region 3 profiles beyond the point of greatest oxidized Al enrichment. Finally, the region 4 profile, Figure 20(i), (although not indicative of the entire CSAF cross section, since Mo was not detected by the end of the profile) reveals a significantly higher amount of total oxide formation than at any of the other locations.

4.4. Discussion

4.4.1. Challenges related to interpretation of work

It is important to emphasize that that primary intent of the study described in this Chapter is to demonstrate our high-throughput methodology as a tool for screening environmental effects on alloy oxidation, for which we have used $Al_xFe_yNi_{1-x-y}$ at 427 °C as a model system. Experimental constraints associated with the RSM tool limit the thickness of $Al_xFe_yNi_{1-x-y}$ CSAFs that we can create, which consequently limits the oxidation temperature/time that can be reasonably studied. As a result, it must be recognized that the direct subject of this study is the oxidation of a very unique system, namely, ~100 nm-thick $Al_xFe_yNi_{1-x-y}$ films that were UHV annealed at 427 °C, exposed briefly to ambient air at room temperature during transfer, and then exposed to humid air at 427 °C for up to 4 h. Thus, interpreting the work as it might relate to other systems poses a number of challenges.

First, as mentioned previously, oxidation at 427 °C is very early/transient compared to oxidation at the much higher temperatures typically considered for alumina formers.[7,15,22,27] Practical alumina-forming alloys also contain additional components besides Al, Fe, and Ni, generally having a significant Cr content, and incorporating one or more of a number possible minor components, including Nb, Mo, Mn, W, Y, Hf, Ti, Si, and C, among others.[8,27,29,30] In principle, developing the ability to prepare much thicker CSAFs with more components could allow high-throughput methods similar to ours to be applied to oxidation studies of alloy composition ranges and oxidizing environments of direct industrial relevance, but this is beyond our current capabilities.

Even when limiting our study to early oxidation at 427 °C, it is unclear how closely the behavior of various locations on $Al_xFe_yNi_{1-x-y}$ CSAFs might mirror that of bulk alloys with equivalent compositions under identical conditions. One major reason for this is that there are likely to be significant differences in the grain structure of ~100 nm-thick alloy films compared to bulk alloys, and these differences might affect the oxidation process. A second reason that an $Al_xFe_yNi_{1-x-y}$ CSAF might oxidize differently from bulk alloys is if sufficient oxide formation occurs such that one or more metallic species are significantly depleted from the film, causing a change in its effective composition which affects the subsequent oxidation. Additional work performed to explore potential differences in the oxidation of bulk alloys and CSAFs will be discussed in Chapter 5.

The primary goal of the work described in this Chapter is simply to demonstrate the ability of our high-throughput methodology to reveal phenomenological differences in the oxidation occurring across the ternary $Al_xFe_yNi_{1-x-y}$ composition space in different environments. Specifically, we sought to determine whether an N_{Al}^* boundary between Al_2O_3-scale passivated and non-passivated compositions could be identified and, if so, whether this boundary was different for oxidation in humid air at 427 °C than that determined previously for oxidation in dry air at 427 °C (Chapter 3).[37] The remainder of the discussion in Chapter 4.4 proceeds as follows. Chapter 4.4.2 outlines our phenomenological characterization of the oxidation behavior of $Al_xFe_yNi_{1-x-y}$ CSAFs in humid air based on the EDX, Raman, and XPS results presented in Chapter 4.3. In Chapter 4.4.3, we compare these results to those from our previous study of oxidation in dry air (Chapter 3). Finally, in Chapters 4.4.4 through 4.4.7, we propose a modified version of the Wagner-Maak model[34,35] (Chapter 1.5) and use it to consider whether our studies of early oxidation of $Al_xFe_yNi_{1-x-y}$ CSAFs at 427 °C can offer insights into the physical factors controlling the value of N_{Al}^* in humid vs. dry environments that might also relate to the oxidation of bulk alumina formers at higher temperatures.

4.4.2. Oxidation behavior of $Al_xFe_yNi_{1-x-y}$ CSAFs in humid air at 427 °C

The primary goal of the work described in this Chapter was to identify phenomenological differences in early oxidation behavior across $Al_xFe_yNi_{1-x-y}$ composition space in humid air at 427 °C and to compare this behavior to that for oxidation in dry air at 427 °C (Chapter 3).[37] In both cases, we are

ultimately able to directly measure a continuous N_{Al}^{*} boundary, which appears to be the minimum N_{Al} required for the initial establishment of a passivating Al_2O_3 scale during early oxidation at 427 °C. As in our dry-air study, we observed correlations between visually identifiable boundaries on $Al_xFe_yNi_{1-x-y}$ CSAFs oxidized in humid air and transitions between phenomenologically distinct types of oxidation behavior. The types of behavior that we propose for the visually distinct regions 1-4 are the same as those shown for the dry air study in Figure 12. The schematics in Figure 12 are not presented as rigorously detailed mechanisms for the regions, but are simply meant to emphasize qualitative differences we are able to detect with our characterization methods.

Region 1 contains compositions which were passivated by an exclusive, surface Al_2O_3 scale (Figure 12). The XPS depth profiles from this region (Figure 20(a, b, c)) show that a thin layer (perhaps ~2-4 nm) of continuous oxidized Al is present at the surface of the CSAF, but the majority of the film's cross section remains metallic and uniform in composition. Given the oxidation conditions used in this study, the oxidized Al is likely amorphous Al_2O_3 and/or γ-Al_2O_3, as discussed in Chapter 3.3.4. The EDX measurements of oxygen uptake (Figure 17) revealed that $\Delta C_{\mathrm{O}} \cong 0$ across region 1 for all $t_{ox} > 0$ h, indicating that the compositions in region 1 were passivated against oxidation for the entire 4 h exposure to humid air at 427 °C, and suggesting that the Al_2O_3 was primarily formed during the brief exposure to ambient air at room temperature upon removal from the UHV deposition chamber. The $C_{\mathrm{O}}(t_{ox} = 4\ \mathrm{h})$ in region 1 is the lowest of the four regions because oxygen is only present in the relatively small amount of Al_2O_3 that was formed at the CSAF surface. As mentioned in Chapter 3.3.4, any Al_2O_3 formed in the CSAFs at 427 °C would not be expected to be Raman-active, which is consistent with the lack of peaks in the Raman spectra measured in region 1 (Figure 19).

The spectroscopic data from region 2 of the CSAFs are consistent with trace Fe and/or Ni oxides on top of a continuous, subsurface Al_2O_3 scale (Figure 12). The depth profiles (Figure 20(d, e, f)) show an initially high concentration of oxidized Fe and/or Ni that rapidly diminishes over the first few etch cycles, revealing a high degree of oxidized Al enrichment in the subsurface. The oxidized Al signal at and below the depth of greatest enrichment must originate primarily from Al_2O_3, as opposed to mixed Al oxides, since Al is the only oxidized species present in a significant concentration. If the enrichment of oxidized Al is assumed to indicate a thin, continuous layer of subsurface Al_2O_3, then the fact that the

depth profiles do not directly reveal a point of 100% oxidized Al in the subsurface suggests that there are lateral variations in the thickness of the Fe/Ni oxides at the surface (potentially to the extent that the Fe/Ni oxides are present as isolated clusters on the Al_2O_3). This type of morphology would prevent the continuous Al_2O_3 scale from being simultaneously exposed to XPS during uniform Ar^+ etching. Given this interpretation of the oxidation behavior of region 2, the reason for the persistence of a small fraction of oxidized Al at greater depths where the majority of the film cross section is metallic is uncertain; it may arise due to complexities of the CSAF grain structure, e.g. perhaps as the result of Al_2O_3 formation along grain boundaries. The oxygen uptake measurements (Figure 17), which show $\Delta C_O \cong 0$ from $t_{ox} = 1$ to 4 h, indicate that region 2 became passivated against further oxidation and, therefore, suggest that a continuous Al_2O_3 layer was indeed formed. The $C_O(t_{ox} = 4\text{ h})$ is slightly higher in region 2 than in region 1 because of the additional oxygen contained in the trace Fe/Ni oxides. The small, measurable values of ΔC_O from $t_{ox} = 0$ to 1 h shows that some of the oxide formation occurred in the humid air at 427 °C before region 2 was passivated. The $NiFe_2O_4$ phase was detected with Raman spectroscopy (Figure 19) at two of the sampled locations in region 2, but the majority of spectra did not show any peaks, likely because the amount of Fe and/or Ni oxide that was formed was too small to be detected.

Region 3 exhibits oxygen uptake trends (Figure 17) that are nearly identical to region 2: ΔC_O is small, but measurable from $t_{ox} = 0$ to 1 h and $\Delta C_O \cong 0$ from $t_{ox} = 1$ to 4 h. The total $C_O(t_{ox} = 4\text{ h})$ is also very similar in both regions. These results suggest that region 3 compositions are also passivated; however, the depth profiles (Figure 20(g, h)) show a slightly lower extent of oxidized-Al enrichment in the subsurface than in region 2, with a continuous layer of oxidized Fe on the CSAF surface. The α-Fe_2O_3 phase was identified with Raman spectroscopy (Figure 19) across all of region 3. Qualitatively equivalent spectroscopic data were obtained across the much larger composition region 3 during our study of $Al_xFe_yNi_{1-x-y}$ CSAF oxidation in dry air at 427 °C, as described in Chapter 3.[37] The most likely interpretation is that the compositions in region 3, like region 2, formed a continuous, passivating Al_2O_3 scale in the subsurface (Figure 12). However, based on the Raman results, the competitive oxide in region 3 appears specifically to be α-Fe_2O_3. Furthermore, the seemingly lower subsurface enrichment of oxidized Al in the XPS depth profiles suggests that there is more variability in the thickness of this competitive oxide in region 3 than in region 2.

Region 4 compositions appear to have experienced internal oxidation in the humid air at 427 °C (Figure 12). The oxygen uptake data (Figure 17) show that $C_{\mathrm{O}}(t_{ox} = 4\ \mathrm{h})$ is significantly higher across the majority of region 4 than in any of the other regions. The amplified plot of ΔC_{O} from $t_{ox} = 1$ to 4 h demonstrates clearly that continuing oxygen uptake during this time is exclusively measurable throughout region 4, indicating that passivation did not occur. The depth profile in Figure 20(i) shows that Fe was oxidized extensively, and is very similar in appearance to the depth profile (not included) from the analysis location in the AlFe binary area of region 4 in Figure 20. The two depth profiles (also not included) from near the pure-Ni corner in region 4 revealed significantly less oxidation overall, but did not show any degree of oxidized-Al enrichment in the CSAF cross section that could be indicative of Al_2O_3 scale formation. The Raman analysis (Figure 19) reveals α-Fe_2O_3 transitioning to $NiFe_2O_4$ as the Fe-to-Ni ratio decreases across composition region 4. The appearance of the $NiFe_2O_4$ phase appears to correlate roughly with a rapid decrease in $C_{\mathrm{O}}(t_{ox} = 4\ \mathrm{h})$ across region 4. Based on the spectroscopic results, we believe that the decrease in $C_{\mathrm{O}}(t_{ox} = 4\ \mathrm{h})$ as the Fe-to-Ni ratio decreases across region 4 is the result of "pseudo-passivation" (i.e. a very slow growth rate at 427 °C) by $NiFe_2O_4$ and/or NiO, but is not attributable to any type of Al_2O_3 scale formation.

The regions described above subdivide the entire $Al_xFe_yNi_{1-x-y}$ composition space into four phenomenologically distinguishable types of oxidation behavior that were observed to occur on CSAFs as a result of oxidation in humid air at 427 °C (Figure 12). Composition regions 1, 2, and 3 all become rapidly passivated against oxidation under these conditions due to the formation of an Al_2O_3 scale, but the oxide morphology in each case is unique. In region 1, the Al_2O_3 is exclusive and continuous at the surface of the CSAF. In region 2, the Al_2O_3 forms a continuous layer beneath trace Fe and/or Ni oxides. In region 3, there appears to be a continuous Al_2O_3 layer in the subsurface beneath variable-thickness α-Fe_2O_3. The compositions in region 4 were not able to establish an Al_2O_3 scale and underwent internal oxidation at a wide range of rates depending on the type of Fe/Ni oxide(s) that were formed. Thus, the boundary of region 4 defines the trajectory of N_{Al}^{*} across $Al_xFe_yNi_{1-x-y}$ composition space for oxidation in the humid air at 427 °C. The N_{Al}^{*} boundary was found to follow a complex path from $Al_{0.35}Fe_{0.65}$ to $Al_{0.22}Ni_{0.78}$, with the minimum being $Al_{0.22}Ni_{0.78}$ and reaching a maximum at $Al_{0.38}Fe_{0.56}Ni_{0.06}$.

4.4.3. Comparison of $Al_xFe_yNi_{1-x-y}$ CSAF oxidation in dry and humid air at 427 °C

The same four types of oxidation behavior (see Figure 12) were identified for regions 1-4 of $Al_xFe_yNi_{1-x-y}$ CSAFs exposed to humid air at 427 °C as for regions 1-4 of $Al_xFe_yNi_{1-x-y}$ CSAFs exposed to dry air at 427 °C (Chapter 3).[37] Thus, the results of the two studies can be directly compared. Figure 21 shows a photograph, the C_O measured by EDX, and the Raman phase map for one CSAF exposed to dry air and one exposed to humid air, each for $t_{ox} = 4$ h. While many aspects of the visual appearance (Figure 21(a)) are similar in the two cases, there are significant differences in the surface coloration patterns in regions 3 and 4. By comparing $C_O(t_{ox} = 4$ h) in the ternary composition diagrams (Figure 21(b)), it is immediately apparent that the rapid increase in C_O upon crossing into region 4 (correlating to the transition from internal to external oxidation) is shifted to significantly higher Al contents at high Fe-to-Ni ratios for the CSAF exposed to humid air. While the C_O plots suggest that certain compositions are oxidized to a markedly different extent in the two different environments, the Raman phase maps (Figure 21(c)) show that the oxide phases that are formed in the different regions of composition space in either case are quite similar. The overall strength of the Raman signal measured at the various surface locations was observed to be substantially higher for the CSAF oxidized in dry air than for the CSAF oxidized in humid air, despite identical acquisition conditions. The reason for this difference is not known, but the much lower signal-to-noise ratio in the data collected on the CSAF oxidized in humid air may have prevented identification of spectra that were definitively characteristic of NiO along the AlNi binary of region 4, as the single peak assigned to NiO in the dry-air study was low and broad compared to those observed for the other oxide phases (see Figure 10).

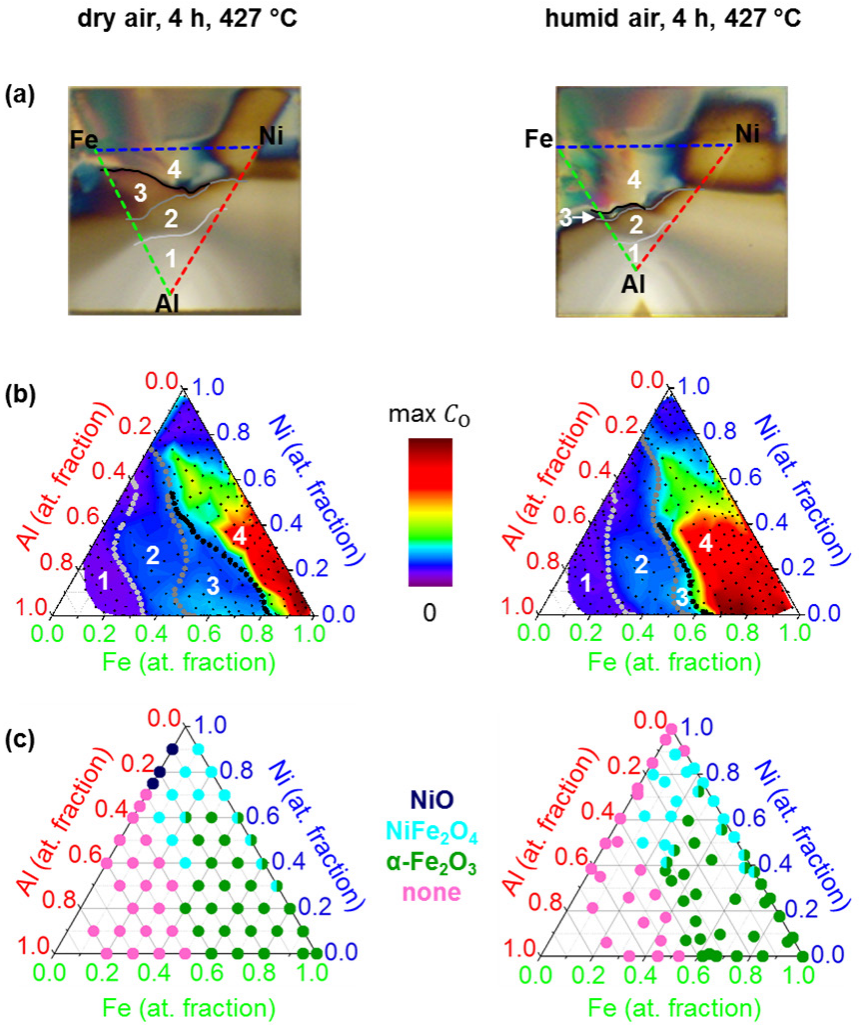

Figure 21. A comparison of key results from the studies of $Al_xFe_yNi_{1-x-y}$ CSAFs oxidized in dry air (left) and humid air (right). **(a)** Photographs of the CSAFs after exposure to their respective environment for $t_{ox} = 4$ h. The ternary-composition areas and visually identified boundaries between composition regions 1-4 are overlaid for reference. **(b)** Composition maps of $C_O(t_{ox} = 4$ h) in the two environments with the regions identified by visual analysis overlaid for reference. The high C_O values associated with region 4 extend across a notably larger fraction of composition space for oxidation in humid air. **(c)** Composition maps of the types oxide phases identified with Raman spectroscopy after $t_{ox} = 4$ h. The maps are very similar for the two different environments. The points on the humid-air map were chosen at real-space locations of interest on the CSAF surface and, thus, are not uniformly distributed in composition space.

The depth resolution of the XPS depth profiles presented in this Chapter (Figure 20) is higher by a factor of ~3× than that of those obtained for the study of CSAF oxidation in dry air (Figure 11). Depth profiles are not directly compared in Figure 21, but the key qualitative features of the oxide/metal cross sections (as described in Chapters 3.4 and 4.4.2) were the same within each corresponding region, 1-4, of the CSAFs oxidized in the two different environments. While the procedure for peak fitting the XPS

data obtained from the humid-air oxidized CSAF (described in Chapter 4.2.4) was slightly more sophisticated than that used for peak fitting the XPS data obtained from the dry-air oxidized CSAF (described in Chapter 3.2.4), both procedures were found to give very similar results. The calculated ratio of oxidized-to-metallic species is marginally lower when using the procedure described in this Chapter, i.e. fitting the metallic peaks with a slight tail at higher binding energies (see Table 2 and Figure 14). However, the qualitative aspects of the resulting profiles which are used to infer oxidation phenomenology remain unchanged regardless of which peak-fitting procedure is used.

The results of our spectroscopic analyses of $Al_xFe_yNi_{1-x-y}$ CSAFs suggest that the four types of phenomenologically distinguishable oxidation behavior shown in Figure 12 occur in both dry air and humid air at 427 °C. Figure 22 shows a comparison of the composition-space boundaries separating regions 1-4 in each case. The boundaries are plotted in a rectangular representation of $Al_xFe_yNi_{1-x-y}$ composition space with N_{Al} plotted as a function of N_{Fe} / (N_{Fe} + N_{Ni}). The vertical and horizontal error bars show uncertainty in position based on the precision of the visual boundary identification. From this comparison, it can be seen that the only measurably significant difference between the two oxidizing environments is a shift in the boundary between regions 3 and 4. Region 3 is significantly narrower for oxidation in humid air than in dry air, being largely supplanted by an expansion of region 4. Thus, the only relevant difference between the two environments is in the subset of the N_{Al}^{*} boundary which separates regions 3 and 4. Figure 23 shows a comparison of the N_{Al}^{*} boundaries determined for exposure at 427 °C to dry air and to humid air. The boundaries are plotted in both the rectangular representation of $Al_xFe_yNi_{1-x-y}$ composition space with error bars, and in a typical ternary composition diagram without error bars. At low Fe-to-Ni ratios, the value of N_{Al}^{*} is approximately constant at ~0.23 in both environments. The two N_{Al}^{*} boundaries begin to measurably diverge at N_{Fe} / (N_{Fe} + N_{Ni}) ≅ 0.35. The magnitude of this divergence increases rapidly beginning at ~0.55, and appears to reach a maximum at ~0.90, where N_{Al}^{*} ≅ 0.15 in dry air and N_{Al}^{*} ≅ 0.38 in humid air. As demonstrated in Figure 22, the increase of N_{Al}^{*} in humid air compared to dry air appears to manifest itself as a collapsing of region 3 in favor of region 4, i.e. many $Al_xFe_yNi_{1-x-y}$ CSAF compositions which are passivated by a subsurface Al_2O_3 scale beneath a continuous surface layer of α-Fe_2O_3 as a result of oxidation in dry air at 427 °C instead experience extensive internal oxidation when exposed to humid air at 427 °C.

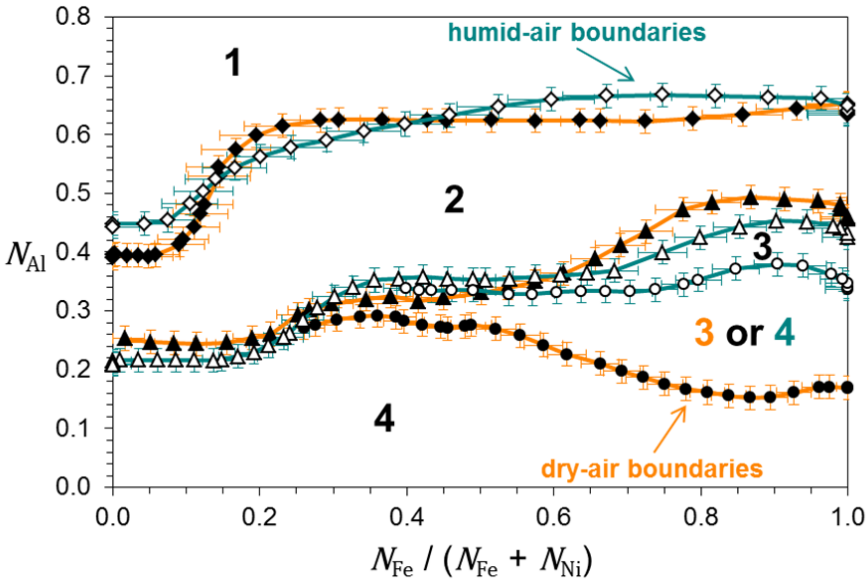

Figure 22. A comparison of the boundaries between composition regions exhibiting different types of oxidation behavior determined by visual analysis of $Al_xFe_yNi_{1-x-y}$ CSAFs oxidized at 427 °C in either dry or humid air. The boundaries are plotted in composition space with Al atomic fraction as a function of the relative Fe atomic fraction compared to Ni. The error bars are representative of the experimental uncertainty of the visual analysis technique. The only measurably significant difference between the two environments is the shift of the boundary between regions 3 and 4 to higher N_{Al} values for humid air compared to dry air.

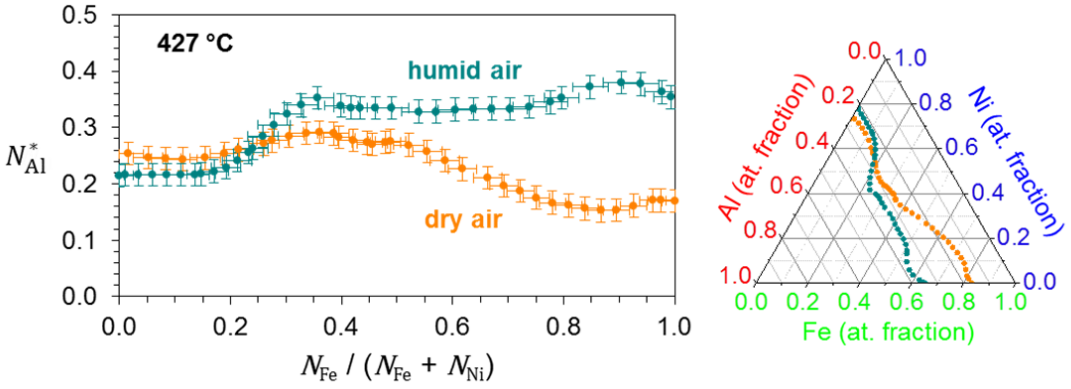

Figure 23. A comparison of N^*_{Al} in dry air and humid air at 427 °C as determined by high-throughput experimentation using $Al_xFe_yNi_{1-x-y}$ CSAFs. **Left:** The N^*_{Al} comparison in a rectangular representation of $Al_xFe_yNi_{1-x-y}$ composition space with Al atomic fraction as a function of the relative Fe atomic fraction compared to Ni. The error bars show the measurement uncertainty in the trajectory of the boundaries. **Right:** The N^*_{Al} comparison on a standard ternary composition diagram. Measurement uncertainty is not represented, but is shown in the plot at left.

4.4.4. Modified Wagner-Maak model

The measured trajectories of N_{Al}^{*} shown in Figure 23 appear to be the minimum Al content required for initial establishment of a continuous, protective Al_2O_3 scale in $Al_xFe_yNi_{1-x-y}$ alloys at 427 °C. We now attempt to analyze our results in terms the Wagner-Maak kinetic model[34,35] (introduced in Chapter 1.5) to consider whether they can offer insights into the physical origins of the composition- and humidity-dependent variations in the value of N_{Al}^{*} observed for oxidation of $Al_xFe_yNi_{1-x-y}$ CSAFs at 427 °C, which may also relate to the oxidation of bulk alloys at higher temperatures. Because the model describes oxidation based on one-dimensional counter-diffusion of oxygen against the alloy component that is oxidized to form the passivating scale, applicability of the model requires that the oxidation process be controlled by diffusion. Whether or not this is the case for our studies of $Al_xFe_yNi_{1-x-y}$ CSAF oxidation at 427 °C will be discussed in more detail in Chapter 4.4.5. Acknowledging this possible limitation, we move forward in considering how the model might be applied to interpreting our results.

Accepting its simplifying assumptions, the Wagner-Maak model produces a physically intuitive description of the internal oxidation mechanism shown in Figure 3, provided that the values of N_{Al}^{*} and g^{*} are small. However, clearly unphysical situations are predicted when considering limiting values of N_{Al}^{*} and g^{*}, which lead us to make two minor modifications to the definitions of these parameters used in the Wagner-Maak model before attempting to use it to analyze the results of our CSAF oxidation studies.

The first modification is to the relationship established in Equation 1.16 between the critical AlO_v volume fraction, g^{*}, and the AlO_v mole fraction, N_{AlO_v}. For a fixed number of moles in a system of only immiscible AlO_v and M, the precise relationship between a defined value of g^{*} and N_{AlO_v} is

$$N_{\mathrm{AlO}_v} = \left(\frac{g^{*}V_{\mathrm{M}}}{V_{ox}+g^{*}V_{\mathrm{M}}-g^{*}V_{ox}}\right) \qquad (4.1).$$

If V_{M} and V_{ox} differ significantly, Equation 1.16 is approximately equivalent to Equation 4.1 only when the value of g^{*} is small. Figure 24 shows a comparison of the relationship between N_{AlO_v} and g^{*} according to Equations 1.16 and 4.1 when $V_{ox} = 1.9V_{\mathrm{M}}$ (representative of the approximate molar volume ratio for an $AlO_{1.5}$ and Ni binary system). The values of N_{AlO_v} predicted by the two equations diverge as the value of

g^* increases. As a consequence of using Equation 1.16, the actual value of N_{AlO_ν} that corresponds to a specific value of g^* is increasingly underestimated as g^* increases. The Wagner-Maak model assumes that N_{AlO_ν} is equal to the effective Al mole fraction obtained due to diffusive Al enrichment at $z = \xi$ immediately before the Al_2O_3 is formed (i.e. $N_{\mathrm{AlO}_\nu} = \alpha N_{\mathrm{Al}}^{(0)}$). Under this assumption, N_{Al}^* will also be increasingly underestimated as g^* increases as a result of using Equation 1.16. From a practical standpoint, it has been shown by Yi et al.[62] that stresses resulting from volume expansion during Al_2O_3 formation in AlNi alloys cause preferential displacement of Ni to the alloy surface, which would offset this error since the resulting N_{AlO_ν} in the subsurface would actually be greater than $\alpha N_{\mathrm{Al}}^{(0)}$. However, the extent to which preferential displacement of M might factor into other AlM systems is not clear. Furthermore, Equation 4.1 sets a physically intuitive limiting bound as $g^* \rightarrow 1$, requiring that an Al_2O_3 volume fraction of 1 correspond to an Al_2O_3 mole fraction of 1.

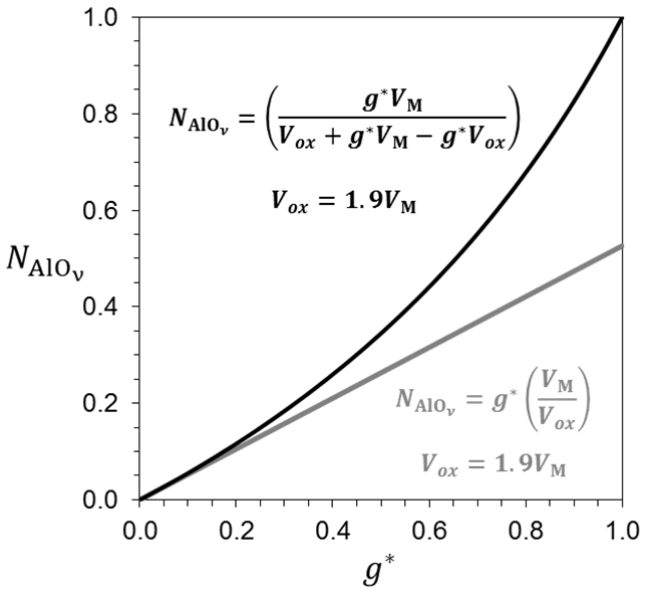

Figure 24. Plot showing the N_{AlO_ν} (mole fraction of AlO_v in an M/AlO_v mixture) corresponding to different values of g^* (the critical volume fraction of AlO_v in an M/AlO_v mixture) according to Equation 1.16 (grey) and Equation 4.1 (black) for a system in which $V_{ox} = 1.9 V_{\mathrm{M}}$.

Our second modification to the Wagner-Maak model relates to how the diffusive enrichment of Al is defined. Writing Equation 1.4 in terms of Al mole fraction is appropriate when the value of $N_{\mathrm{Al}}^{(0)}$ is small.

However, given the model's assumption that the M matrix is immobile, this treatment becomes increasingly erroneous as the value of either $N_{\mathrm{Al}}^{(0)}$ or α increases. For example, even if Equation 4.1 is used in place of Equation 1.16, the limiting case where $g^* = N_{\mathrm{AlO}_\nu} = 1$ can still result in counterintuitive solutions where $\alpha > 1$, and $N_{\mathrm{Al}}^* < 1$ as a result. This concern can be addressed by writing Equations 1.3-1.8, 1.11, and 1.13 in terms of concentrations rather than mole fractions, i.e. by replacing all instances of N with c, where c_i is the concentration of species i in units of moles per volume. Equation 1.12 then becomes

$$\frac{c_{\mathrm{O}}^{(\mathrm{s})}}{\nu c_{\mathrm{Al}}^{(0)}} = \frac{\mathrm{erf}(\gamma)-\mathrm{erf}(u)}{\mathrm{erf}(\gamma)} \frac{\mathrm{G}(\gamma)}{\mathrm{F}(\gamma\varphi^{1/2})} \tag{4.2}$$

where $\mathrm{G}(\gamma)$ and $\mathrm{F}(\gamma\varphi^{1/2})$ are defined as before. Likewise, Equation 1.14 becomes

$$c_{\mathrm{AlO}_\nu} = \frac{c_{\mathrm{Al}}^{(0)}}{\mathrm{F}(\gamma\varphi^{1/2})} \tag{4.3}$$

and the Al enrichment factor, formerly expressed by Equation 1.15, is now defined as

$$\alpha = \frac{c_{\mathrm{AlO}_\nu}}{c_{\mathrm{Al}}^{(0)}} = \frac{1}{\mathrm{F}(\gamma\varphi^{1/2})} \tag{4.4}.$$

Equations 4.2-4.4 can be rewritten in terms of mole fractions by assuming

$$N_{\mathrm{Al}} = \frac{c_{\mathrm{Al}}}{c_{\mathrm{Al}}+c_{\mathrm{M}}} \tag{4.5}$$

where c_{M} is the molar concentration of immobile M in the metallic matrix. Neglecting volume expansion due to diffusive Al enrichment, the value of c_{M} can be assumed to be constant. It is reasonable to assume that $N_{\mathrm{O}}^{(\mathrm{s})} \ll 1$, so N_{O} can be accurately approximated as

$$N_{\mathrm{O}} = \frac{c_{\mathrm{O}}}{c_{\mathrm{M}}} \qquad (4.6).$$

Equations 4.1-4.6 can be combined and rearranged to yield a modified Wagner-Maak model of the form

$$\frac{N^*_{\mathrm{Al}}}{N^*_{\mathrm{Al}}+\mathrm{F}(\gamma\varphi^{1/2})(1-N^*_{\mathrm{Al}})} = \frac{g^* V_{\mathrm{M}}}{V_{ox}+g^* V_{\mathrm{M}}-g^* V_{ox}} \qquad (4.7)$$

$$\frac{N^{(\mathrm{s})}_{\mathrm{O}}(1-N^*_{\mathrm{Al}})}{\nu N^*_{\mathrm{Al}}} = \frac{\mathrm{erf}(\gamma)-\mathrm{erf}(u)}{\mathrm{erf}(\gamma)}\frac{\mathrm{G}(\gamma)}{\mathrm{F}(\gamma\varphi^{1/2})} \qquad (4.8).$$

As with the unmodified Wagner-Maak model (Equations 1.17 and 1.18), Equations 4.7 and 4.8 can be solved simultaneously for any two of the variables N^*_{Al}, $N^{(\mathrm{s})}_{\mathrm{O}}$, D_{O}, D_{Al}, g^*, k_c, V_{M}, V_{ox}, ν, and γ, given appropriate values of the others. Inspection of Equations 4.7 and 4.8 reveals that they become equivalent to Equations 1.17 and 1.18 in the limit of small values of N^*_{Al} and g^*. In practice, the predictions of the modified and unmodified Wagner-Maak models are fairly similar for small to moderate values of these variables. Neither model incorporates details of volume expansion related to oxide formation or Al diffusion, but the modified form has the advantage of forcing the intuitively correct limiting solution that $N^*_{\mathrm{Al}} \rightarrow 1$ as the specified value of $g^* \rightarrow 1$.

4.4.5. Applicability of Wagner-Maak model to $Al_xFe_yNi_{1-x-y}$ CSAF oxidation

A number of the details of the Wagner-Maak model must be considered to assess its ability to describe the results of our oxidation studies on $Al_xFe_yNi_{1-x-y}$ CSAFs. Most importantly, as stated earlier, the oxidation process must be diffusion-controlled for the model to apply. Typically, it has been applied to alloy systems at temperatures >800 °C where this is known to be the case. The best indication of whether diffusion is also controlling the oxidation of our $Al_xFe_yNi_{1-x-y}$ CSAFs at 427 °C would be if our measurements of C_{O} vs. time exhibited parabolic trends. However, due to practical limitations of these measurements (primarily the reasonably achievable number and spacing of time points), it is not possible for us to definitively determine whether or not this is so. We proceed recognizing the possibility that, if the

oxidation process is driven by a mechanism other than diffusion in our $Al_xFe_yNi_{1-x-y}$ CSAFs at 427 °C, the conclusions drawn by analysis using any Wagner-Maak-based model may not be accurate.

Another important point is that for an alloy with a subcritical Al content, the Wagner-Maak model predicts ongoing, time-dependent internal oxidation as depicted in Figure 3 (based on the variables $N_{\mathrm{Al}}^{(0)}$, $N_{\mathrm{O}}^{(\mathrm{s})}$, D_{O}, D_{Al}, k_c, ν, and γ as defined by Equations 1.1, 1.2, and 1.12). Thus, for the oxidation behavior of the $Al_xFe_yNi_{1-x-y}$ CSAFs to be consistent with the Wagner-Maak model requires that the oxide cross section for $N_{\mathrm{Al}}^{(0)} < N_{\mathrm{Al}}^{*}$ resemble that shown in Figure 3. This appears to be generally consistent with the XPS depth profile shown in Figure 20(i) of one such location on a CSAF oxidized in humid air. The profile reveals a continuous layer of competitive Fe oxide at the CSAF surface, transitioning to a combination of oxidized Fe and oxidized Al with increasing depth. It is not necessary that the profile reveal regions corresponding to $X \leq z \leq \xi$ and $z \geq \xi$ in Figure 3 to be consistent with this description of oxidation behavior, since ξ and X must eventually exceed the limits of the initial CSAF thickness if passivation does not occur. It should be noted that the surface layer of 100% MO_β shown for $z < 0$ in Figure 3 is not directly described in the mathematics of the Wagner-Maak model, although it is a well-known feature of the oxide morphology developed on AlM alloys when M can be oxidized and $N_{\mathrm{Al}}^{(0)} < N_{\mathrm{Al}}^{*}$.[10,12,58] Based on the model's assumption that an oxygen mole fraction $N_{\mathrm{O}}^{(\mathrm{s})}$ is maintained at X for all $t > 0$, the impact of the competitive MO_β formation on the predicted value of N_{Al}^{*} depends solely on the value of k_c, which describes only the growth of the inner part of the MO_β scale. Practically speaking, the thickness of the outer MO_β scale and the value of k_c will be related.

Given that the Wagner-Maak model is derived based on the assumption of a semi-infinite bulk, it is also prudent to consider whether preferential depletion of one or more metallic components from the non-infinite CSAF during oxide formation might affect its assumptions or boundary conditions. This possibility was investigated and will be discussed further in Chapter 5. We have found that depletion does not appear to be significant in the regions of the CSAFs where Al_2O_3 passivation occurs for $t_{ox} \leq 4$ h at 427 °C. Since our CSAF studies reveal a clear transition from passivated to non-passivated compositions, and our goal is simply to use the Wagner-Maak model to gain insights related to the N_{Al}^{*} where this transition takes place, it appears that concerns related to depletion effects are minimal.

Finally, it is important to recall that the Wagner-Maak model is only related to N_{Al}^{*} by Wagner's assumption regarding g, the volume fraction of Al_2O_3 formed in the IOZ. If $g < g^{*}$, precipitate blocking of oxygen diffusion is assumed to be negligible, but if $g \geq g^{*}$, it is assumed to be the controlling factor that causes a passivating scale to be established. Thus, the strict physical picture of the model is that an AlM alloy with $N_{\mathrm{Al}}^{(0)} < N_{\mathrm{Al}}^{*}$ will experience ongoing internal oxidation with a morphology like that shown in Figure 3, while an alloy with $N_{\mathrm{Al}}^{(0)} \geq N_{\mathrm{Al}}^{*}$ will develop a passivating Al_2O_3 scale instead. In this respect, the results of our oxidation studies are also quite consistent with the model, as we have been able to observe sharply defined N_{Al}^{*} boundaries on the $Al_xFe_yNi_{1-x-y}$ CSAFs. This is particularly well illustrated by the plot of $C_{\mathrm{O}}(t_{ox} = 4\ \mathrm{h})$ in Figure 17, which shows that the total oxygen uptake into the CSAF was increased by a factor of ~4× over a range of just a few at.% Al upon transitioning from the passivated region 3 to the non-passivated region 4. No distinction is made by the Wagner-Maak model as to whether the passivating Al_2O_3 scale will be established at the surface or in the subsurface if $N_{\mathrm{Al}}^{(0)} \geq N_{\mathrm{Al}}^{*}$.

Although the basic physical picture of the Wagner-Maak model appears to be essentially correct for diffusion-controlled oxidation, it has never been demonstrated that it can provide predictions of the value of N_{Al}^{*} that are sufficiently accurate for alloy design, even in alloy systems where this is definitively known to occur. This is likely due, in part, to difficulties associated with accurately determining the values of the various kinetic parameters contained in the model. The parameters, as described in the derivation of Equations 1.17 and 1.18, would be most appropriately applied to modelling the oxidation of a large AlM single crystal where $N_{\mathrm{Al}}^{(0)}$ is small. However, complications arise when considering less ideal systems. For example, in a polycrystalline alloy, oxygen and Al are likely to diffuse at different rates through the crystalline matrix, at grain boundaries, and/or along Al_2O_3/M interfaces.[63,64] Furthermore, certain AlM alloy compositions form coexisting phases which could have significantly different local compositions and/or kinetic properties. The Wagner-Maak model can only be quantitatively accurate if it is possible to determine an appropriate "effective value" for each kinetic parameter which accounts for these types of effects. However, for the purposes of analyzing our CSAF data, this also means that the model can be extended from binary AlM to consider the more complex AlFeNi system if M is assumed to be a variable mixture of Fe and Ni, where these effective parameter values depend on the Fe-to-Ni ratio.

4.4.6. Sensitivity analysis of parameters in modified Wagner-Maak model

Without known values for the parameters $N_{\mathrm{O}}^{(s)}$, D_{O}, D_{Al}, k_c, and g^*, we performed a simple sensitivity analysis to investigate their influence on the value of N_{Al}^* predicted by the modified Wagner-Maak model. This sensitivity analysis is not a mathematically rigorous screening of the full parameter space but, rather, is intended to provide physical insights into the effects of each parameter. For the analysis, we chose wide ranges of possible "effective values" of these parameters for $Al_xFe_yNi_{1-x-y}$ oxidation at 427 °C. Equations 4.7 and 4.8 were then repeatedly solved to find N_{Al}^* and γ across the range of values selected for each parameter while holding all of the other variables constant at a chosen set of base values. The base value and range for each variable are shown in Table 3. The base values of V_{M} and V_{ox} in Table 3 correspond to the approximate molar volumes at 427 °C of metallic Ni and $AlO_{1.5}$, respectively. The value of ν was taken as 1.5 (the stoichiometric ratio of oxygen-to-Al in Al_2O_3). The base values of $N_{\mathrm{O}}^{(s)}$, D_{O}, and D_{Al} are intended to be roughly appropriate for a Ni single-crystal matrix in equilibrium with NiO at 427 °C, and were obtained by extrapolating (to the nearest order of magnitude) from temperature dependences of these parameters that have been measured by other authors.[65–68] The base value of k_c was then chosen (to the nearest order of magnitude) to maximize the sensitivity of the predicted value of N_{Al}^* to small changes in the value of k_c. Finally, the base value of g^* was chosen such that the N_{Al}^* predicted using the complete set of base values in Table 3 was in agreement with that which we experimentally observed at the AlNi binary using the $Al_xFe_yNi_{1-x-y}$ CSAFs (as shown in Figure 23, this N_{Al}^* value was very similar in both the dry-air and humid-air environments).

Table 3. Values used for sensitivity analysis of modified Wagner-Maak model.

variable	base value	range	refs.
$N_{\mathrm{O}}^{(s)}$	10^{-5}	10^{-8} – 10^{-2}	65,66
D_{O}	10^{-14} cm^2/s	10^{-17} – 10^{-11}	65,66
D_{Al}	10^{-19} cm^2/s	10^{-22} – 10^{-16}	67,68
k_c	10^{-19} cm^2/s	10^{-22} – 10^{-16}	–
g^*	0.40	0.00 – 1.00	–
V_{M}	6.7 cm^3/mol	n/a	–
V_{ox}	12.7 cm^3/mol	n/a	–
ν	1.5	n/a	–

Plots of the N_{Al}^{*} predicted by the modified Wagner-Maak model across the ranges of values for $N_{\mathrm{O}}^{(\mathrm{s})}$, D_{O}, D_{Al}, k_c, and g^{*} shown in Table 3 are presented in Figure 25. The point shown as an open circle on each plot indicates the N_{Al}^{*} calculated for the complete set of base values shown in Table 3. The solid points show the N_{Al}^{*} calculated for different values of the parameter on the horizontal axis while holding all of the other parameters constant at their base values. The modified functional form of the Wagner-Maak model was used because of the extreme limiting values that were considered for g^{*}. As mentioned earlier, the predictions of the modified and unmodified model are similar unless the values of g^{*} or N_{Al}^{*} are large, and thus the plot of N_{Al}^{*} vs. g^{*} (Figure 25(e)) is the only one that is significantly affected by the choice of the modified model (the unmodified-model solutions converge to $N_{\mathrm{Al}}^{*} \cong 0.43$ at $g^{*} = 1$, rather than $N_{\mathrm{Al}}^{*} = 1$). The predicted N_{Al}^{*} values shown on the other plots (Figure 25(a-d)) are systematically decreased by between 0.03 and 0.05 if the unmodified model is used, but the general trends remain identical. The plots in Figure 25 allow assessment of the manner in which the effective values of the kinetic parameters of the modified Wagner-Maak model affect the predicted value of N_{Al}^{*}.

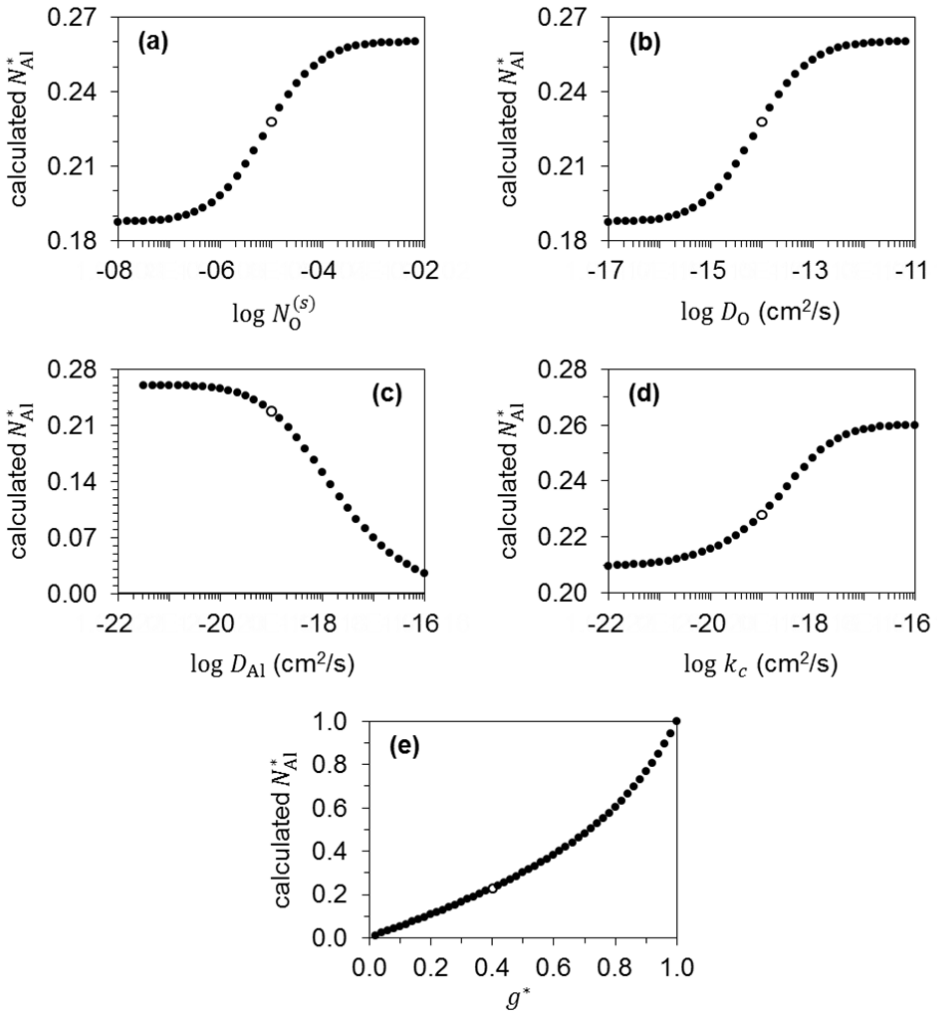

Figure 25. Plots showing the calculated value of N_{Al}^* for a range of values of different variables in the modified Wagner-Maak criterion with the others held at the base values shown in Table 3. The point shown as an open circle on each plot represents the solution when all the variables are set to the base values. **(a)** Semi-log plot showing the effect of changing the value of $N_{\mathrm{O}}^{(s)}$. **(b)** Semi-log plot showing the effect of changing the value of D_{O}. **(c)** Semi-log plot showing the effect of changing the value of D_{Al}. **(d)** Semi-log plot showing the effect of changing the value of k_c. **(e)** Plot showing the effect of changing the value of g^*.

The plots showing calculated N_{Al}^* as a function of $N_{\mathrm{O}}^{(s)}$ and D_{O} (Figure 25(a, b)) reveal an identical trend if either is increased or decreased by an equivalent factor relative to its base value. The predicted values of N_{Al}^* fall on S-shaped curves, approaching a non-zero, asymptotic limit for both high and low extremes of $N_{\mathrm{O}}^{(s)}$ or D_{O}. In the limit of low $N_{\mathrm{O}}^{(s)}$ or D_{O} values, inward oxygen diffusion becomes negligibly slow relative to outward Al diffusion, maximizing the degree to which Al is enriched at $z = \xi$ before

forming Al_2O_3 (see Figure 3). The solution does not converge to $N_{\mathrm{Al}}^{*} = 0$ in the limit of low $N_{\mathrm{O}}^{(\mathrm{s})}$ or D_{O} values because the timescale for Al enrichment is still restricted by growth of the competitive MO_β scale, i.e. the specific solution that $N_{\mathrm{Al}}^{*} \cong 0.19$ results from a balance between the base values of D_{Al} and k_c. Conversely, in the limits of high $N_{\mathrm{O}}^{(\mathrm{s})}$ or D_{O} values, outward Al diffusion becomes negligibly slow relative to inward oxygen diffusion. In such a situation, Al is essentially immobile and diffuses at a rate which is insufficient to allow for any significant enrichment at $z = \xi$ before the Al_2O_3 is formed (i.e. $\alpha = 1$). It is, therefore, required that $N_{\mathrm{Al}}^{*} = N_{\mathrm{AlO}_\nu}$ to obtain an oxide volume fraction of g^* and satisfy the modified Wagner-Maak criterion. In this case, N_{Al}^{*} may simply be calculated directly from Equation 4.1, which depends only on g^*, V_{M}, and V_{ox}. Inserting the base values for these three parameters into Equation 4.1, one obtains $N_{\mathrm{AlO}_\nu} \cong 0.26$, which is the asymptotic limit of the predicted value of N_{Al}^{*} at high values of $N_{\mathrm{O}}^{(\mathrm{s})}$ or D_{O}.

The plot showing calculated N_{Al}^{*} vs. D_{Al} (Figure 25(c)) also exhibits an S-shaped trend. In the limit of low D_{Al} values, outward Al diffusion is again negligibly slow relative to inward oxygen diffusion. This is another scenario in which there is no significant Al enrichment, and an asymptotic limit is obtained that is identical to that observed for high $N_{\mathrm{O}}^{(\mathrm{s})}$ or D_{O} values (again, determined by Equation 4.1 and depending only on the values of g^*, V_{M}, and V_{ox}). In the limit of high D_{Al} values, the value of N_{Al}^{*} calculated from the modified Wagner-Maak model asymptotically approaches 0. This is because as D_{Al} increases, Al diffusion becomes fast relative to both oxygen diffusion and the competitive MO_β scale growth rate, causing the degree of predicted Al enrichment to continuously increase as D_{Al} is increased.

The plot of calculated N_{Al}^{*} as a function of k_c (Figure 25(d)) shows another S-shaped trend where both asymptotic limits are non-zero. In the limit of low k_c values, the growth rate of the competitive scale becomes negligibly slow relative to the diffusion rates of Al and oxygen. As a result, $X \ll \xi$ (see Figure 3), i.e. competitive MO_β scale growth is negligible. In this case, the timescale for Al enrichment is restricted only by the rate of inward oxygen diffusion, and the specific solution that $N_{\mathrm{Al}}^{*} \cong 0.21$ results from a balance between the base values of $N_{\mathrm{O}}^{(\mathrm{s})}$, D_{O}, and D_{Al}. In the limit of high k_c values, the diffusion rates of Al and oxygen become negligibly slow relative to the competitive scale growth rate. As in the case of high $N_{\mathrm{O}}^{(\mathrm{s})}$, high D_{O}, or low D_{Al}, no significant enrichment of Al is able to occur, and direct conversion of the

initial Al content to Al_2O_3 must result in the volume fraction g^* (as defined by Equation 4.1) for passivation to occur.

The plot in Figure 25(e) shows that the N_{Al}^* predicted by the modified Wagner-Maak model can be made to range anywhere from 0 to 1 for values of the critical Al_2O_3 volume fraction, g^*, lying between 0 and 1. Given the manner in which g^* is physically described by Wagner, we believe that this is a more intuitive result than that suggested by the unmodified model. Due to the limitations of Equation 1.16, the unmodified Wagner-Maak model must converge to a predicted value of $N_{Al}^* \leq V_M/V_{ox}$ as $g^* \rightarrow 1$.

The influence of V_M and ν on the values of N_{Al}^* predicted by the modified Wagner-Maak model were also investigated, but are not shown in Figure 25. Because V_M would be expected to vary with $Al_xFe_yNi_{1-x-y}$ composition, it was allowed to increase from the base value of 6.7 cm^3/mol up to 7.2 cm^3/mol (the approximate molar volume of pure Fe at 427 °C), but the predicted value of N_{Al}^* was only found to vary by ~0.01 across this range. The parameter ν was investigated because, as discussed in detail by Meijering,[69] its effective value can change if the metal component forming the protective oxide also forms a mixed oxide with another alloy component, a condition which might arise in the $Al_xFe_yNi_{1-x-y}$ system. In AlNi alloys, the effective value of ν has been found to be ~2 due to $NiAl_2O_4$ formation.[58] However, changing ν from the base value of 1.5 to 2.0 was found to change the N_{Al}^* predicted by the modified Wagner-Maak model by <0.005. Thus, if the modified Wagner-Maak model can be applied to our $Al_xFe_yNi_{1-x-y}$ CSAFs, changes in the effective values of V_M and/or ν are unlikely to be significant factors in causing the comparatively large variations of N_{Al}^* across the composition space (see Figure 23), and will not be discussed further.

4.4.7. Assessing $Al_xFe_yNi_{1-x-y}$ CSAF oxidation with modified Wagner-Maak model

We have used the results shown in Figure 25 to consider possible physical insights into the complex dependence of the value of N_{Al}^* on both composition and humidity that we have observed using $Al_xFe_yNi_{1-x-y}$ CSAFs. This was done by assuming that the oxidation of the CSAFs at 427 °C is diffusion-controlled, and can be accurately described by the modified Wagner-Maak model given appropriate effective values of the kinetic parameters, as discussed in Chapter 4.4.5. Specifically, Figure 25 was used to assess whether changes in values of the various parameters might explain the total range

observed for N_{Al}^{*}, i.e. the difference between the maximum and minimum N_{Al}^{*} observed in the $Al_xFe_yNi_{1-x-y}$ system in either oxidizing environment. The highest value measured for N_{Al}^{*} in $Al_xFe_yNi_{1-x-y}$ was ~0.38, occurring at a composition of $Al_{0.38}Fe_{0.56}Ni_{0.06}$ in humid air, while the lowest measured value was ~0.15, occurring at $Al_{0.15}Fe_{0.74}Ni_{0.11}$ in dry air. Thus, the range of N_{Al}^{*} values was found to be 0.23. As illustrated in Figure 23, the minimum and maximum occur at a very similar Fe-to-Ni ratio in the two different environments, i.e. substituting ~10% H_2O by volume into dry air in a 427 °C oxidizing environment is apparently solely responsible for causing some change in the system that leads N_{Al}^{*} to increase by 0.23 in an $Al_xFe_yNi_{1-x-y}$ CSAF where N_{Fe} / (N_{Fe} + N_{Ni}) ≅ 0.90. If the modified Wagner-Maak model indeed applies to the system, then the addition of the small amount of humidity to the oxidizing environment must be resulting in a change in the effective values of one or more of the kinetic parameters which causes a change in the critical Al concentration of $\Delta N_{\mathrm{Al}}^{*} = 0.23$. Of the parameters analyzed in Figure 25, only changes in D_{Al} or g^{*} are predicted to be individually capable of causing a $\Delta N_{\mathrm{Al}}^{*} \geq 0.23$. This simple sensitivity analysis does not, of course, rigorously prove the importance of either parameter since the predicted N_{Al}^{*} depends on the values of all of the parameters which may be coupled to one another, and which might all change upon switching oxidizing environments. However, the analysis does reveal a vital aspect of the model: that the maximum possible value that can be predicted for N_{Al}^{*} is independent of the values of $N_{\mathrm{O}}^{(\mathrm{s})}$, D_{O}, D_{Al}, and k_c. As noted earlier, these maximum N_{Al}^{*} solutions occur when Al enrichment is negligible and they depend only on g^{*}, V_{M}, and V_{ox}, as defined in Equation 4.1. Thus, for the highest measured value of N_{Al}^{*} ($Al_{0.38}Fe_{0.56}Ni_{0.06}$ in humid air) to be predicted by the modified Wagner-Maak model requires that $g^{*} \geq 0.54$, given the base values for V_{M} and V_{ox} shown in Table 3.

Before further considering the potential importance of the various parameters when applying the modified Wagner-Maak criterion to our $Al_xFe_yNi_{1-x-y}$ oxidation results at 427 °C, two important points must be made regarding the base values used for D_{O} and k_c in our sensitivity analysis. First, Stott[65] showed that the diffusion coefficient of oxygen along the incoherent interface between Al_2O_3 and a bulk Ni lattice is orders of magnitude greater than that for diffusion through the lattice at temperatures between 800 and 1100 °C, and that this difference increases as temperature decreases. As a result, the effective value of D_{O} in the $Al_xFe_yNi_{1-x-y}$ CSAFs during oxidation at 427 °C is likely to be significantly higher at all compositions than the base value which was estimated by extrapolation of lattice diffusion data. Second,

the base value of k_c was simply chosen to maximize the sensitivity of the predicted value of N_{Al}^* to small changes in k_c given the values already chosen for the other parameters. However, it is predicted from Equation 1.1 that, for this value of k_c, the total advancement depth, X, of the competitive scale (see Figure 3) will be only ~0.5 nm after 4 h oxidation time in an alloy where $N_{\mathrm{Al}}^{(0)} < N_{\mathrm{Al}}^*$. While determining precise values for X at different internally oxidized locations on the CSAFs was not practical given the characterization tools available to us, the XPS depth profiles taken in this region (e.g. Figure 20(i)) suggest that $X > 0.5$ nm, particularly at high Fe-to-Ni ratios where it appears that X may be on the order of tens of nm. Since k_c is a parabolic rate constant, this suggests that its actual value is likely several orders of magnitude higher than the base value across much of the composition space. As illustrated in Figure 25, higher effective values of D_{O} and k_c both tend to drive the modified Wagner-Maak model towards the physically limiting condition where Al enrichment is negligible. When this is the case, the N_{Al}^* predicted by the modified Wagner-Maak model is locally independent of all of the variables shown in Figure 25 except for g^*. If the model indeed applies to our system, then the N_{Al}^* boundary measured in dry air (see Figure 23) would support the argument that oxidation of the $Al_xFe_yNi_{1-x-y}$ CSAFs at 427 °C occurs in a regime where Al enrichment is negligible. The reason for this is that we have previously shown[37] that the total amount of competitive oxide that is formed increases significantly as the Fe-to-Ni ratio increases on the side of this boundary where $N_{\mathrm{Al}}^{(0)} < N_{\mathrm{Al}}^*$ (region 4). This indicates that the parabolic rate constant k_c must increase by orders of magnitude as the Fe-to-Ni ratio increases. Figure 25(d) shows that such an increase in k_c should generally favor an increase in N_{Al}^* but, in fact, the opposite trend is observed, i.e. the measured N_{Al}^* is significantly lower in AlFe than in AlNi, despite the much higher rate of competitive oxide growth. This is consistent with a situation where no significant enrichment of Al is able to occur and, as a result, N_{Al}^* is essentially independent of k_c.

In terms of the modified Wagner-Maak criterion, it is highly likely that only system-dependent changes in the value of g^* could explain the wide range we have observed for N_{Al}^* in $Al_xFe_yNi_{1-x-y}$ CSAFs exposed to dry or humid air at 427 °C. It appears to be physically unlikely that there can be any significant diffusive enrichment of Al during oxidation under these conditions, making the N_{Al}^* predicted by the model independent of all variables other than g^*, V_{M}, and V_{ox}. However, V_{ox} should remain constant

and the dependence on V_{M} is weak, leaving g^* as the only variable in the modified Wagner-Maak model that might change to explain the large ΔN_{Al}^* observed upon varying the Fe-to-Ni ratio and/or the humidity of the oxidizing environment. Until recently, the value of g^* used in the Wagner or Wagner-Maak models has been widely assumed to be a constant, and in many cases has simply been taken as $g^* = 0.3$, a value determined experimentally by Rapp for oxidation of AgIn alloys at 550 °C.[70] Our results directly suggest that g^* may depend on both alloy composition and the oxidizing environment in $Al_xFe_yNi_{1-x-y}$ CSAFs at 427 °C, which could also be true in bulk alumina formers at higher temperatures. This is consistent with recent findings by Zhao et al., who studied the oxidation of bulk AlCrNi and AlNi samples at 1000 °C in dry air and 30% H_2O in air by volume.[15,58] They found that N_{Al}^* was higher in the humid environment and, by assessment using the unmodified Wagner-Maak criterion (described by Equations 1.17 and 1.18), concluded that only an increase in g^* due to the presence of the H_2O vapor could account for the ΔN_{Al}^* that they observed. They also showed that internal Al_2O_3 precipitates formed in the humid environment were coarser and more widely spaced than those formed in the dry environment, and suggested that the difference in precipitate geometries might lead to different values of g^*. It is easy to rationalize that various factors that might depend on the specific precipitate geometry (e.g. the ratio of the Al_2O_3/M interface area to precipitate volume) could play an important role in determining the g^* at which oxygen diffusion will be blocked "sufficiently" for lateral Al_2O_3 growth to dominate.

If system-dependent variability of g^* is indeed significant, the ability to use the modified Wagner-Maak criterion to more accurately predict N_{Al}^* for generic AlM systems would require a more advanced kinetic treatment of two major aspects of the model: 1) determining the value of g^* required for different systems based on the metal(s) represented by M and the geometry of the Al_2O_3 precipitates, and 2) determining the N_{AlO_ν} that actually results from a given $N_{\mathrm{Al}}^{(0)}$ when accounting for volume expansion effects. The first aspect was partially considered in another recent paper by Zhao et al., in which they show that, neglecting specific precipitate-geometry effects, an expression for g^* can be derived which depends only on V_{ox} and V_{M}.[71] However, their equation was derived in the limit that $N_{\mathrm{O}}^{(\mathrm{s})} D_{\mathrm{O}} \ll N_{\mathrm{Al}}^{(0)} D_{\mathrm{Al}}$, and so is not likely to apply in systems where this is not the case, such as $Al_xFe_yNi_{1-x-y}$ at 427 °C. The second aspect is equally important because, even if an exact value of g^* could be determined, it must

also be possible to predict the $N_{Al}^{(0)}$ required to obtain the N_{AlO_ν} corresponding to that g^*. The simplifying assumptions used to develop both the unmodified and modified Wagner-Maak models neglect any effects of volume expansion due to diffusive Al enrichment or oxide formation and, as a result, are likely to limit the accuracy with which this can be done, particularly for large values of g^*. However, keeping this limitation in mind, Equation 4.1 can be used to calculate composition-dependent values of g^* from the N_{Al}^* boundaries that we have measured, since N_{Al}^* in $Al_xFe_yNi_{1-x-y}$ at 427 °C should be essentially independent of all other variables in the modified Wagner-Maak criterion, if it applies. Figure 26 shows the values of g^* calculated in this way as a function of Fe-to-Ni ratio for $Al_xFe_yNi_{1-x-y}$ oxidation in both the dry and humid air at 427 °C. Even if the internal oxidation of $Al_xFe_yNi_{1-x-y}$ at 427 °C cannot be accurately described by the Wagner-Maak model as shown in Figure 3 (i.e. is not diffusion-controlled), the concept of g^* is still likely to apply given the abrupt and marked transition we have observed between internal and external oxidation on the CSAFs. If this is the case, determining g^* values from N_{Al}^* using Equation 4.1 may still be generally appropriate, provided Al is not significantly enriched by some non-diffusive mechanism prior to Al_2O_3 precipitation. Even assuming Al enrichment is indeed negligible, the precise values of g^* shown in Figure 26 are unlikely to be accurate since Equation 4.1 does not account for volume expansion effects or details of the CSAF microstructure; however, the general trends observed in the dependence of g^* on the Fe-to-Ni ratio and oxidizing environment should be correctly representative of the system.

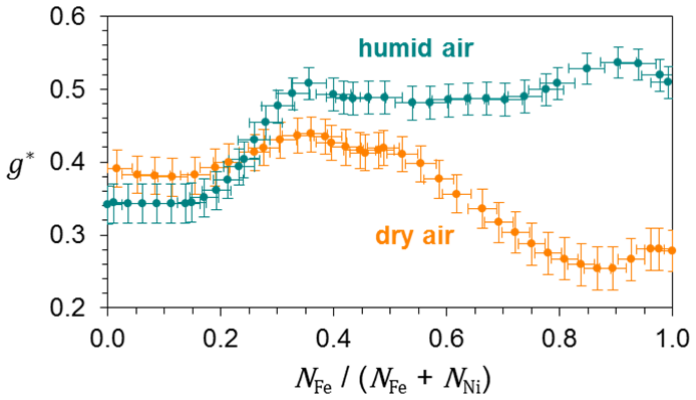

Figure 26. Plot showing the values of g^* corresponding to the measured N_{Al}^* boundaries for $Al_xFe_yNi_{1-x-y}$ oxidation in dry and humid air at 427 °C according to the modified Wagner-Maak criterion, assuming a limiting case where Al enrichment is negligible.

4.5. Conclusions

A high-throughput methodology was applied to the study of early oxidation of $Al_xFe_yNi_{1-x-y}$ CSAFs in humid air (~10% H_2O in air by volume) at 427 °C. A combination of characterization techniques was used to determine a continuous N_{Al}^* boundary through the ternary composition space, separating CSAF compositions that are passivated by formation of a surface or subsurface Al_2O_3 scale from those that are internally oxidized under these conditions. The work demonstrates the potential of CSAF-based, high-throughput methods to rapidly screen complex oxidation responses across continuous regions of alloy composition space. Such approaches could prove particularly valuable in thoroughly vetting the effect of different oxidizing environments on alloy oxidation, as demonstrated by our comparison of the N_{Al}^* boundary identified for $Al_xFe_yNi_{1-x-y}$ oxidation in humid air at 427 °C with that previously measured in dry air at the same temperature. While experimental constraints limited the direct subject of this work to early oxidation of ternary thin films, the ability to create thicker CSAFs containing more components could, in principle, allow oxidation of alumina formers at much higher temperatures to be studied across any continuous plane of higher-order composition space. Furthermore, the large amount of data generated by such high-throughput approaches could provide key fundamental insights into how to improve existing theoretical models in order to more accurately predict important properties like N_{Al}^*, which could aid in the development of improved alumina-forming alloys.

Chapter 5. Assessment of CSAF methodology for study of $Al_xFe_yNi_{1-x-y}$ oxidation

5.1. Introduction

As demonstrated in Chapters 3 and 4, the oxidation of alumina-forming alloys can exhibit a complex dependence on both multicomponent composition and the chemical environment. Because the value of N_{Al}^{*} is difficult to predict theoretically and impractical to identify empirically across multicomponent composition spaces using single-composition alloy samples, combinatorial screening approaches like the CSAF-based methods described in Chapters 3 and 4 should be ideal for studying alloy passivation by Al_2O_3 scale formation. Yet, despite the recent proliferation of combinatorial and high-throughput methods applied to a wide variety of other problems in materials science,[1–3] we are aware of only a handful of studies by other authors[19,28,72,73] that have attempted to apply such methods to the study of Al-alloy oxidation. Because the use of CSAFs to study multicomponent alloy oxidation is a relatively undeveloped field, the purpose of the work described in this Chapter was to critically assess certain aspects of the high-throughput methodology described in Chapters 3 and 4, in order to better understand the significance of the results. Specifically, we investigate two aspects of practical interest: 1) the widths in composition of the transitions between the different types of oxidation behavior upon crossing the boundaries between composition-space regions on the CSAFs, and 2) the extent to which CSAF oxidation behavior is representative of the behavior of bulk alloys exposed to identical oxidizing conditions. In the interest of simplicity, we explore these aspects by focusing specifically on the binary Al_xFe_{1-x} and Al_xNi_{1-x} areas of $Al_xFe_yNi_{1-x-y}$ CSAFs oxidized in dry air at 427 °C, a subset of the results reported in Chapter 3.

5.2. Results and discussion

5.2.1. Summary of relevant results from Chapter 3

A number of key results from Chapter 3 are directly relevant to the work discussed in this Chapter and will be referenced frequently. For convenience, these results have been reproduced in Figure 27. Figure 27(a) shows a schematic of an ideal $Al_xFe_yNi_{1-x-y}$ CSAF, which closely resembles those that were actually obtained with the RSM tool and used for our studies. The photograph in Figure 27(b) shows the

typical appearance of an $Al_xFe_yNi_{1-x-y}$ CSAF after it has been deposited, annealed at 427 °C for 2 h in UHV, and then briefly exposed to ambient air at room temperature. Figure 27(c) shows a photograph of one of the $Al_xFe_yNi_{1-x-y}$ CSAFs after exposure to dry air at 427 °C for $t_{ox} = 4$ h. The overlaid mesh indicating composition across the ternary region represents the best-fit CDM for the CSAF (see Chapter 3.2.2). The white circles mark the continuous boundaries (identified optically based on discoloration or with SEM) which subdivide the composition space into the four regions that we propose to exhibit the different types of oxidation behavior shown schematically around the photograph in Figure 27(c). The ternary composition diagram in Figure 27(d) shows the $C_O(t_{ox} = 4$ h) of the CSAF shown in Figure 27(c), and the diagram in Figure 27(e) shows the oxide phases detected via Raman spectroscopy. The type of oxidation behavior proposed for each region in Chapter 3 was determined based also on the XPS depth profiles from Figure 11, which are not reproduced in Figure 27.

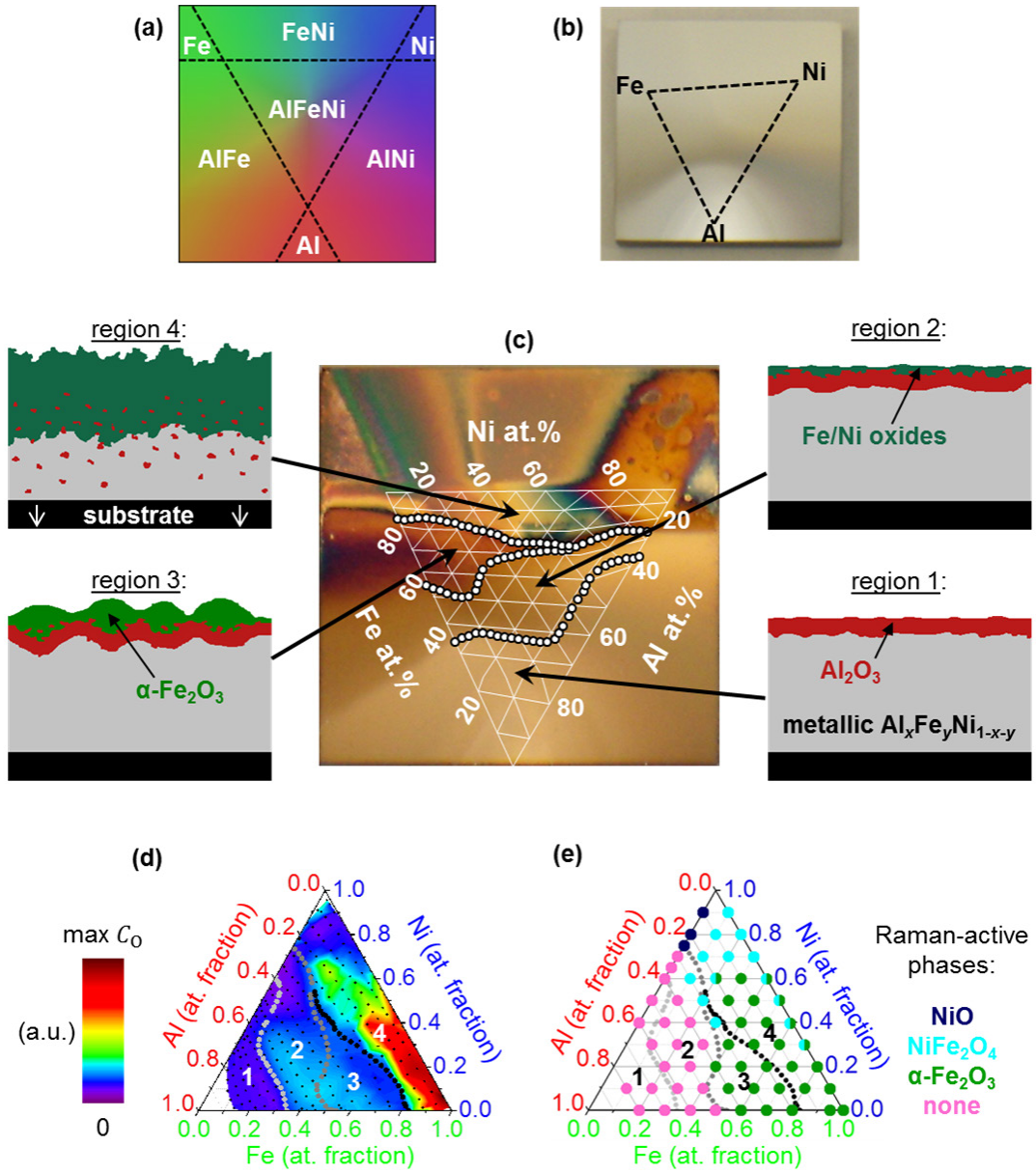

Figure 27. Summary of Chapter 3 study of $Al_xFe_yNi_{1-x-y}$ CSAF oxidation in dry air at 427 °C.[37] **(a)** Targeted gradient geometry for a full-range $Al_xFe_yNi_{1-x-y}$ CSAF. **(b)** Photograph of an $Al_xFe_yNi_{1-x-y}$ CSAF (annealed in UHV for 2 h at 427 °C) in ambient air. The approximate location of the ternary composition area is shown. **(c)** Photograph of an $Al_xFe_yNi_{1-x-y}$ CSAF which has been exposed to dry air at 427 °C for $t_{ox} = 4$ h. The color variations across the surface reflect differences in oxidation behavior. Four regions exhibiting unique oxidation phenomenology (represented schematically around the photograph) were identified in real space. The composition-space trajectories of the boundaries between these regions were determined based on the overlaid mapping of the $Al_xFe_yNi_{1-x-y}$ gradients. **(d)** The C_O measured with EDX across the CSAF shown in (c) represented on a ternary composition diagram. **(e)** Color-coded map of oxide phases detected with Raman spectroscopy across the CSAF shown in (c) represented on a ternary composition diagram.

5.2.2. Assessing the "sharpness" of transitions in oxidation behavior on CSAFs

The studies described in Chapters 3 and 4[37,38] identified four different composition-space regions on oxidized (427 °C in dry or humid air) $Al_xFe_yNi_{1-x-y}$ CSAFs that correlate with the results of EDX, Raman, and XPS analyses. The schematic depictions of oxide cross sections shown for the dry-air oxidized CSAF in Figure 27(c) illustrate the key, qualitative differences detected with these analysis methods. However, it is not completely clear based on the results in Chapters 3 and 4 how "sharp" the transitions between the regions are, i.e. what change in the CSAF composition is needed to induce a well-defined transition from one behavior to the next. The width of the oxidation transitions on CSAFs dictates the precision with which important boundaries such as N_{Al}^{*} can be identified.

Of the characterization analyses performed on the oxidized $Al_xFe_yNi_{1-x-y}$ CSAFs, EDX measurements allowed the highest density sampling of different locations/compositions. As discussed in Chapter 3.2.4, because the depth sensitivity of EDX greatly exceeds the thickness of the CSAF layer, we can use these measurements to estimate values of C_{O}, the total amount of oxygen incorporated within the entire CSAF cross section at any laterally resolved location during oxidation. In the studies described in Chapters 3 and 4, we identified the composition regions that are passivated on the CSAFs by analyzing oxygen-uptake kinetics as determined from measurements of C_{O} made across composition space at different total exposure times to the oxidizing environment, t_{ox}.[37,38] For example, Figure 27(d) shows $C_{\mathrm{O}}(t_{ox} = 4\ \mathrm{h})$ as measured from the CSAF pictured in Figure 27(c). However, quantitative analysis of data as plotted in Figure 27(d) (i.e. using color-scale contours in a ternary composition diagram) is difficult and may be misleading.

By focusing only on the measurements of C_{O} taken in the binary Al_xFe_{1-x} and Al_xNi_{1-x} regions of $Al_xFe_yNi_{1-x-y}$ CSAFs, the data can instead be represented on standard, two-dimensional plots. Figure 28 shows C_{O} measured across the Al_xFe_{1-x} (left column) and Al_xNi_{1-x} (right column) binary regions of $Al_xFe_yNi_{1-x-y}$ CSAFs oxidized in dry air at 427 °C. The plots in the top row show total C_{O} measured at $t_{ox} = 0$, 1, and 4 h, while the plots in the middle and bottom rows show the change in C_{O}, ΔC_{O}, in the two intervening time periods. The full scale for C_{O} or ΔC_{O} on each plot is defined relative to the arbitrary maximum value in the upper-left plot. The data shown in Figure 28 were collected from two different CSAFs; points measured from one sample are plotted as circles, while those measured from the other are

plotted as diamonds. The two data sets overlap very closely, demonstrating remarkable reproducibility between the two different CSAFs. The vertical dashed lines in each plot mark the composition boundaries between regions 1-4 (see Figure 27(c)) corresponding to real-space features observed in optical or SEM images of the CSAFs. It is evident from Figure 28 that these boundaries correlate well with shifts in how C_{O} and/or ΔC_{O} change as a function of Al_xFe_{1-x} or Al_xNi_{1-x} composition. Of particular note is that $\Delta C_{\mathrm{O}} \cong 0$ from $t_{ox} = 1$ to 4 h (bottom row) in regions 1, 2, and 3, indicating that these compositions were passivated against further oxidation after some $t_{ox} \leq 1$ h. We attribute the small ΔC_{O} from $t_{ox} = 0$ to 1 h (middle row) in regions 2 and 3 to initial growth of trace Fe and/or Ni oxides at the alloy surface before passivating Al_2O_3 was established in the subsurface. Region 4 compositions exhibit the highest values of $C_{\mathrm{O}}(t_{ox} = 4\text{ h})$ (top row) and have $\Delta C_{\mathrm{O}} > 0$ from $t_{ox} = 1$ to 4 h (bottom row), indicating that passivation did not occur. Overall, the EDX measurements show that readily definable transitions in the oxygen-uptake kinetics occur abruptly in composition space near the boundaries identified between the numbered regions, apparently over a range of just a few at.% in alloy composition.

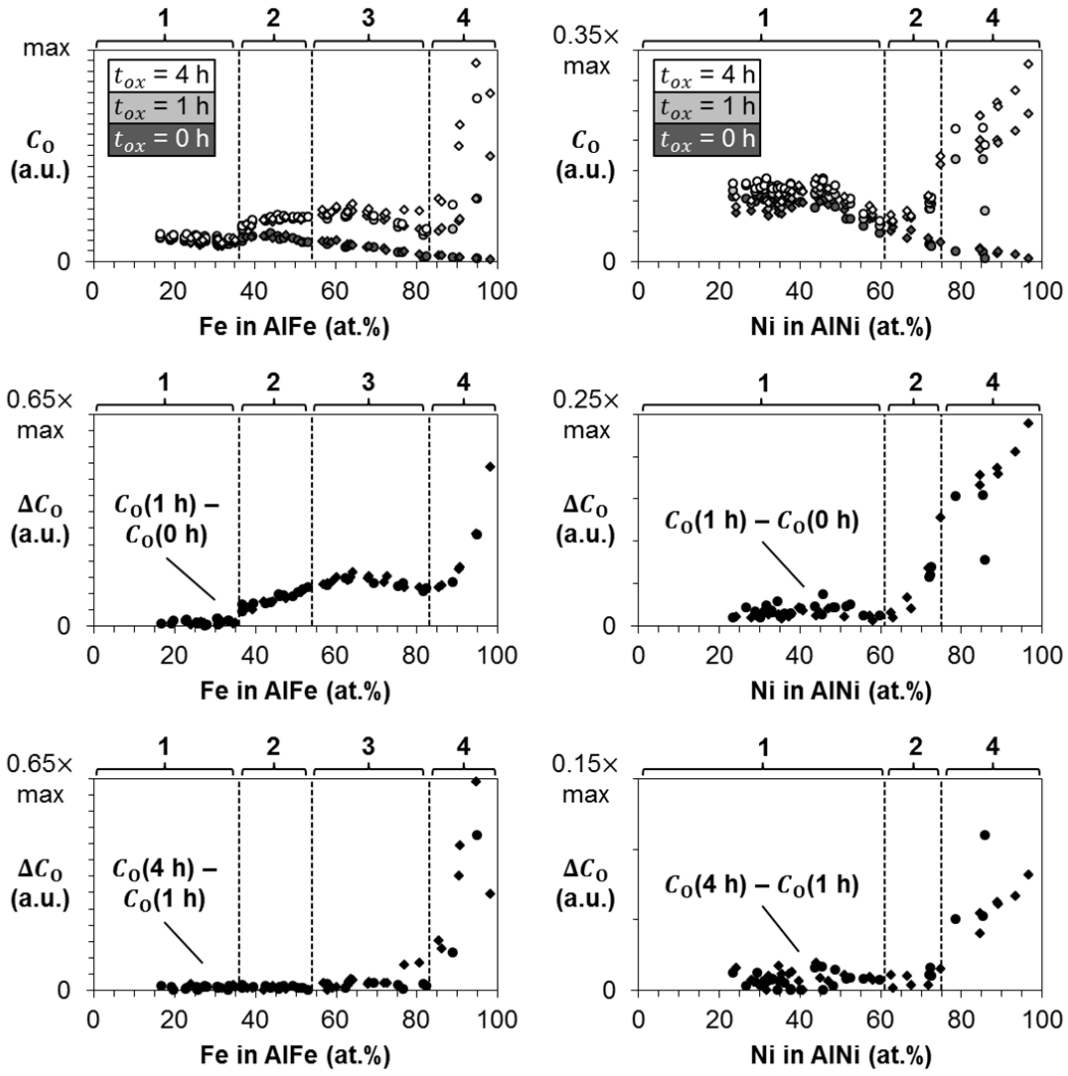

Figure 28. Arbitrary C_O (total oxygen content – top row) measured across two $Al_xFe_yNi_{1-x-y}$ CSAFs after t_{ox} = 0, 1, and 4 h in dry air at 427 °C and the ΔC_O in the two intervening time periods (bottom two rows). The data points from one CSAF are plotted as circles, while those from the other are plotted as diamonds. The left column contains the data for binary Al_xFe_{1-x} compositions, while the right column contains the data for binary Al_xNi_{1-x} compositions. The maximum C_O or ΔC_O for each plot is scaled relative to the arbitrary maximum on the plot in the upper left; each tick mark on the vertical axes represent 5% of this maximum value. The vertical dashed lines represent the composition-space boundaries between the four regions which exhibit phenomenologically different types of oxidation behavior. The region numbers are shown across the top of each plot.

XPS depth profiling allows spatially resolved analysis of the cross-sectional distribution of metals and oxides in a CSAF and, thus, can be used to distinguish more subtle differences in oxidation behavior than is possible based solely on oxygen-uptake kinetics. However, due to the large amount of time required to measure the depth profiles, the maximum number of locations that can be practically analyzed

is much smaller than with EDX. Therefore, we have used XPS depth profiling to focus specifically on three of our proposed transitions in oxidation behavior in the binary regions of $Al_xFe_yNi_{1-x-y}$ CSAFs oxidized for $t_{ox} = 4$ h in dry air at 427 °C (see Figure 27(c)): region 1 to region 2 in Al_xFe_{1-x}, region 3 to region 4 in Al_xFe_{1-x}, and region 2 to region 4 in Al_xNi_{1-x}. In each case, a series of 5 depth profiles was measured along a line crossing the continuous boundary (identified visually or with SEM on an oxidized CSAF surface) proposed to correlate with a transition in oxidation behavior.

Figure 29 shows the results of the XPS depth profiling performed to investigate the transition from region 1 to region 2 in Al_xFe_{1-x} composition space. The SEM image (top) shows the portion of the oxidized CSAF surface where the depth profiles were later performed; the approximate areas sampled by the profiles are indicated by the circles labeled a-e. The continuous boundary between regions 1 and 2 is visible as a change in SEM contrast; region 1 appears lighter, while region 2 appears darker. Therefore, areas a and b fall entirely within region 2, areas d and e fall entirely within region 1, and area c contains part of both regions. The profiles obtained across areas a-e are presented in Figure 29(a-e), respectively; the labels indicate the composition of the CSAF at the center of each area as determined by EDX prior to the high-temperature exposure (i.e. at $t_{ox} = 0$ h). The profile plots show the relative composition of elements in metallic or oxidized chemical states (determined using XPS) as a function of etching time with a rastered Ar^+ beam, i.e. depth into the sample. Since the CSAFs are ~100 nm thick,[37,38] a length scale for depth into the sample can be approximated on the horizontal axes based on the time at which the Mo substrate appears, as shown in Figure 29(e). The profiles from region 1 (Figure 29(d, e)) show that a thin, continuous layer of oxidized Al was formed at the CSAF surface, while the rest of the cross section remained metallic and uniform in composition. The profiles from region 2 (Figure 29(a, b)) are very similar, but show that the continuous layer of oxidized Al is present in the subsurface beneath trace Fe oxide at the surface (at greater depths, a small fraction of oxidized Al is also detected, but the Fe remains in a metallic state). Each of the profiles contained entirely within region 1 or 2 are consistent with the respective behavior which we have previously proposed (see Figure 27(c)).[37] The profiles directly indicate that a complete transition from region 1 to region 2 occurs over a composition window of $Al_{0.64}Fe_{0.36}$ to $Al_{0.61}Fe_{0.39}$. However, if the change in SEM contrast is indeed indicative of this

phenomenological change in oxidation behavior, then the complete transition actually occurs within area c, over a composition range of ~1 at.%.

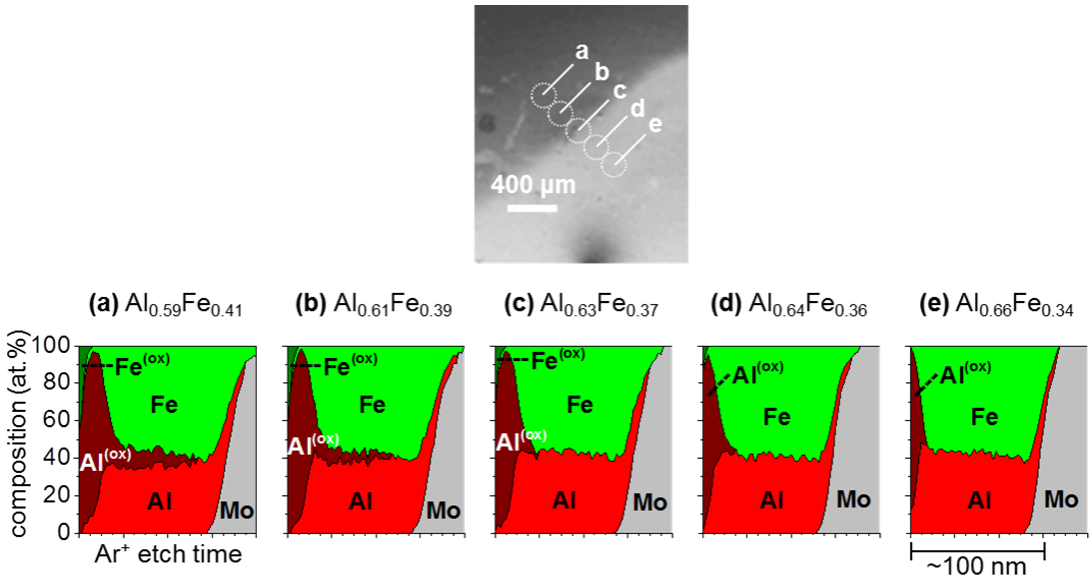

Figure 29. Line of XPS depth profiles performed on an $Al_xFe_yNi_{1-x-y}$ CSAF to investigate the transition between regions 1 and 2 for Al_xFe_{1-x} after t_{ox} = 4 h in dry air at 427 °C. The SEM image (top) shows the five approximate areas, a-e, across which the depth profiles were later performed. The boundary between regions 1 and 2 is visible based on the SEM contrast and passes through area c (region 1 appears lighter and region 2 appears darker). **(a)-(e)** The depth profile plots measured across the correspondingly labeled areas, a-e. The label above each plot is the CSAF composition measured with EDX at the center of the area at t_{ox} = 0 h. The plots show the relative composition of each detected element, M, in a metallic, "M", or oxidized, "$M^{(ox)}$", chemical state as a function of total Ar^+ etch time. An approximate length scale is shown below the plot in (e).

The results of the XPS depth profiling performed to investigate the transition from region 3 to region 4 in Al_xFe_{1-x} composition space are shown in Figure 30. The low-magnification SEM image (top) shows the approximate areas, labeled a-e, at which the 5 profiles were later obtained on the oxidized (t_{ox} = 4 h) CSAF surface. In this case, the transition between regions is not visible by SEM contrast, but is clearly evident based on optical appearance (see Figure 27(c)). Areas d and e fall entirely within region 3, while areas a and b fall entirely within region 4. The optically identified boundary between regions 3 and 4 passes through area c. The profiles obtained across areas a-e are shown in Figure 30(a-e), respectively. Each profile is also accompanied by a high-magnification SEM image taken at the center of the measurement area prior to the depth profiling. The labels above these SEM images indicate the

CSAF composition at the center of each measurement area determined using EDX at $t_{ox} = 0$ h. The appearance of the profiles from region 3 (Figure 30(d, e)) is consistent with the proposed passivation behavior shown in Figure 27(c).[37] Given sufficient variations in the thickness of the surface α-Fe_2O_3, uniform Ar^+ etching would not simultaneously expose the continuous Al_2O_3 layer in the subsurface. Thus, XPS depth profiling of such a cross section would be expected to reveal subsurface enrichment of Al oxide, but not to 100% for any given etch time, consistent with the profiles in Figure 30(d, e). In contrast, the profiles from region 4 (Figure 30(a, b)) show extensive formation of Fe oxide and no sign of oxidized Al enrichment at any depth, indicating that the CSAF is not passivated. The CSAF surface in region 4 exhibits significant roughening as a result of the oxidation, as evident from the high-magnification SEM images in Figure 30(a, b). As a result, the transition from the CSAF to the Mo substrate appears more gradual in these profiles (thinner areas were etched away to reveal the underlying substrate much earlier than thicker areas). The profile in Figure 30(c) is consistent with an average of the profiles from the two different regions, arising from simultaneous sampling of the two different oxide cross sections present within area c. The set of profiles in Figure 30 suggest that a well-defined transition from region 3 to region 4 behavior occurs abruptly in Al_xFe_{1-x} composition space near $Al_{0.19}Fe_{0.81}$ as a result of a change in alloy composition of a few at.%, at most.

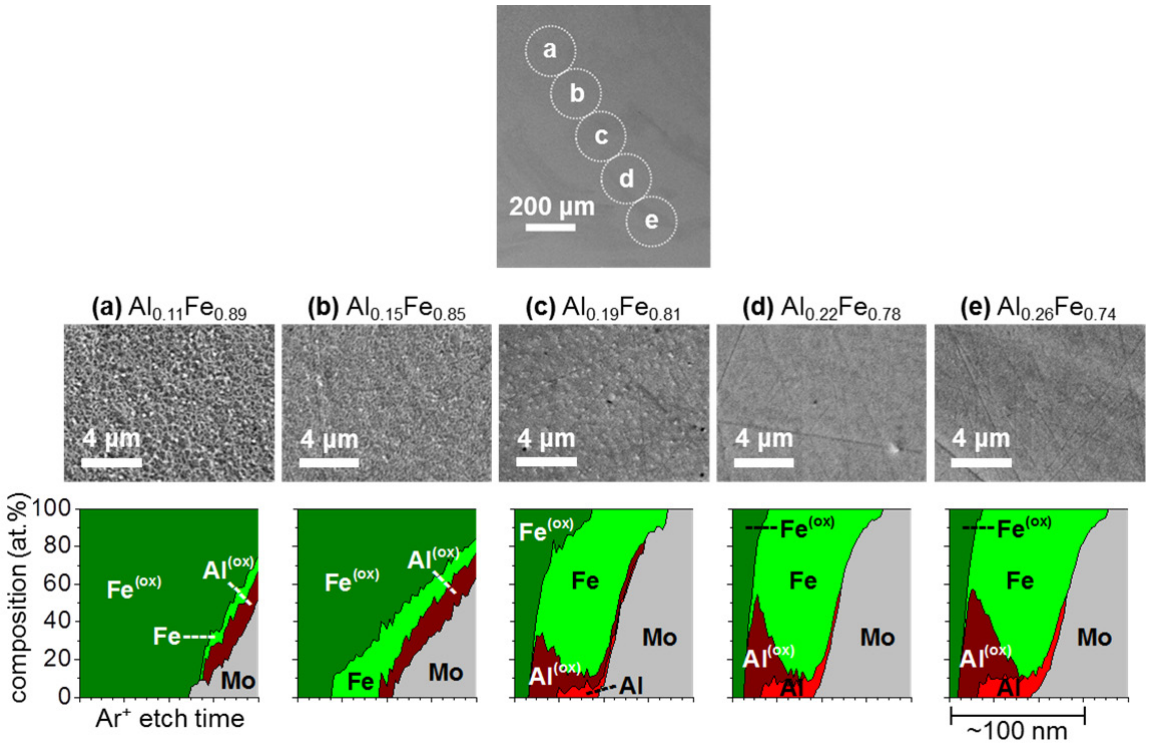

Figure 30. Line of XPS depth profiles performed on an $Al_xFe_yNi_{1-x-y}$ CSAF to investigate the transition between regions 3 and 4 for Al_xFe_{1-x} after t_{ox} = 4 h in dry air at 427 °C. The topmost SEM image shows the five approximate areas, a-e, across which the depth profiles were later performed. The boundary between regions 3 and 4 is not visible based on the SEM contrast, but passes through area c. **(a)-(e)** The depth profile plots measured across the correspondingly labeled areas, a-e, and SEM images taken at the center of the areas prior to obtaining the depth profiles. The label above each SEM image is the CSAF composition measured with EDX at the center of the area at t_{ox} = 0 h. The plots show the relative composition of each detected element, M, in a metallic, "M", or oxidized, "$M^{(ox)}$", chemical state as a function of total Ar^+ etch time. An approximate length scale is shown below the plot in (e).

Figure 31 shows the results of the XPS depth profiling performed to investigate the transition from region 2 to region 4 in Al_xNi_{1-x} composition space (region 3 behavior specifically involves α-Fe_2O_3 growth and, therefore, does not occur in binary Al_xNi_{1-x}). The low-magnification SEM image (top) shows the areas, labeled a-e, across which the 5 profiles were later performed. The boundary between regions 2 and 4 is visually obvious in optical images of oxidized CSAFs (see Figure 27(c)), and can also be discerned by SEM contrast; region 2 appears darker, while region 4 appears lighter. Thus, areas a and b are entirely within region 4, areas d and e are entirely within region 2, and area c covers part of both regions. Plots of the profiles obtained at areas a-e are shown in Figure 31(a-e), respectively. The EDX-measured composition at t_{ox} = 0 h and a high-magnification SEM image from the center of each area

(taken prior to the depth profiling) are also shown. It is evident from Figure 31 that an abrupt transition in oxidation phenomenology occurs around the composition $Al_{0.29}Ni_{0.71}$. The profiles from region 2 (Figure 31(d, e)) exhibit clear evidence of continuous oxidized Al in the subsurface beneath trace Ni oxide, consistent with the behavior we have previously proposed for this region (see Figure 27(c)).[37] The profiles from region 4 (Figure 31(a, b)) appear to show partial subsurface enrichment of oxidized Al, but based on previous EDX measurements of oxygen-uptake kinetics at similar locations on other $Al_xFe_yNi_{1-x-y}$ CSAFs, this enrichment is not believed to correspond to formation of a passivating Al_2O_3 scale in the subsurface.[37,38] The high-magnification SEM images appear to show that the surface has become roughened and/or pitted in region 4 as a result of the oxidation, likely explaining the small amount of Mo detected at short etch times in the profiles in Figure 31(a, b). It appears from Figure 31 that a complete transition from region 2 to region 4 in Al_xNi_{1-x} composition space occurs over ~1 at.%, and that the appearance of the profile in Figure 31(c) is again an average of the profiles from the two different regions.

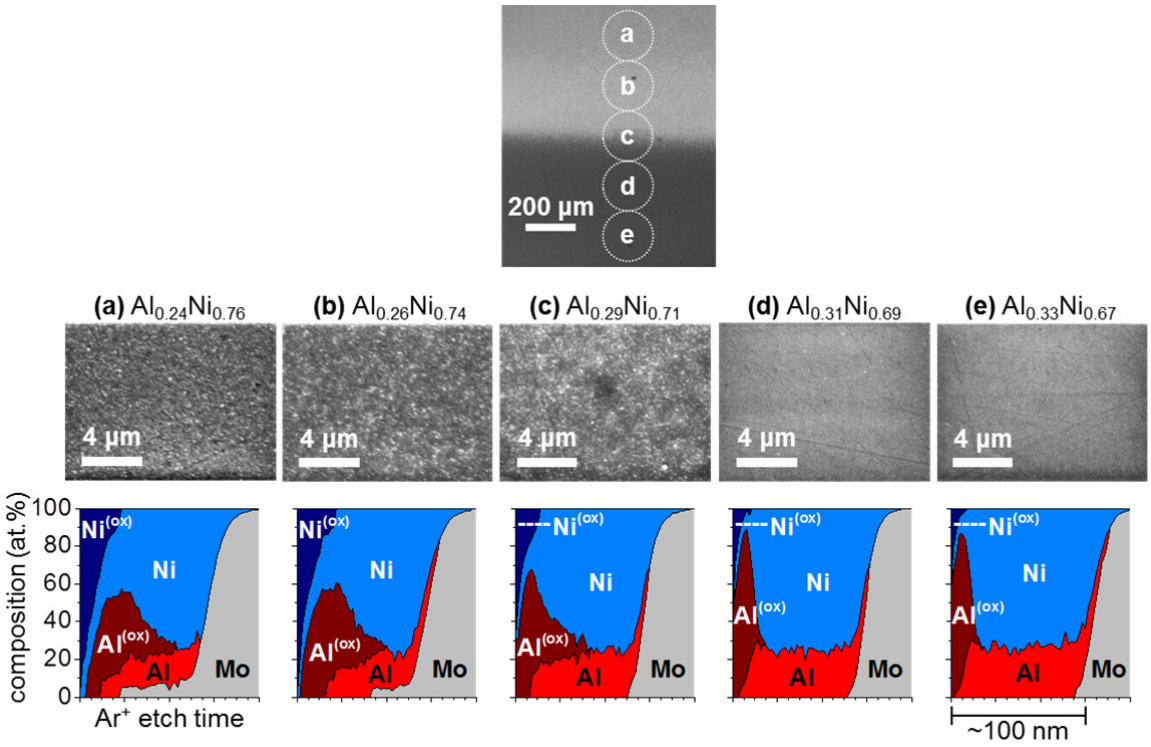

Figure 31. Line of XPS depth profiles performed on an $Al_xFe_yNi_{1-x-y}$ CSAF to investigate the transition between regions 2 and 4 for Al_xNi_{1-x} after t_{ox} = 4 h in dry air at 427 °C. The topmost SEM image shows the five approximate areas, a-e, across which the depth profiles were later performed. The boundary between regions 2 and 4 is visible based on the SEM contrast and passes through area c (region 2 appears darker and region 4 appears lighter). **(a)-(e)** The depth profile plots measured across the correspondingly labeled areas, a-e, and SEM images taken at the center of the areas prior to obtaining the depth profiles. The label above each SEM image is the CSAF composition measured with EDX at the center of the area at t_{ox} = 0 h. The plots show the relative composition of each detected element, M, in a metallic, "M", or oxidized, "$M^{(ox)}$", chemical state as a function of total Ar^+ etch time. An approximate length scale is shown below the plot in (e).

The results presented in Figures 28, 29, 30, and 31 indicate that phenomenologically definable transitions in the oxidation behavior of the CSAFs occur abruptly in Al_xFe_{1-x} and Al_xNi_{1-x} composition space upon crossing the continuous boundaries that were identified optically or with SEM. While not explicitly investigated in the work described in this Chapter, we expect that the same is true for the continuations of these boundaries through the $Al_xFe_yNi_{1-x-y}$ region of the CSAFs (see Figure 22), as reported in the results discussed in Chapters 3 and 4.[37,38] For the specific boundaries that we have investigated, it appears that well-defined transitions in oxidation behavior occur completely over a composition range of ~1-2 at.%. However, it should be noted that the absolute accuracy with which we are able to determine CSAF composition (e.g. along the identified boundaries or at the depth profile

locations) is limited by the accuracy of our EDX-based composition measurements (discussed in Chapter 3.3.1), and is likely no better than ±2 at.%. Thus, the actual $Al_xFe_yNi_{1-x-y}$ CSAF compositions at which the identified transitions in oxidation behavior occur may systematically differ from those reported within this degree of uncertainty.

5.2.3. Comparing oxidation behavior of CSAFs with that of bulk alloys

The other aspect of our CSAF-based oxidation studies that we consider in this Chapter is comparison of CSAF oxidation to that of bulk (single-composition) alloys exposed to identical oxidizing environments. It is important to emphasize that the subject of our studies is a very specific and unique system, namely, ~100 nm-thick $Al_xFe_yNi_{1-x-y}$ films that were UHV annealed at 427 °C, exposed briefly to ambient air at room temperature during transfer, and then oxidized in dry or humid air at 427 °C for up to 4 h. There are two principal reasons why $Al_xFe_yNi_{1-x-y}$ bulk alloys might exhibit oxidation behavior different from that of ~100 nm-thick CSAFs with equivalent composition. First, the grain structure of the CSAFs is likely to be significantly different from that of bulk alloys, and this difference might influence oxidation processes (e.g. if oxygen and/or metal transport along grain boundaries plays an important role). Second, if oxide formation proceeds across enough of a CSAF's cross section, preferential depletion of one or more of the component metals from the portion of the film that is not yet oxidized could cause a non-negligible change in its composition, which might alter subsequent oxidation processes.

Six bulk alloys (four different binary Al_xFe_{1-x} compositions and two different binary Al_xNi_{1-x} compositions) were prepared for comparison with $Al_xFe_yNi_{1-x-y}$ CSAFs. The targeted compositions and their corresponding behavior regions were $Al_{0.70}Fe_{0.30}$ (region 1), $Al_{0.55}Fe_{0.45}$ (region 2), $Al_{0.30}Fe_{0.70}$ (region 3), $Al_{0.10}Fe_{0.90}$ (region 4), $Al_{0.35}Ni_{0.65}$ (region 2), and $Al_{0.20}Ni_{0.80}$ (region 4) (see Figure 27(c)).[37] Each bulk alloy was cast as an ingot, from which a 7×7×2.5 mm^3 token was cut for use in the oxidation studies. According to the Al_xFe_{1-x} and Al_xNi_{1-x} phase diagrams,[74,75] $Al_{0.30}Fe_{0.70}$, and $Al_{0.10}Fe_{0.90}$ should form a single phase at all temperatures, while various two-phase equilibria are favored for $Al_{0.70}Fe_{0.30}$, $Al_{0.55}Fe_{0.45}$, $Al_{0.35}Ni_{0.65}$, and $Al_{0.20}Ni_{0.80}$, depending on temperature. However, phase formation in cast alloys can be influenced by the cooling profile, which was not measured, making it difficult to predict which phases should be expected. One 7×7 mm^2 face of each token was mechanically polished to a mirror finish. The polished faces were cleaned under UHV by Ar^+ sputtering, after which the tokens were annealed at 427

°C for 2 h. Since the alloys were cast at a much higher temperature, it is unlikely that their grain structure was significantly affected by the annealing at 427 °C. The samples were briefly exposed to ambient air upon removal from the UHV chamber, after which initial characterization ($t_{ox} = 0$ h) of the polished/sputtered faces was performed using SEM imaging and EDX. The tokens were then exposed to dry air at 427 °C for $t_{ox} = 4$ h and the characterization measurements were repeated.

Low-magnification SEM images of the six bulk alloys at $t_{ox} = 0$ h are shown in Figure 32(a-f). The images were captured using back-scattered electron (BSE) detection. Two-phase separation is clearly visible from the BSE contrast for $Al_{0.55}Fe_{0.45}$ and $Al_{0.35}Ni_{0.65}$ (Figure 32(b, e), respectively), and can also be discerned (with sufficient image resolution) for $Al_{0.70}Fe_{0.30}$ (Figure 32(a)). There also appear to be contrast variations across the image of $Al_{0.20}Ni_{0.80}$ (Figure 32(f)), but the edges are not sharply defined. $Al_{0.30}Fe_{0.70}$ and $Al_{0.10}Fe_{0.90}$ (Figure 32(c, d), respectively) appear flat and featureless on the imaged length scale.

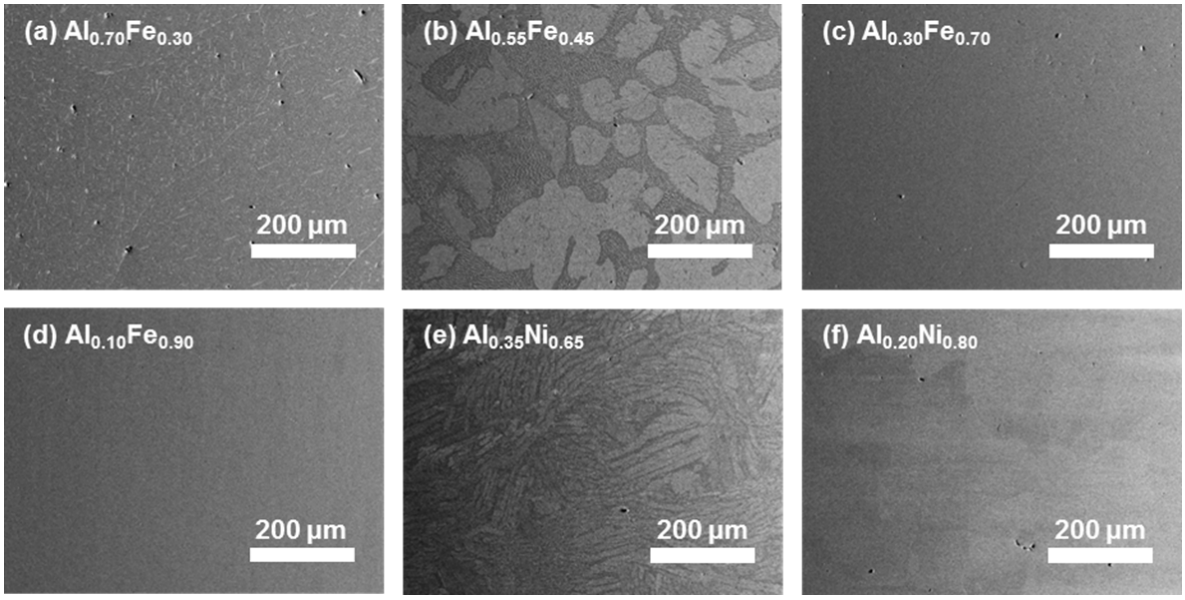

Figure 32. Low-magnification BSE-SEM images of the as-prepared (polished, sputtered, and annealed) surfaces of bulk Al_xFe_{1-x} and Al_xNi_{1-x} samples prior to oxidation in dry air at 427 °C ($t_{ox} = 0$ h).

Higher-magnification BSE-SEM images of each of the bulk alloys are shown in Figure 33 at both $t_{ox} = 0$ h (left column) and $t_{ox} = 4$ h (right column). The images in Figure 33(a-f) are of the same samples as those in in Figure 32(a-f), respectively. The compositions reported in Figure 33 were measured by performing EDX on the alloys at $t_{ox} = 0$ h. The "average" compositions were determined from area scans taken across ~700×500 μm^2 areas centered at the imaged locations. The average compositions are consistent with the targeted compositions of the samples to ±2 at.%, except for the alloy in Figure 33(e), which was nominally $Al_{0.35}Ni_{0.65}$, but was measured to be $Al_{0.31}Ni_{0.69}$. It can be seen from the BSE-SEM contrast that four of the alloys (Figure 33(a, b, e, f)) partitioned into two distinct phases. EDX point scans (~0.5×0.5 μm^2 spot) were used to measure individually the compositions of the "light" and "dark" phases visible in each case; the results are shown below the average compositions. The phase compositions were found to be measurably different in all four of the two-phase alloys, with the Al-rich phases appearing darker. The images of the other two alloys (Figure 33(c, d)) do not appear to show any evidence of phase separation, revealing only shallow scratches that remain after polishing. Images captured with BSE-SEM at identical locations on the alloys after $t_{ox} = 0$ h or $t_{ox} = 4$ h were indistinguishable from one another, with the exception of $Al_{0.10}Fe_{0.90}$, which became noticeably roughened as a result of oxidation. Thus, to provide an additional example of the characteristic appearance of each surface, the $t_{ox} = 4$ h images shown in Figure 33 are from different locations on their respective alloys than the $t_{ox} = 0$ h images. The fact that BSE-SEM imaging reveals no change in the two-phase alloys as a result of the oxidation indicates that the grain structure (presumably formed when the alloys were cast) was not significantly affected by the oxidation. This is unsurprising, given that the characteristic dimensions of the phase domains are large compared to the thickness of the various oxide layers formed in the ~100 nm-thick $Al_xFe_yNi_{1-x-y}$ CSAFs exposed to dry air at 427 °C (see Figure 27(c)).[37] However, it further suggests that the oxidation events under these conditions are likely to occur essentially independently on each phase, i.e. that grains with different phases are unlikely to interact significantly while oxidizing and, therefore, may behave differently due to their differing composition.

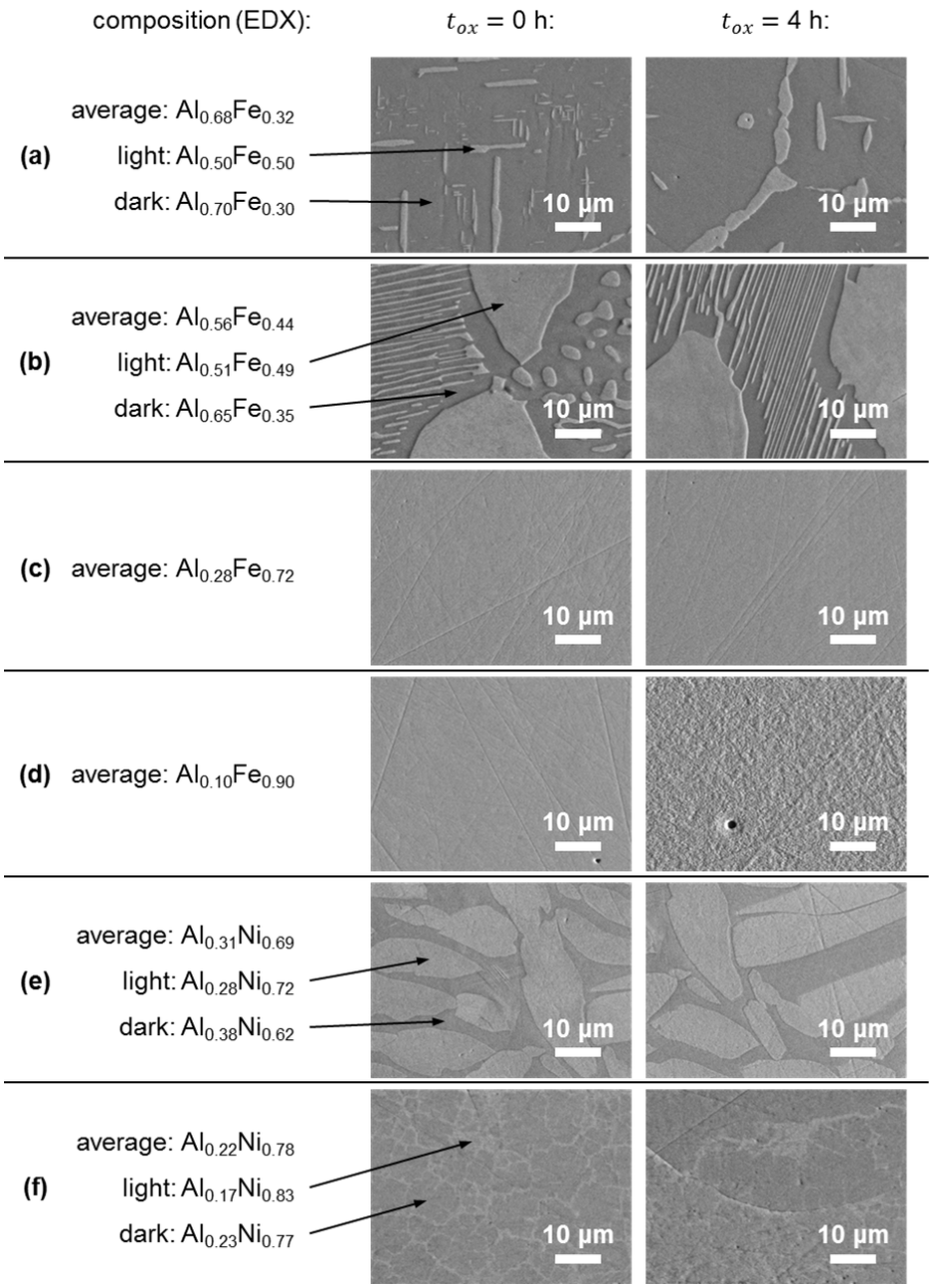

Figure 33. High-magnification BSE-SEM images of the bulk Al_xFe_{1-x} and Al_xNi_{1-x} samples taken after t_{ox} = 0 h (left column) and t_{ox} = 4 h (right column) in dry air at 427 °C. The labeled compositions were measured with EDX at t_{ox} = 0 h. The average compositions determined in this way are similar to the nominal compositions, which were **(a)** $Al_{0.70}Fe_{0.30}$, **(b)** $Al_{0.55}Fe_{0.45}$, **(c)** $Al_{0.30}Fe_{0.70}$, **(d)** $Al_{0.10}Fe_{0.90}$, **(e)** $Al_{0.35}Ni_{0.65}$, and **(f)** $Al_{0.20}Ni_{0.80}$. Each pair of images shown in (a)-(f) were taken at different locations on their respective sample. Except for (d), images taken at the same location on any of the samples after t_{ox} = 0 or 4 h were indistinguishable.

To investigate the differences between the grain structures of CSAFs and the bulk alloys, an $Al_xFe_yNi_{1-x-y}$ CSAF prepared at Carnegie Mellon University was sent to the National Institute of Metrology,

Quality and Technology of Brazil (Inmetro) for additional characterization using transmission electron microscopy (TEM). The CSAF underwent the same preparation, UHV-annealing, handling, and initial-characterization steps as those used in the oxidation studies, but was not exposed to dry air at 427 °C, i.e. $t_{ox} = 0$ h. The sample was shipped in a sealed container filled with Ar to minimize ambient air exposure while in transit, and removed from this container in a glove bag under N_2 upon arrival at Inmetro. Cross sections (~5×10 μm^2) of the CSAF/substrate were then cut from six different locations using a focused ion beam (FIB) and analyzed by TEM. Figure 34 provides a summary of important results collected from one of these locations, at which the CSAF composition was measured to be $Al_{0.58}Fe_{0.42}$ during the initial characterization at Carnegie Mellon University. Figure 34(a) shows a cross-sectional view of the CSAF/substrate layering in an image collected by scanning transmission electron microscopy (STEM) with annular dark-field detection (the Mo is the substrate, and the Pt is a protective layer deposited as part of the FIB cutting procedure). Figure 34(b) is a TEM bright-field image, providing a higher-magnification view of the CSAF layer. Figure 34(c) shows the diffraction pattern corresponding to the region imaged in Figure 34(b). The CSAF is polycrystalline, as clearly evidenced by the diffraction rings. Finally, Figure 34(d) is a TEM dark-field image of the same region shown in Figure 34(b), produced by selectively filtering for the (011) Bragg diffraction feature circled in Figure 34(c). The image in Figure 34(d) reveals that the CSAF has a columnar grain structure.

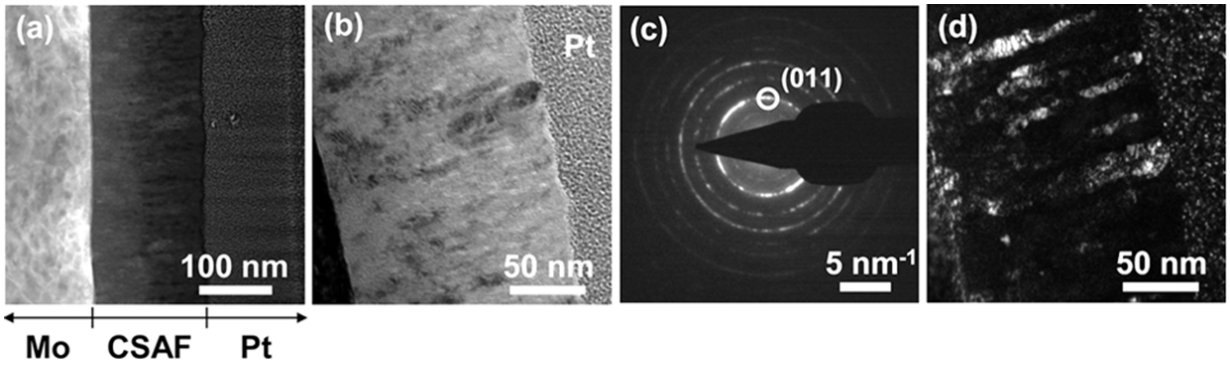

Figure 34. Summary of FIB-TEM analyses performed on an $Al_xFe_yNi_{1-x-y}$ CSAF ($t_{ox} = 0$ h) at a location where the composition is ~$Al_{0.58}Fe_{0.42}$. **(a)** STEM annular dark-field image showing the layering of the CSAF on the Mo substrate. The Pt layer was deposited on the CSAF for protection prior to the FIB cross sectioning. **(b)** TEM bright-field image showing a magnified view of the CSAF layer. **(c)** The diffraction pattern corresponding to the region imaged in (b). The pattern is comprised of rings, indicating that the CSAF is polycrystalline. **(d)** TEM dark-field image of the same view field shown in (b), filtered for the (011) Bragg diffraction feature circled in (c). The image shows that the CSAF formed columnar grains.

EDX and high-resolution transmission electron microscopy (HRTEM) were also used to analyze the sample (not shown in Figure 34). EDX measurements averaged across large areas of the CSAF cross section were consistent with the expected composition of $Al_{0.58}Fe_{0.42}$. Based on the STEM/TEM imaging (e.g. Figure 34(a, b, d)), the thickness of the CSAF at this location was determined to be 152 ±3 nm. STEM imaging coupled with EDX elemental mapping revealed that any intermixing of the Mo substrate with the CSAF was limited to an interface region of ~4 nm in thickness. TEM dark-field imaging (e.g. Figure 34(d)) showed that the CSAF consists of columnar grains with lengths of 82 ±30 nm and widths of 20 ±5 nm. It is not clear whether these grains exhibit the same separation into $Al_{0.51}Fe_{0.49}$ and $Al_{0.65}Fe_{0.35}$ phases that was observed in the bulk $Al_{0.56}Fe_{0.44}$ sample (Figure 33(b)). Fast Fourier transforms of HRTEM images and selected area diffraction patterns did confirm that the phase of some of the grains in the $Al_{0.58}Fe_{0.42}$ CSAF is cubic AlFe $Pm\bar{3}m$ (space group 221), consistent with the $Al_{0.51}Fe_{0.49}$ stoichiometry. However, a second phase consistent with the $Al_{0.65}Fe_{0.35}$ stoichiometry could not be identified conclusively.

FIB-TEM analyses similar to those discussed for $Al_{0.58}Fe_{0.42}$ above were performed at five other locations with expected CSAF compositions (based on the initial characterization) of $Al_{0.32}Fe_{0.64}Ni_{0.04}$, $Al_{0.30}Fe_{0.45}Ni_{0.25}$, $Al_{0.10}Fe_{0.21}Ni_{0.69}$, $Al_{0.09}Fe_{0.09}Ni_{0.82}$, and $Al_{0.06}Fe_{0.04}Ni_{0.90}$. STEM/TEM imaging revealed that the CSAF thicknesses at these locations were 123 ±5 nm, 125 ±2 nm, 76 ±4 nm, 60 ±3 nm, and 53 ±7 nm, respectively, decreasing as the Ni fraction in the film increased. Despite these thickness differences, the composition as determined by EDX measurements across large areas of the CSAF cross section was similar to the expected composition at all of the locations. A grain structure similar to that visible in Figure 34(d) was observed at the $Al_{0.32}Fe_{0.64}Ni_{0.04}$ and $Al_{0.30}Fe_{0.45}Ni_{0.25}$ locations (where the CSAF thickness was $>$120 nm), while the structure at the more Ni-rich locations (where the CSAF thickness was $<$80 nm) consisted of much smaller grains with characteristic length and width dimensions on the order of ~10 nm. Conclusive evidence of a multiphase equilibrium was not obtained with HRTEM at any of the sampled locations on the CSAF. However, it is worth noting that previous work at Carnegie Mellon University has shown directly using electron backscatter diffraction that ~100 nm-thick Cu_xPd_{1-x} CSAFs exhibit multiphase equilibria consistent with the bulk Cu_xPd_{1-x} phase diagram.[76] Thus, since the FIB-TEM studies

show that grains were formed in the $Al_xFe_yNi_{1-x-y}$ CSAF as a result of UHV annealing at 427 °C, it is likely that these grains exhibit the multiphase equilibria of bulk $Al_xFe_yNi_{1-x-y}$ at 427 °C.

Having investigated the microstructure of the bulk alloy samples, XPS was used to compare depth profiles of these samples after $t_{ox} = 4$ h with those of CSAF locations with similar composition; the results are shown in Figure 35. The bulk-alloy profiles were measured across ~0.13 mm^2 circular areas and are labeled with the average composition of each bulk sample determined by EDX (see Figure 33). The CSAF profiles were measured across ~0.03 mm^2 circular areas (spanning a total range of ~2 at.% in the composition gradients) and are labeled with the composition at the center of each area as determined with EDX at $t_{ox} = 0$ h. Identical Ar^+ etch conditions and time steps were used for all of the profiles in Figure 35; thus, the length scale of all the horizontal (i.e. depth) axes should be roughly equivalent and is approximated based on the appearance of the Mo substrate in the $Al_{0.66}Fe_{0.34}$ CSAF profile.

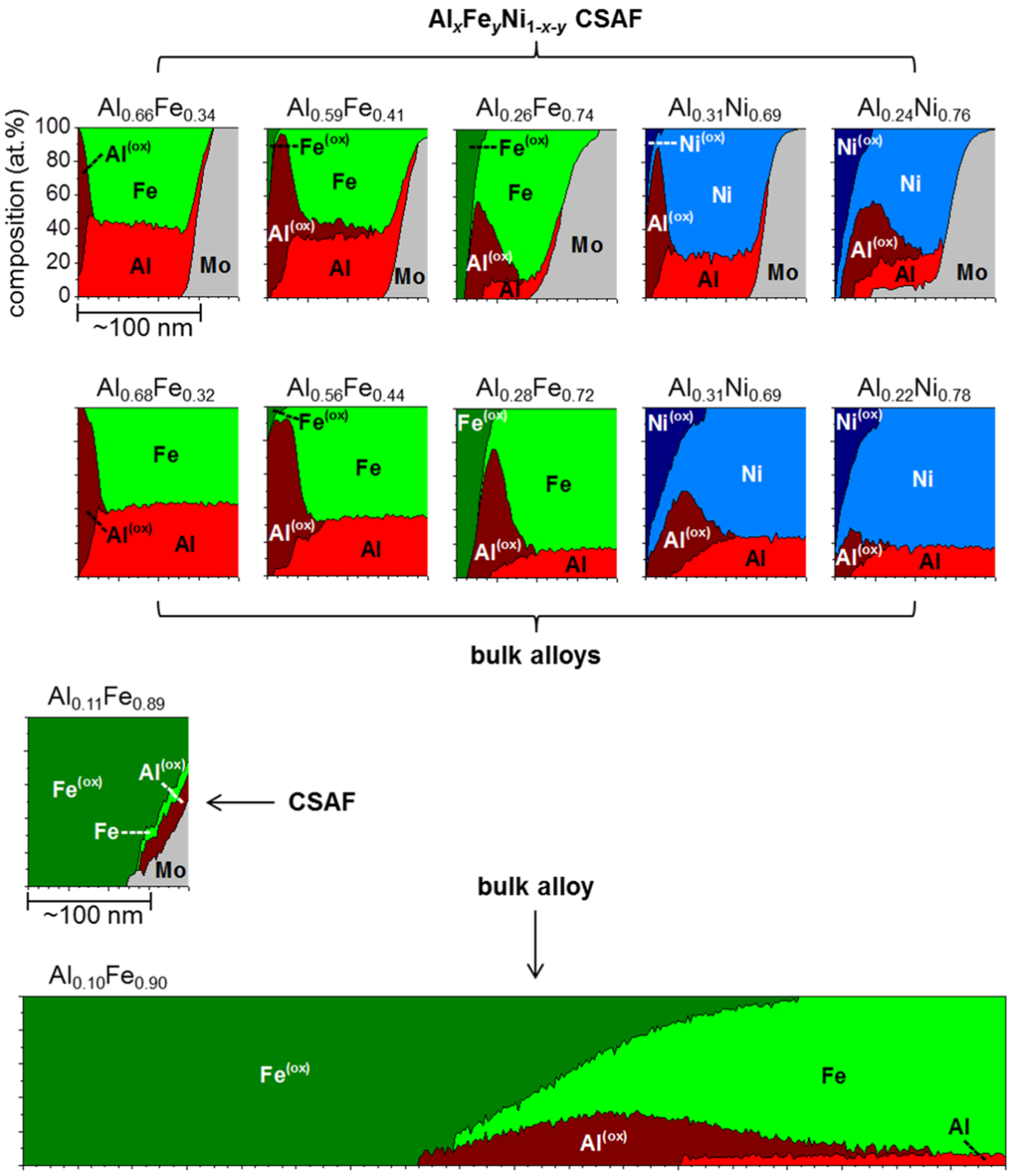

Figure 35. Comparison of XPS depth profiles measured on the bulk Al_xFe_{1-x} and Al_xNi_{1-x} samples with those measured at locations with similar compositions on an $Al_xFe_yNi_{1-x-y}$ CSAF (Mo substrate), both after t_{ox} = 4 h in dry air at 427 °C. The plots show the relative composition of each detected element, M, in a metallic, "M", or oxidized, "$M^{(ox)}$", chemical state as a function of total Ar^+ etch time. The labels above each profile are the CSAF or bulk composition measured with EDX at the profile location at t_{ox} = 0 h. Identical etch conditions were used for all of the profiles, so the depth increments corresponding to the tick marks on the horizontal axes should be roughly equivalent for all of the plots; an approximate length scale is shown below the $Al_{0.66}Fe_{0.34}$ and $Al_{0.11}Fe_{0.89}$ CSAF profiles. The $Al_{0.10}Fe_{0.90}$ bulk profile was measured using 6× more etch cycles than the other profiles and, thus, sampled ~6× further in total depth.

The $Al_{0.68}Fe_{0.32}$, $Al_{0.56}Fe_{0.44}$, and $Al_{0.28}Fe_{0.72}$ bulk depth profiles in Figure 35 are remarkably similar to the corresponding $Al_{0.66}Fe_{0.34}$, $Al_{0.59}Fe_{0.41}$, and $Al_{0.26}Fe_{0.74}$ CSAF depth profiles. This suggests that the oxidation behavior in dry air at 427 °C observed for regions 1, 2, and 3 in the Al_xFe_{1-x} section of the CSAF (see Figure 27(c)) is effectively the same as that of bulk alloys, despite both significant differences in grain structure (see Figures 33 and 34) and the much smaller amount of material available in the ~100 nm-thick CSAF. The $Al_{0.10}Fe_{0.90}$ (region 4) bulk profile required 6× more etch time than the other profiles to reach the depth at which the composition became uniform and metallic, indicating much more extensive Fe-oxide formation than on the other Al_xFe_{1-x} bulk samples. Based on the depth of oxide penetration revealed by the $Al_{0.10}Fe_{0.90}$ bulk profile, it is unsurprising that the $Al_{0.11}Fe_{0.89}$ CSAF profile shows essentially complete oxidation across the entire film. Due to depletion of the metallic components, the $Al_{0.11}Fe_{0.89}$ CSAF profile clearly cannot provide a representative picture of the oxide formation which occurs in bulk alloys with similar composition. However, it does plainly indicate that region 4 of the CSAF was not passivated by an Al_2O_3 scale, and simply making this distinction was the primary goal of our previous studies discussed in Chapters 3 and 4.[37,38]

The Al_xNi_{1-x} bulk depth profiles in Figure 35 do not match their corresponding CSAF profiles as closely as the Al_xFe_{1-x} pairs. One possible interpretation of the $Al_{0.31}Ni_{0.69}$ bulk profile is that it represents an average of two different types of behavior, where an Al_2O_3 scale is formed at the surface of the $Al_{0.38}Ni_{0.62}$ “dark” phase regions visible in Figure 33(e), and in the subsurface of the $Al_{0.28}Ni_{0.72}$ “light” phase regions. This explanation would be qualitatively consistent with the behavior identified individually for these compositions on the $Al_xFe_yNi_{1-x-y}$ CSAFs, as shown in Figure 27(c). It is very likely that the two phases oxidized essentially independently of one another in the bulk sample, given the characteristic dimensions of the grains relative to the thickness of the oxide layers that are formed. However, a sufficiently small grain size in a CSAF could allow significant lateral interactions between phases with differing composition. As mentioned previously in the discussion of the FIB-TEM results, Ni-rich locations on that particular $Al_xFe_yNi_{1-x-y}$ CSAF were comprised of very small grains with characteristic dimensions on the order of ~10 nm. Thus, it is possible that the differences between the $Al_{0.31}Ni_{0.69}$ bulk and the $Al_{0.31}Ni_{0.69}$ CSAF depth profiles in Figure 35 are related to differences in grain structure. A challenge in assessing the final pair of Al_xNi_{1-x} profiles at $Al_{0.24}Ni_{0.76}$ (CSAF) and $Al_{0.22}Ni_{0.78}$ (bulk) is that Ni oxidizes

slowly in dry air at 427 °C. As a result, the presence or absence of a passivating Al_2O_3 scale cannot be discerned easily based on the amount of Ni oxide that was formed, as can be done based on the amount of Fe oxide formed in Al_xFe_{1-x}. With this in mind, the $Al_{0.22}Ni_{0.78}$ bulk depth profile in Figure 35 suggests strongly that no passivating Al_2O_3 scale was formed, as it reveals no subsurface enrichment of Al oxide. The location at which the $Al_{0.24}Ni_{0.76}$ CSAF depth profile was measured became significantly roughened/pitted as a result of the oxidation (see Figure 31(a)), complicating its interpretation and making direct comparison with the $Al_{0.22}Ni_{0.78}$ bulk profile difficult. However, we have concluded based on additional analyses in our previous studies[37,38] that this region of the CSAF is not passivated by the formation of an Al_2O_3 scale.

5.2.4. Summary and outlook

By specifically focusing on Al_xFe_{1-x} and Al_xNi_{1-x} oxidation in dry air at 427 °C, we have investigated two aspects of the high-throughput methodology that we previously developed and applied to study oxidation using $Al_xFe_yNi_{1-x-y}$ CSAFs (see Figure 27) in the work reported in Chapters 3 and 4.[37,38] EDX measurements of oxygen-uptake kinetics (Figure 28) and XPS depth profiling (Figures 29, 30, and 31) showed that readily definable changes in the oxidation phenomenology of the CSAFs occur over composition ranges of ~1-2 at.% at boundaries between regions exhibiting different types of oxidation behavior. The ability to identify these boundaries continuously in real space on the CSAF surface allows precise measurement of $Al_xFe_yNi_{1-x-y}$ compositions at which important transitions in oxidation behavior occur, including the N_{Al}^{*} boundary separating compositions which form a passivating Al_2O_3 scale from those that do not. However, it is important to recognize that these results apply specifically to oxidation of ~100 nm-thick $Al_xFe_yNi_{1-x-y}$ films, which might differ from that of bulk alloys exposed to identical environments. Despite electron microscopy analyses (Figures 32, 33, and 34) revealing significant differences in the microstructure of bulk and CSAF samples, XPS depth profiling (Figure 35) showed remarkable agreement between the metal/oxide cross sections developed in the Al_xFe_{1-x} region of a CSAF and those developed in bulk alloys. Conversely, there were notable differences in the metal/oxide cross sections developed in the Al_xNi_{1-x} region of the CSAF and those developed in bulk alloys. Thus, at least in certain cases, it appears that microstructural differences might lead to practical issues with extrapolating our high-throughput results to bulk alloy systems. This concern aside, our work still clearly

demonstrates the potential value of applying high-throughput, CSAF-based methods to the study of oxidation in multicomponent alloys. Any issues related to differences in the oxidation behavior of CSAFs compared to bulk alloys could, in principle, be simply overcome given the ability to create sufficiently thick CSAFs. Additional component(s) could also be incorporated into the CSAFs to generate alloy libraries representing any plane through a quaternary or higher-order composition space. In this way, high-throughput methods similar to ours could be used to rapidly screen alloy oxidation in any given environment across continuous composition ranges of practical interest.

5.3. Experimental methods

5.3.1. $Al_xFe_yNi_{1-x-y}$ CSAF preparation

The $Al_xFe_yNi_{1-x-y}$ CSAFs were created using the RSM tool[4] (described in Chapter 1.2). The substrates used to support the CSAFs were polycrystalline-Mo blocks with dimensions $14\times14\times2.5$ mm^3. The CSAFs were created by evaporative deposition onto one of the 14×14 mm^2 faces (rms roughness $<$1.5 nm) of the substrates. After loading a substrate into the UHV chamber housing the RSM tool, the deposition face was sputtered for 20 min with a defocused, 2 kV Ar^+ beam (~5 μA sample current) to remove contaminants. The substrate was then annealed at 477 °C for 1 h, and allowed to cool to room temperature. Another cycle of Ar^+ sputtering was performed immediately before the CSAF deposition. To create the CSAF, the Al, Fe, and Ni were simultaneously deposited onto the substrate, each from a separate e-beam evaporator loaded with ≥99.98% pure source material. Prior to deposition, the QCM was used to measure the deposition rates and determine the power required for each of the evaporators to achieve approximately equal molar deposition rates. The deposition time for the CSAFs was 500 min, resulting in film thicknesses of ~100 nm. Immediately after its deposition, each CSAF was annealed at 427 °C for 2 h and cooled to room temperature in UHV. The chamber was then vented to atmosphere and the CSAF was exposed to ambient air at room temperature for ~15 min while it was transferred to a *Tescan* Vega3 SEM system with an operating pressure of $\sim1\times10^{-4}$ Torr.

5.3.2. EDX mapping of $Al_xFe_yNi_{1-x-y}$ CSAF composition gradients

Immediately following the deposition of each $Al_xFe_yNi_{1-x-y}$ CSAF, spatial mapping of the composition gradients was performed in the *Tescan* Vega3 SEM system using EDX measurements made

with an *Oxford Instruments* X-max 80 mm^2 detector. The detector was controlled by INCA Energy software and calibrated hourly with a pure Ni standard. EDX spectra were collected across the CSAF surface from 50×50 μm^2 areas arranged in a square grid with 1 mm spacing. The spectra were measured from 0-10 keV (10 eV binning, >300,000 total counts) at a working distance of 15 mm with the SEM beam operating at 11.24 kV. The CSAF composition at each location was determined by processing the collected spectra using the *Oxford Instruments* software package INCA ThinFilmID, which was used to account for the layering of the sample within the electron beam interaction volume. The assumption used in quantifying the spectra was that the $Al_xFe_yNi_{1-x-y}$ CSAF forms a flat, homogenous layer on the Mo substrate (based on FIB-TEM results like those shown in Figure 34, this appears to be an accurate approximation). Three separate measurements of composition were made at each location and averaged to reduce noise. The discrete $Al_xFe_yNi_{1-x-y}$ compositions determined in this way at the points located on the square grid on each CSAF were used to determine parameter values describing a best-fit CDM for each $Al_xFe_yNi_{1-x-y}$ CSAF (see Chapter 2), where A_{Al}, A_{Fe}, and A_{Ni} were each modeled using a linear wedge (Figure 4, Equation 2.1). The best-fit CDMs were used in determining the composition-space trajectories of the real-space boundaries observed on the CSAFs.

5.3.3. Oxidation of $Al_xFe_yNi_{1-x-y}$ CSAFs

After initial analyses of the $Al_xFe_yNi_{1-x-y}$ CSAFs were performed at $t_{ox} = 0$ h (deposited/annealed with ~15 min exposure to ambient air at room temperature), the CSAFs were incrementally exposed to dry air at 427 °C for total times of $t_{ox} = 1$, 2, and 4 h. The exposures were performed in a quartz tube (~2 cm in diameter and ~60 cm long) which was heated by a furnace, with one end connected to a gas-introduction manifold and the other end open to atmosphere. Prior to each exposure, the furnace was preheated until the temperature was stable at 427 ±1 °C while the manifold was used to maintain a continuous flow of ~1 slpm of dry air through the tube. The CSAF was then loaded into a ceramic boat (which was preheated with the furnace) and quickly pushed to the center of the tube. Only the bottom of the Mo substrate was in direct contact with the boat. At the end of each exposure increment, the sample was removed from the furnace, and the bottom of the substrate was placed in contact with a sheet of aluminum foil to quickly dissipate heat, cooling the CSAF to room temperature in ~2 min. Various

characterizations of the CSAF were then performed before proceeding with the next incremental exposure to dry air in the furnace.

5.3.4. EDX measurement of oxygen uptake during $Al_xFe_yNi_{1-x-y}$ CSAF oxidation

EDX was used to measure C_O (the total amount of oxygen present throughout the entire film cross section) as a function of composition across the $Al_xFe_yNi_{1-x-y}$ CSAFs after t_{ox} = 0, 1, 2, and 4 h. Each individual spectrum used to derive C_O was collected across a 50×50 μm^2 area of the CSAF surface. The locations of these areas were chosen (with guidance from the best-fit CDM) to provide a dense sampling of the $Al_xFe_yNi_{1-x-y}$ composition space. In total, 71 different binary Al_xFe_{1-x} compositions and 59 different binary Al_xNi_{1-x} compositions were sampled across two different CSAFs (corresponding to the data presented in Figure 28). The spectra used to derive C_O were measured from 0-10 keV (10 eV binning, >250,000 total counts) at a working distance of 15 mm with the SEM beam operating at 20 kV. An arbitrary value for C_O was calculated from the oxygen EDX signal scaled by the (much larger) Mo EDX signal from the substrate. As discussed in Chapter 3.2.4, the values of C_O calculated in this way are approximately proportional to the total amount of oxygen present across the CSAF because the depth sensitivity of 20 kV EDX is much greater than the CSAF thickness. Three separate measurements of C_O were made for each CSAF composition at each t_{ox} and averaged to reduce noise.

5.3.5. XPS depth profiling of oxidized $Al_xFe_yNi_{1-x-y}$ CSAFs

The XPS depth profiling of both the $Al_xFe_yNi_{1-x-y}$ CSAFs and the bulk alloys was performed in a *ThermoFisher* ThetaProbe instrument with a hemispherical energy analyzer. The XPS measurements were made using monochromated Al K_α X-rays; an X-ray spot diameter of ~200 μm was used for the profiles measured on the CSAFs, while a spot diameter of ~400 μm was used for the profiles measured on the bulk alloys. During each set of XPS measurements, spectra were acquired across 10-14 eV ranges of binding energies containing the non-overlapping Al 2s, Fe $2p_{1/2}$, Ni $2p_{3/2}$, and Mo $3p_{3/2}$ peaks. With the pass energy of the hemispherical analyzer held constant at 100 eV, the spectra were collected by scanning across each energy range in 0.05 eV steps with 0.2 s dwell time per step. The sets of XPS measurements were alternated with uniform etching of the analysis area by a rastered Ar^+ beam (3 kV, 1 μA) in 65 identical cycles (except for the $Al_{0.10}Fe_{0.90}$ bulk profile in Figure 35, for which 390 cycles were

used) to obtain XPS data as a function of depth into the samples. It is possible to discern whether the monitored species were in a metallic or oxidized chemical state based on the position of the peaks in their XPS spectra; oxidized metals have their peak binding energies increased by ~2-5 eV over the binding energies of the metallic species. The spectra were processed using *Thermo* Avantage software to fit metallic and/or oxidized peaks to each of the spectra. The geometric parameters used to define each of the peaks and examples of fit spectra are provided in Table 2 and Figure 14, respectively. The relative compositions of the elemental components were calculated by normalizing their total peak areas by Wagner sensitivity factors, while the metallic-to-oxidized ratio for each species was assumed to be equal to the ratio of the area of the metallic peak to the area of the oxidized peak(s).

5.3.6. Preparation and handling of Al_xFe_{1-x} and Al_xNi_{1-x} bulk samples

The Al_xFe_{1-x} and Al_xNi_{1-x} bulk samples were cast as ~700 cm^3 ingots at the United States Department of Energy National Energy Technology Laboratory facility in Albany, Oregon. Tokens with approximate dimensions of 7×7×2.5 mm^3 were cut from these ingots by wire electrical discharge machining. One 7×7 mm^2 face of each token was then mechanically polished in a sequence of seven steps, first using 1200 grit sandpaper, then 9, 6, 3, and 1 μm *Buehler* MetaDi Supreme Polycrystalline Diamond solutions, and finally 0.3 and 0.05 μm *Buehler* Micropolish II Alumina compounds. The 9, 6, and 3 μm solutions were applied using *Buehler* nylon pads, while the 1 μm solution and Micropolish II Alumina compounds were applied using *Buehler* microcloth. In between each step, the surface of the token was thoroughly rinsed with deionized water to remove any residual polishing material from the previous step. Visually, the surfaces of the tokens developed a mirror finish as a result of the polishing sequence. The tokens were then placed under UHV in the chamber housing the CSAF deposition tool, sputtered with a defocused, 2 kV Ar^+ beam (~1 μA current per token) for ~20 min, and annealed for 2 h at 427 °C. Similar to the $Al_xFe_yNi_{1-x-y}$ CSAFs, the tokens were exposed to ambient air at room temperature for ~15 min as they were transferred to the *Tescan* Vega3 SEM system for initial ($t_{ox} = 0$ h) characterization. The resulting roughness of the token surfaces was not quantified, but can be qualitatively assessed based on the SEM images shown in Figure 33. After initial characterization, the tokens were oxidized in dry air at 427 °C for 4 h by the same procedures used for the $Al_xFe_yNi_{1-x-y}$ CSAFs.

5.3.7. SEM imaging

All SEM imaging was performed in the *Tescan* Vega3 system at a working distance of 11 mm with the beam operating at 20 kV. The electron beam diameter was ~90 nm and the scan rate was 1 ms per pixel. The SEM images of the $Al_xFe_yNi_{1-x-y}$ CSAF surfaces (Figures 29, 30, and 31) were generated by secondary electron detection, while those of the bulk Al_xFe_{1-x} and Al_xNi_{1-x} alloy surfaces (Figures 32 and 33) were generated by BSE detection.

5.3.8. EDX of bulk alloy samples

The compositions shown for the bulk Al_xFe_{1-x} and Al_xNi_{1-x} alloys in Figure 33 were determined from EDX spectra processed using the default quantification routine in the INCA Energy software. These spectra were measured from 0-10 keV (5 eV binning, >200,000 total counts) at a working distance of 15 mm with the SEM beam operating at 20 kV. The "average" compositions were determined from spectra measured while rastering the beam over an ~700×500 μm^2 area on the surface, while the compositions of the "light" and "dark" phases were determined from spectra acquired with the beam held stationary (sampling an ~0.5×0.5 μm^2 area). Each of the compositions shown in Figure 33 is the average of 5 individual measurements.

5.3.9. FIB-TEM analyses of $Al_xFe_yNi_{1-x-y}$ CSAF

Cross sections of the $Al_xFe_yNi_{1-x-y}$ CSAF sent to Inmetro were prepared by FIB using an *FEI* Nova NanoLab 600 and were analyzed by TEM in a C_s-corrected *FEI* Titan 80-300 (300 kV operating voltage) equipped with an X-FEG filament and monochromator. Conventional bright-field and dark-field TEM images were processed using DigitalMicrograph software. STEM images were acquired using a *Gatan* bright-field/annular dark-field detector with a camera length of 38 mm and a convergence semi-angle of 27.3 mrad. EDX spectra used for chemical analyses were measured using an *EDAX* analyzer. EDX elemental maps were acquired by a drift-corrected STEM spectrum imaging experiment and processed using TIA software. A combination of measurements using HRTEM, selected area diffraction, nanobeam diffraction, and EDX were used to identify the AlFe $Pm\bar{3}m$ phase in the $Al_{0.58}Fe_{0.42}$ cross section of the CSAF.

Chapter 6. Quaternary CSAF methods: oxidation of $(Al_xFe_yNi_{1-x-y})_{\sim 0.8}Cr_{\sim 0.2}$

6.1. Introduction

In recent years, an increasingly wide variety of problems in materials science have been studied using CSAF-based combinatorial methods.[1–3] However, the vast majority of this work has used binary or ternary CSAFs, as was the case for our studies of $Al_xFe_yNi_{1-x-y}$ CSAF oxidation described in Chapters 3, 4, and 5. Examples of studies involving quaternary or higher-order CSAFs[77–82] are far less common. In addition, in all such studies of which we are aware, at least some of the components are incorporated into the CSAFs in fixed ratios (most often as stoichiometric oxides). This approach reduces the degrees of freedom in the prepared composition range (making it easier to present and interpret the results of high-throughput measurements made across the CSAFs), but also constrains the regions of composition space that can be accessed. For example, a quaternary CSAF of elements A-B-C-D created using A, B, and CD as base components can only access compositions with a C:D ratio of 1, i.e. $A_xB_y(CD)_{1-x-y}$ where ($0 \leq x \leq 1$, $0 \leq y \leq [1 - x]$). The work reported in this Chapter explores the preparation and characterization of quaternary CSAFs for a more general case in which none of the alloy components are incorporated in fixed ratios. Specifically, we investigate the preparation of $(Al_xFe_yNi_{1-x-y})_{1-z}Cr_z$ CSAFs using the RSM tool[4] described in Chapter 1.2. We then perform a case study of the oxidation of these CSAFs (related to the work described in Chapters 3, 4, and 5) to demonstrate how such a sample can be used to investigate alloy oxidation across a continuously defined region of quaternary $(Al_xFe_yNi_{1-x-y})_{1-z}Cr_z$ composition space. The primary goal of this case study was to identify the N^*_{Al} boundary for oxidation of an $(Al_xFe_yNi_{1-x-y})_{1-z}Cr_z$ CSAF in dry air at 427 °C, and compare it to the N^*_{Al} boundary that we have previously measured[37] for ternary $Al_xFe_yNi_{1-x-y}$ CSAFs in the same environment (Chapter 3).

6.2. Results and discussion

6.2.1. Quaternary CSAFs

CSAFs are ideal for combinatorial screening across composition space of any alloy property which can be rapidly measured at discrete locations across a surface. Lateral composition gradients afford up to two degrees of freedom in the composition range that can be generated in any given CSAF.

In the case of a ternary alloy, $A_xB_yC_{1-x-y}$, this is sufficient to produce a continuous spread of all possible compositions ($x = 0 \rightarrow 1$, $y = 0 \rightarrow [1 - x]$) across a finite, two-dimensional (2D) region of physical space. For example, Figure 36(a) reproduces the schematic from Figure 1, showing a full-range $A_xB_yC_{1-x-y}$ CSAF with a triangular geometry resembling a ternary composition diagram. However, because the composition range of an *n*-component CSAF is constrained to a 2D surface in an (*n* – 1)-dimensional composition space, it is not possible for a CSAF to continuously span the entire composition space of a quaternary or higher-order alloy. The simplest approach for using a CSAF to study such alloys would instead be to prepare a specific plane of interest through the composition space. The schematic in Figure 36(b) shows an example of a CSAF containing a single plane through quaternary A-B-C-D composition space. In principle, by fixing the atomic fraction of D at a constant value, *z*, an $(A_xB_yC_{1-x-y})_{1-z}D_z$ CSAF could contain all possible *relative* compositions of $A_xB_yC_{1-x-y}$ ($x = 0 \rightarrow 1$, $y = 0 \rightarrow [1 - x]$) by using a gradient geometry that is otherwise identical to that shown for the ternary CSAF in Figure 36(a).

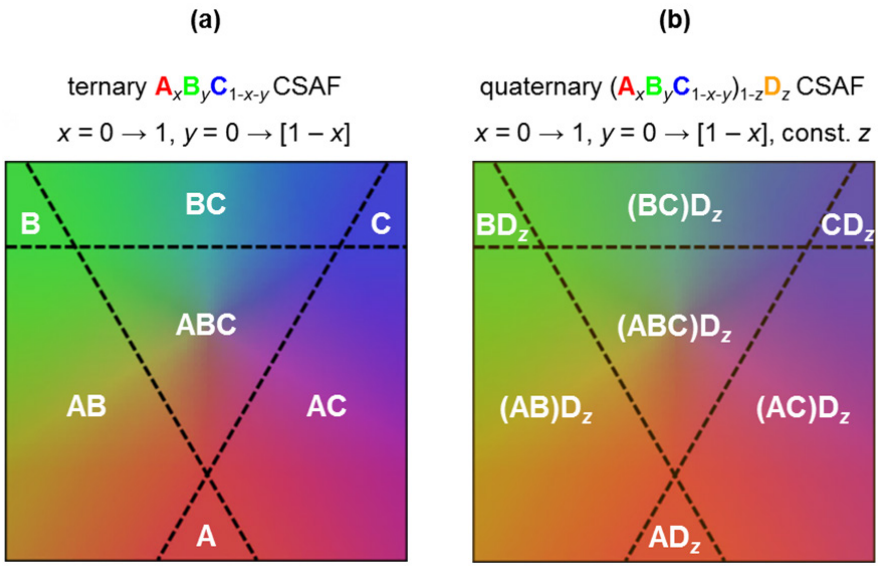

Figure 36. **(a)** Schematic depiction of a ternary CSAF containing all possible compositions of $A_xB_yC_{1-x-y}$. **(b)** Schematic depiction of a quaternary CSAF containing all possible relative compositions of $A_xB_yC_{1-x-y}$ where *z*, the atomic fraction of component D, is constant.

To investigate practical aspects of working with quaternary CSAFs, we attempted to prepare a sample like that shown in Figure 36(b), with a constant $z = 0.2$, and where the components A-B-C-D were Al-Fe-Ni-Cr, respectively. The CSAF was prepared under ultra-high vacuum (UHV) using the using the RSM tool[4] described in Chapter 1.2. For the work described in Chapters 3, 4, and 5, we developed the ability to use the RSM tool to prepare ~100 nm-thick $Al_xFe_yNi_{1-x-y}$ CSAFs with composition gradients closely resembling those shown in Figure 36(a).[37–39] In attempting to prepare a quaternary $(Al_xFe_yNi_{1-x-y})_{0.8}Cr_{0.2}$ CSAF, we used Al, Fe, and Ni evaporation procedures identical to those used for making the $Al_xFe_yNi_{1-x-y}$ CSAFs, while a fourth, unmasked source deposited a roughly uniform amount of Cr across the substrate with a flux that was ~25% of the maximum molar flux of the other components. After deposition, the CSAF was UHV-annealed for 2 h at 427 °C in the RSM tool and then transferred to an SEM for composition mapping using EDX. Spatially resolved measurements of CSAF composition were made across a 13×13 grid with 1 mm spacing, which was centered on the face of the substrate. Figure 37 shows contour plots of the relative Al, Fe, Ni, and Cr compositions of the CSAF as a function of real-space position based on these 169 discrete measurements. The measured Al, Fe, and Ni concentrations in the CSAF each vary from 0 to ~80 at.% across the region, but the measured Cr concentration varies from 9 to 25 at.%, revealing that the sample deviates measurably from an "ideal" $(Al_xFe_yNi_{1-x-y})_{0.8}Cr_{0.2}$ CSAF, for which the Cr concentration would be constant at 20 at.%. These observed variations in the Cr atomic fraction are not caused by non-uniform Cr deposition, but result from the specific nature of the gradients produced independently for each of the other components, as will be demonstrated by the following discussion regarding the modeling of the CSAF's composition distribution.

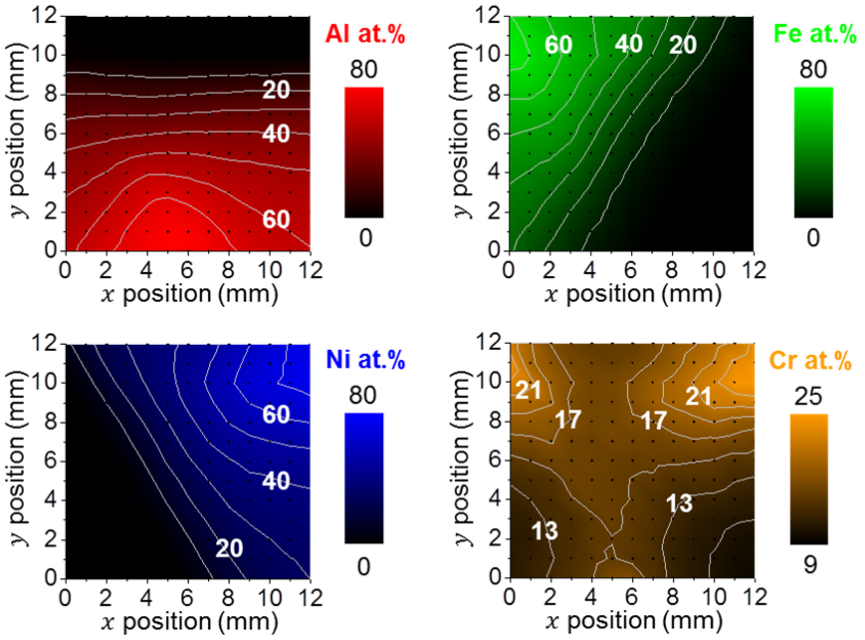

Figure 37. Real-space contour plots of the relative Al, Fe, Ni, and Cr concentrations in the quaternary CSAF as measured with EDX. The contours are fit based on discrete measurements made with 1 mm spacing on a regular grid.

To better understand the composition gradients obtained in the quaternary CSAF, the data shown in Figure 37 was used to determine parameter values describing a best-fit CDM (see Chapter 2). Because the Al, Fe, and Ni were deposited from three independently shadow-masked sources, A_{Al}, A_{Fe}, and A_{Ni} were each modeled using a linear wedge (Figure 4, Equation 2.1). The Cr was deposited from an unmasked source to obtain a relatively uniform flux across the surface and, thus, A_{Cr} was modeled using a plane (Equation 2.2). Defining $A_{\mathrm{Al}}(x,y)$, $A_{\mathrm{Fe}}(x,y)$, and $A_{\mathrm{Ni}}(x,y)$ by Equation 2.1 and $A_{\mathrm{Cr}}(x,y)$ by Equation 2.2, the values of 15 parameters are needed to evaluate $N_i(x,y)$ across the quaternary CSAF surface: h_i, w_i, α_i, and θ_i for each Al, Fe, and Ni, and $A_i(1{,}11)$, $A_i(11{,}11)$, and $A_i(6{,}1)$ for Cr. Table 4 shows the values of these parameters describing the best-fit CDM for the CSAF, as determined by performing a least-squares regression of N_i^{CDM} values (defined by Equation 2.3) compared to the 676 N_i^{msrd} values plotted in Figure 37. A schematic visualization of the best-fit CDM is shown in Figure 38 next to a photograph of the CSAF, on which the (x,y) coordinate system and the grid of 169 points at which N_i^{msrd} values were obtained are superimposed.

Table 4. Parameter values defining the best-fit CDM for the quaternary CSAF.

	w_i	h_i	α_i	θ_i
Al	7.6 mm	1.00	908 mm	179.38°
Fe	6.2 mm	0.69	5.1 mm	63°
Ni	4.9 mm	0.54	5.7 mm	299°
	$A_i(1,11)$	$A_i(6,1)$	$A_i(11,11)$	
Cr	0.21	0.19	0.18	

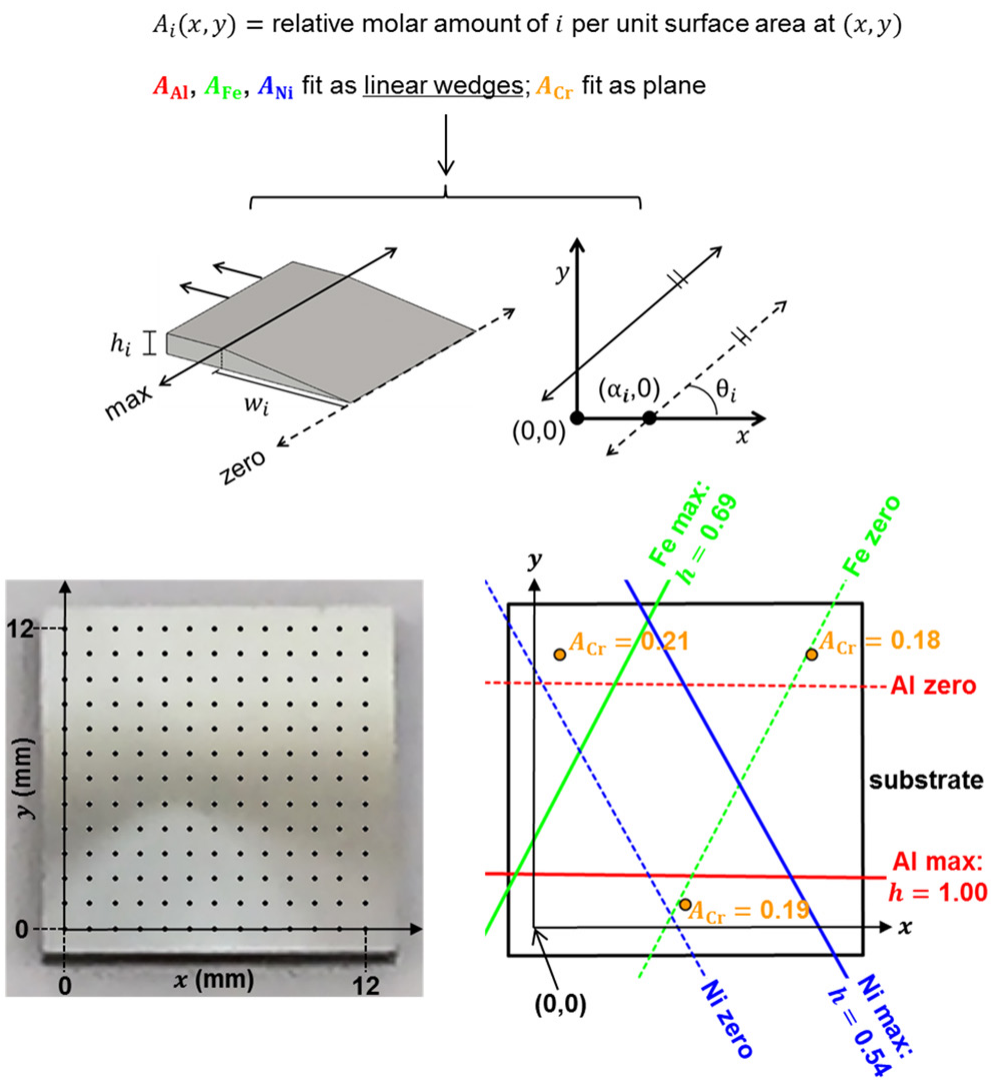

Figure 38. **Top:** The "linear wedge" surface used in the CDM to describe $A_{\mathrm{Al}}(x,y)$, $A_{\mathrm{Fe}}(x,y)$, and $A_{\mathrm{Ni}}(x,y)$ in terms of the parameters h_i, w_i, α_i, and θ_i. **Bottom (left):** Photograph of the quaternary CSAF with an overlaid grid of real-space coordinates across which the compositions used to fit the CDM were measured. **Bottom (right):** Graphical depiction of the best-fit CDM showing the wedge boundaries for $A_{\mathrm{Al}}(x,y)$, $A_{\mathrm{Fe}}(x,y)$, and $A_{\mathrm{Ni}}(x,y)$. $A_{\mathrm{Cr}}(x,y)$ is modeled as the plane passing through the three points labeled with the values of A_{Cr}.

The accuracy of the CDM fit to the CSAF's composition distribution can be assessed by comparing the values of N_i^{CDM} and N_i^{msrd} on a point-by-point basis. Figure 39 presents histograms of the difference in these two values for each component at the 169 locations analyzed on the CSAF. These histograms provide an indication of how accurately the best-fit CDM represents the actual CSAF composition distribution (as would be measured with EDX) within the bounds of the analyzed grid: 49% of the N_i^{msrd} values agree with N_i^{CDM} to within ±0.5 at.%, 83% agree to within ±1.5 at.%, and 95% agree to within ±2.5 at.%. As discussed in Chapter 3.3.1, the absolute accuracy with which EDX can be used to determine CSAF composition is likely no better than ±2 at.%. Based on the histograms in Figure 39, the CDM appears to be adequate for describing the local composition to within ±2 at.% across the vast majority of the CSAF.

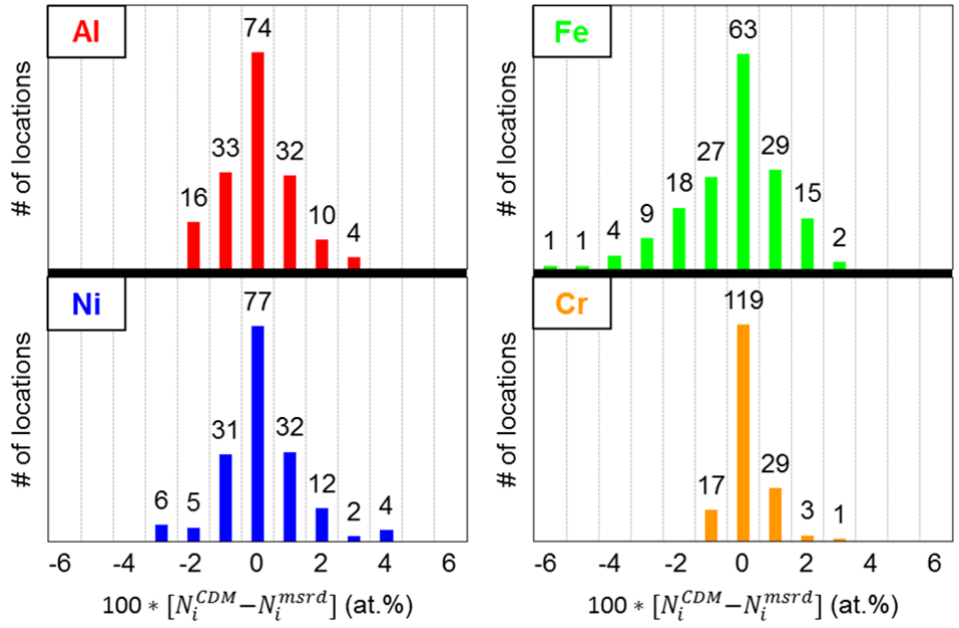

Figure 39. Histograms for each alloy component showing the difference between the compositions predicted by the best-fit CDM and the measured compositions used for the fitting. The numbers above each bar indicate the number of points (from a total of 169) falling within the range indicated on the horizontal axes.

Accepting the best-fit CDM (defined by the parameter values in Table 4 and shown schematically in Figure 38) as sufficiently accurate, it can be used to assess the nature of the composition gradients obtained in the quaternary CSAF, and how they differ from an "ideal" $(Al_xFe_yNi_{1-x-y})_{0.8}Cr_{0.2}$ CSAF with a

geometry like that shown in Figure 36(b). A photograph of the CSAF with an overlay of the A_{Al}, A_{Fe}, and A_{Ni} "wedge" boundaries defined by the CDM is shown in the upper left of Figure 40. The dashed lines represent the edges at which A_i reaches zero, while the solid lines represent the edges at which A_i reaches a constant maximum value (see Figure 38). Recalling that Cr was co-deposited across the entire substrate, these boundaries reveal which components are present in different regions of the CSAF. The triangular region bounded by the three dashed lines is the Al-Fe-Ni-Cr quaternary region, as shown in the upper right of Figure 40. The CSAF also contains Al-Fe-Cr, Fe-Ni-Cr, and Al-Ni-Cr ternary regions, as well as Fe-Cr, Ni-Cr, and Al-Cr binary regions. The Al-Fe-Ni-Cr region is divided into four sub-regions, across each of which the gradient of A_i is constant for each component. As a result, the composition range contained within any one of these sub-regions falls on a single plane through the three-dimensional (3D) quaternary composition space. All compositions lying on such a plane can be described as a linearly weighted average of three fixed (binary and/or ternary) compositions. This allows the composition range of each sub-region to be represented using a single "pseudoternary" composition diagram, where the axes indicate the weighting fraction of these three fixed compositions rather than pure component fractions, as in standard ternary composition diagrams. The gradients of $A_{\mathrm{Al}}(x, y)$, $A_{\mathrm{Fe}}(x, y)$, and $A_{\mathrm{Ni}}(x, y)$ change upon crossing the solid lines along which their maxima are reached. Thus, the segments of these lines falling within the Al-Fe-Ni-Cr quaternary region delineate an intersection of two different planes through the 3D quaternary composition space, each of which must be represented using a different pseudoternary composition diagram. Four pseudoternary diagrams (one for each sub-region) are required to represent the range of compositions present in the quaternary region of the CSAF in Figure 40. Compositions from the remaining binary or ternary regions can simply be plotted on standard ternary composition diagrams.

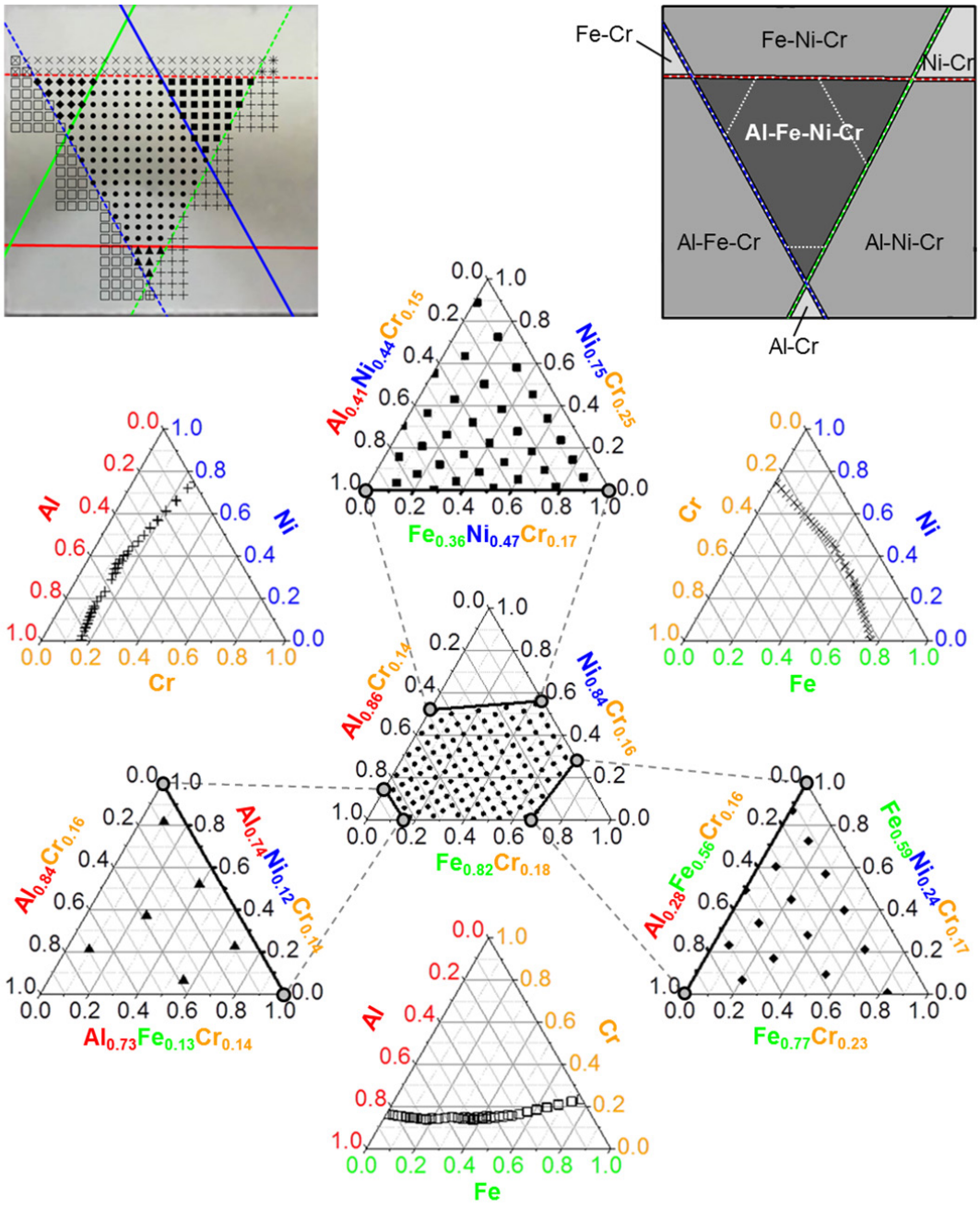

Figure 40. Top (left): A regularly spaced grid on the quaternary CSAF surface (photographed) relative to the CDM-defined wedge boundaries for $A_{\mathrm{Al}}(x,y)$, $A_{\mathrm{Fe}}(x,y)$, and $A_{\mathrm{Ni}}(x,y)$. **Top (right):** The components contained in different regions of the CSAF, as determined based on the wedge boundaries. **Bottom:** The set of 7 different composition diagrams (4 pseudoternary, 3 ternary) required to rigorously represent all of the CSAF compositions predicted by the CDM at the points shown on the grid at top left. Corresponding sets of points are indicated with matching symbols.

The points shown on the CSAF in the upper left of Figure 40 fall on a regular grid (0.5 mm spacing) from which data were collected for the oxidation study which will be presented in Chapter 6.2.2.

The CSAF composition at each point can be plotted on at least one of the seven diagrams shown in the bottom of Figure 40. Four of these are the pseudoternary composition diagrams describing the composition range of the Al-Fe-Ni-Cr quaternary region, while the remaining three are standard ternary composition diagrams describing all possible compositions for which $N_i = 0$ for at least one of the four components. The points on the diagrams and their corresponding points on the CSAF are indicated with matching symbols. The complete set of diagrams is necessary to rigorously represent the full range of compositions contained in the quaternary CSAF according to the CDM (Figure 38). The four pseudoternary composition diagrams are sample-specific, and would change if any of the CDM parameters in Table 4 were changed. This complicates the comparison of property measurements made across any two quaternary CSAFs which are not precisely identical. However, based on the diagrams in Figure 40, the sample could be approximately described as an $(Al_xFe_yNi_{1-x-y})_{\sim 0.8}Cr_{\sim 0.2}$ CSAF (containing all compositions where $x = 0 \rightarrow 1$, $y = 0 \rightarrow [1 - x]$) for simplified comparison with similar CSAFs.

6.2.2. $(Al_xFe_yNi_{1-x-y})_{\sim 0.8}Cr_{\sim 0.2}$ CSAF oxidation in dry air at 427 °C

To demonstrate how the principles discussed in Chapter 6.2.1 can be related to high-throughput oxidation studies, we performed a simple case study by oxidizing the $(Al_xFe_yNi_{1-x-y})_{\sim 0.8}Cr_{\sim 0.2}$ CSAF in dry air at 427 °C. Our primary goal was to identify the continuous N^*_{Al} boundary separating alloy compositions which form a passivating Al_2O_3 scale from those that do not. We showed in the work described in Chapters 3, 4, and 5 that, for $Al_xFe_yNi_{1-x-y}$ CSAFs oxidized at 427 °C, passivated compositions can be revealed based on EDX measurements of the total oxygen content, C_{O}, as a function of total exposure time to the environment, t_{ox}.[37–39] For $t_{ox} > 1$ h, compositions which had formed a passivating Al_2O_3 scale exhibited a measurably lower ΔC_{O} with additional t_{ox} than those which were not passivated.[37–39]

C_{O} was measured across the $(Al_xFe_yNi_{1-x-y})_{\sim 0.8}Cr_{\sim 0.2}$ CSAF for different values of t_{ox} in dry air at 427 °C on the grid shown in Figure 40. Figure 41 shows the ΔC_{O} from $t_{ox} = 1$ to 16 h plotted using a color scale on the set of composition diagrams introduced in Figure 40. The data are displayed using continuous contours (fit based on measurements at the discrete compositions indicated by white points) on the four pseudoternary composition diagrams representing the quaternary region, while each point is individually color-coded in the three ternary composition diagrams. Figure 41 reveals an abrupt increase

in ΔC_O with decreasing N_{Al} across the entire range of compositions contained in the CSAF. Based on our previous studies of ternary $Al_xFe_yNi_{1-x-y}$ CSAF oxidation (Chapters 3, 4, and 5), we proceed assuming that this increase occurs upon crossing the N_{Al}^* boundary on the $(Al_xFe_yNi_{1-x-y})_{\sim 0.8}Cr_{\sim 0.2}$ CSAF, i.e. the boundary between compositions which formed a passivating Al_2O_3 scale in dry air at 427 °C and those that did not. We do not attempt to further verify this, as referring nonspecifically to the boundary along which the observed increase in ΔC_O occurs as "N_{Al}^*" provides a suitable basis for all subsequent discussion of the present case study, regardless of its physical significance.

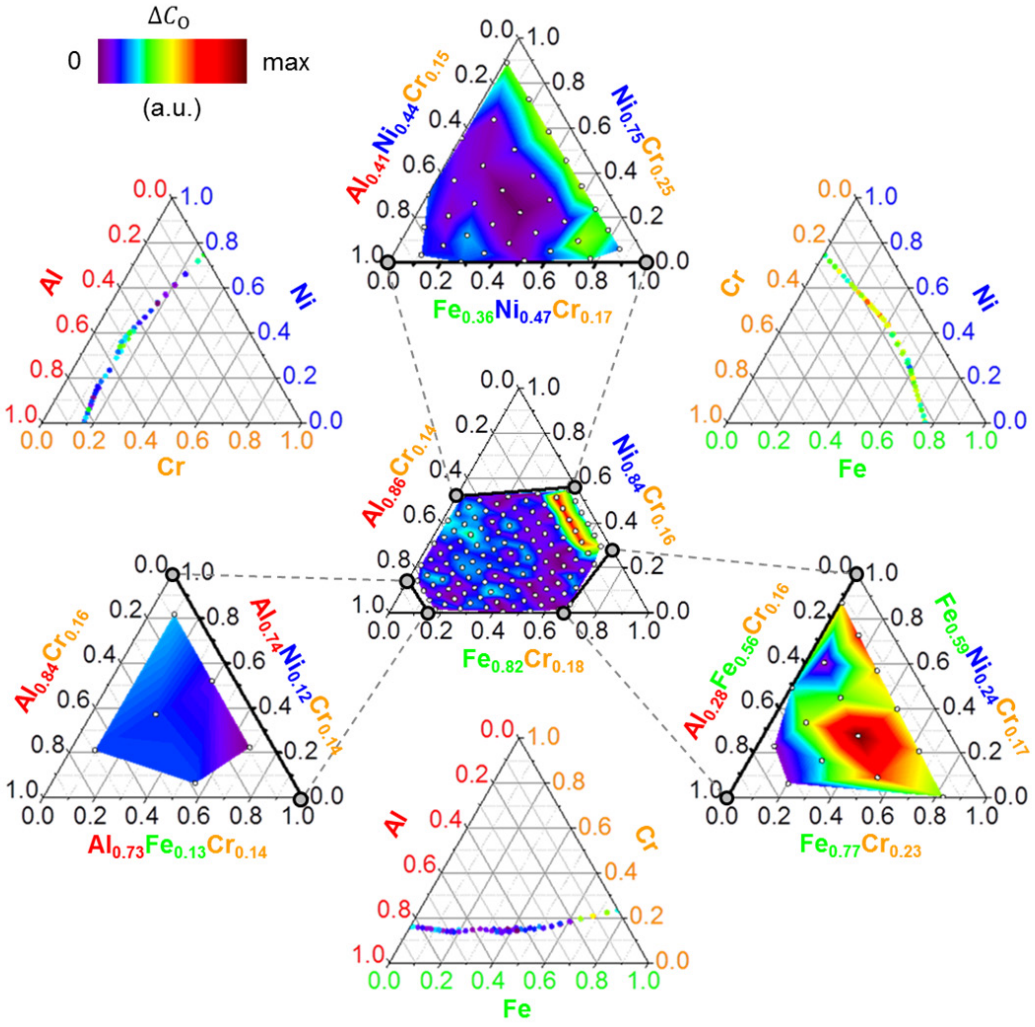

Figure 41. EDX-measured oxygen uptake (ΔC_O, arbitrary units) between $t_{ox} = 1$ and 16 h in dry air at 427 °C as a function of the $(Al_xFe_yNi_{1-x-y})_{\sim 0.8}Cr_{\sim 0.2}$ CSAF composition. The pseudoternary diagrams show continuous contours fit to the discrete measurements made at the white points, while each point is individually color-coded in the ternary diagrams.

Given the spacing of the discrete points at which ΔC_{O} was measured, it is difficult to propose a precise trajectory of N_{Al}^{*} through the diagrams based solely on the data in Figure 41. A key finding from the studies described in Chapters 3, 4, and 5 was that the discoloration patterns developed on $Al_xFe_yNi_{1-x-y}$ CSAFs as a result of their oxidation in dry and humid air at 427 °C reveal the real-space trajectory of N_{Al}^{*} across their surfaces. As simple visual analysis could then be used to map the N_{Al}^{*} boundary precisely in real space on the $Al_xFe_yNi_{1-x-y}$ CSAFs, the CDMs fit to those CSAFs could be used to estimate the continuous composition-space trajectory of N_{Al}^{*}.[37–39] Here, we consider whether N_{Al}^{*} might similarly be visually identified on the $(Al_xFe_yNi_{1-x-y})_{\sim 0.8}Cr_{\sim 0.2}$ CSAF. Figure 42(a) shows a photograph of an $Al_xFe_yNi_{1-x-y}$ CSAF oxidized for 4 h in dry air at 427 °C in the study described in Chapter 3, with the location of the ternary composition region (see Figure 36(a)) marked for reference. The abrupt change in surface discoloration indicated by the solid white line was found to correlate with N_{Al}^{*}, as determined by EDX measurements of C_{O} and ΔC_{O}.[37] Figure 42(b) shows the $(Al_xFe_yNi_{1-x-y})_{\sim 0.8}Cr_{\sim 0.2}$ CSAF after oxidation for 16 h in dry air at 427 °C with the location of the quaternary region marked for reference (see Figure 40). Many aspects of the appearances of the two oxidized CSAFs in Figure 42 are significantly different. The rate at which the visual appearance of the $(Al_xFe_yNi_{1-x-y})_{\sim 0.8}Cr_{\sim 0.2}$ CSAF changed with increasing t_{ox} was found to be much slower than that of the $Al_xFe_yNi_{1-x-y}$ CSAF (thus, a maximum t_{ox} of 16 h was used instead of 4 h). However, by $t_{ox} = 16$ h, the $(Al_xFe_yNi_{1-x-y})_{\sim 0.8}Cr_{\sim 0.2}$ CSAF does appear to exhibit a well-defined boundary at which the surface discoloration increases abruptly with decreasing Al content, similar to the N_{Al}^{*} boundary on the $Al_xFe_yNi_{1-x-y}$ CSAF for $t_{ox} = 4$ h.

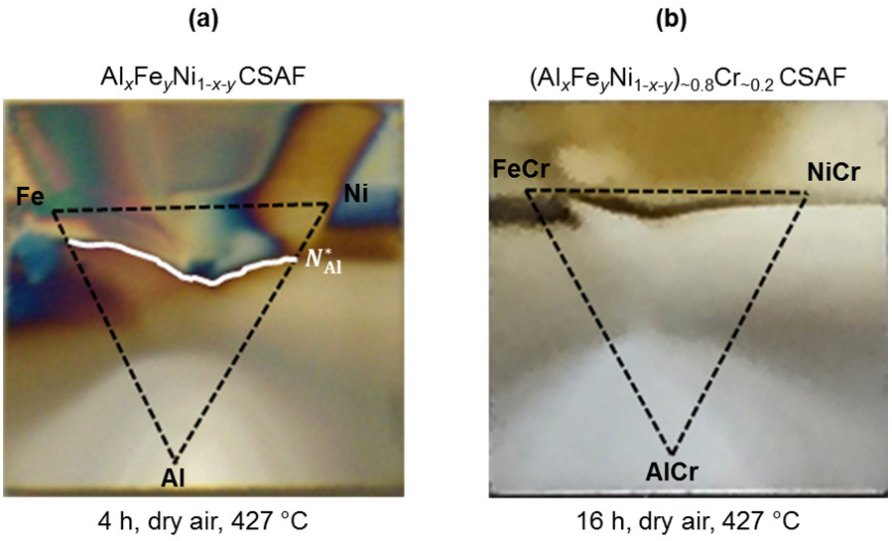

Figure 42. **(a)** Photograph of an $Al_xFe_yNi_{1-x-y}$ CSAF exposed to dry air at 427 °C for $t_{ox} = 4$ h. The real-space trajectory of N^*_{Al} can be identified visually based on surface discoloration. **(b)** Photograph of the $(Al_xFe_yNi_{1-x-y})_{\sim 0.8}Cr_{\sim 0.2}$ CSAF exposed to dry air at 427 °C for $t_{ox} = 16$ h. Significantly more discoloration occurred as the result of oxidation near the top of the CSAF (at low values of N_{Al}) than across the remainder of its surface.

To determine whether the abrupt change in surface discoloration of the $(Al_xFe_yNi_{1-x-y})_{\sim 0.8}Cr_{\sim 0.2}$ CSAF visible in Figure 42(b) is correlated with N^*_{Al}, we used the best-fit CDM for the sample (see Table 4 and Figure 38) to compare the composition-space trajectory of the visually observed boundary with the ΔC_O data shown in Figure 41. The trajectory of the observed boundary across the quaternary region of the $(Al_xFe_yNi_{1-x-y})_{\sim 0.8}Cr_{\sim 0.2}$ CSAF is shown as a dashed black line on the photograph in Figure 43(a). The boundary traverses three of the four planes through quaternary composition space. The composition-space trajectory of the boundary (as calculated with the CDM) is superimposed on the three pseudoternary composition diagrams in Figure 43(a), showing the measured ΔC_O from $t_{ox} = 1$ to 16 h across these planes. For reference, the white square and triangle mark the corresponding ends of the boundary on the photograph and diagrams. The visually observable boundary correlates well with the abrupt increase in ΔC_O and, therefore, does appear to reveal the trajectory of N^*_{Al} on the $(Al_xFe_yNi_{1-x-y})_{\sim 0.8}Cr_{\sim 0.2}$ CSAF.

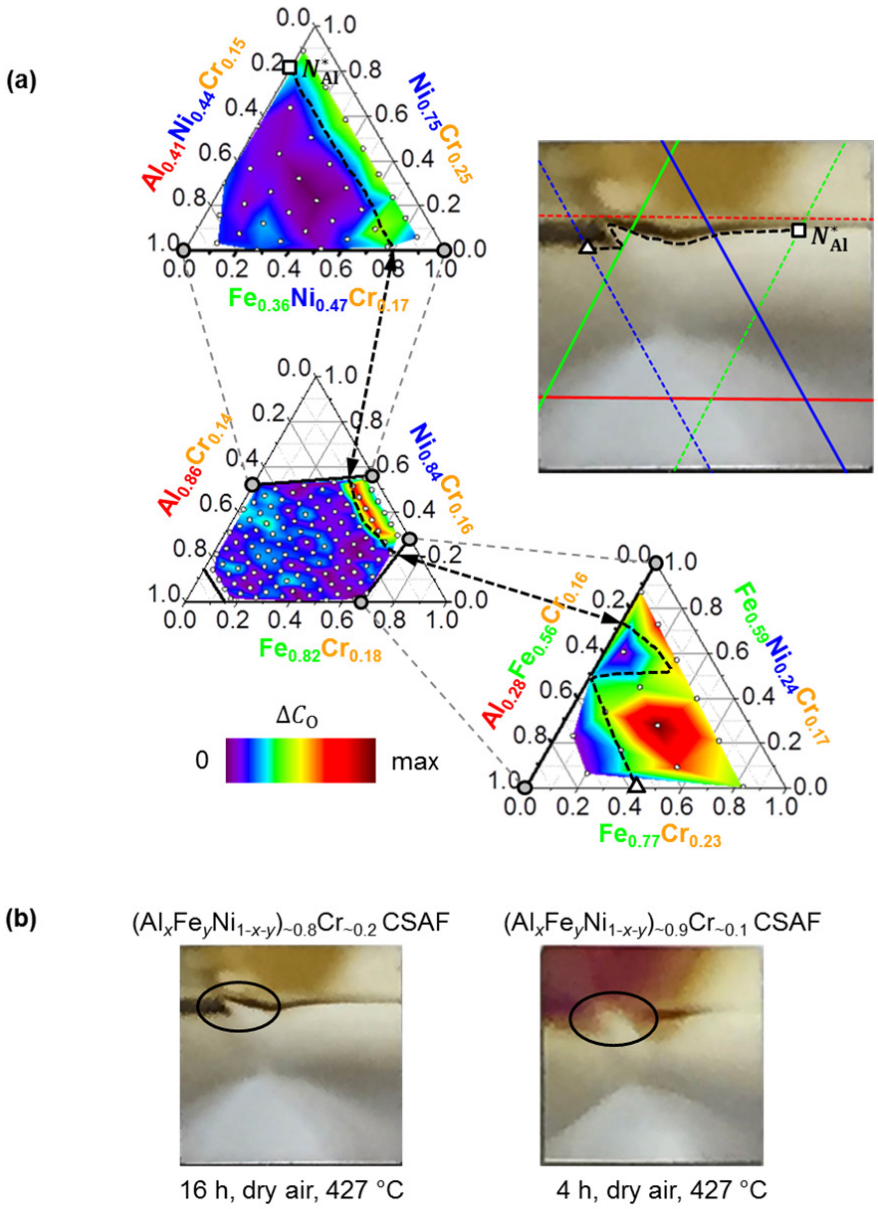

Figure 43. **(a)** The real-space boundary on the photograph at right was identified based on the discoloration of the oxidized (t_{ox} = 16 h in dry air at 427 °C) $(Al_xFe_yNi_{1-x-y})_{\sim 0.8}Cr_{\sim 0.2}$ CSAF surface. The continuous composition-space trajectory of the boundary predicted by the CDM is shown in the three pseudoternary diagrams. Its clear correlation with an abrupt increase in oxygen uptake (ΔC_O, arbitrary units) upon decreasing the Al content suggests that this boundary is N^*_{Al}. **(b)** A similar "kink" feature to that circled on the photograph of the oxidized $(Al_xFe_yNi_{1-x-y})_{\sim 0.8}Cr_{\sim 0.2}$ CSAF (left) was also observed on a $(Al_xFe_yNi_{1-x-y})_{\sim 0.9}Cr_{\sim 0.1}$ CSAF (right), indicating that it arises from a reproducible physical effect of alloy composition.

Because we can determine the real-space trajectory of boundaries on a CSAF with an accuracy of about ±0.1 mm (see Chapter 3.3.2), the visual analysis in Figure 43(a) allows the trajectory of N^*_{Al} to be

determined much more precisely than is possible based only on the ΔC_O data in Figure 41, which was measured with 0.5 mm spacing on the grid shown in Figure 40. For example, the point where $\Delta C_O \cong 0$ at $Al_{0.09}Fe_{0.59}Ni_{0.15}Cr_{0.17} = [Al_{0.28}Fe_{0.56}Cr_{0.16}]_{0.32}[Fe_{0.77}Cr_{0.23}]_{0.07}[Fe_{0.59}Ni_{0.24}Cr_{0.17}]_{0.61}$ appears to be an outlier in the lower right pseudoternary diagram in Figure 41, but in Figure 43(a) it clearly lies within an interesting "kink", where the value of N_{Al}^* abruptly decreases as the Ni-to-Fe ratio increases. The inherent advantage of high-throughput screening methods lies in their ability to reveal complex trends in composition-property relationships, like that represented by this kink. To qualitatively explore the reproducibility and relevance of the kink feature on the $(Al_xFe_yNi_{1-x-y})_{\sim 0.8}Cr_{\sim 0.2}$ CSAF, we prepared a second CSAF with similar gradient geometry, but approximately half the Cr content. EDX composition mapping similar to that shown in Figure 37 confirmed that the second sample could be approximately described as an $(Al_xFe_yNi_{1-x-y})_{\sim 0.9}Cr_{\sim 0.1}$ CSAF. Photographs of the $(Al_xFe_yNi_{1-x-y})_{\sim 0.8}Cr_{\sim 0.2}$ CSAF after exposure to dry air at 427 °C for $t_{ox} = 16$ h and the $(Al_xFe_yNi_{1-x-y})_{\sim 0.9}Cr_{\sim 0.1}$ CSAF after exposure to an identical environment for $t_{ox} = 4$ h are compared in Figure 43(b). No significant changes in the discoloration of the $(Al_xFe_yNi_{1-x-y})_{\sim 0.9}Cr_{\sim 0.1}$ CSAF were observed between $t_{ox} = 1$ and 4 h (consistent with the behavior we have observed previously for $Al_xFe_yNi_{1-x-y}$ CSAFs[37,38]), so it was not oxidized beyond $t_{ox} = 4$ h. The final appearance of the oxidized $(Al_xFe_yNi_{1-x-y})_{\sim 0.9}Cr_{\sim 0.1}$ CSAF appears to be intermediate to that of the oxidized $(Al_xFe_yNi_{1-x-y})_{\sim 0.8}Cr_{\sim 0.2}$ CSAF and oxidized $Al_xFe_yNi_{1-x-y}$ CSAFs[37] (e.g. Figure 42(a)). A kink similar to that observed on the $(Al_xFe_yNi_{1-x-y})_{\sim 0.8}Cr_{\sim 0.2}$ CSAF is also visible on the $(Al_xFe_yNi_{1-x-y})_{\sim 0.9}Cr_{\sim 0.1}$ CSAF; these features are circled on the images of the CSAFs in Figure 43(b). It is not surprising that the feature is less pronounced on the $(Al_xFe_yNi_{1-x-y})_{\sim 0.9}Cr_{\sim 0.1}$ CSAF than on the $(Al_xFe_yNi_{1-x-y})_{\sim 0.8}Cr_{\sim 0.2}$ CSAF, given that it is not observed at all on $Al_xFe_yNi_{1-x-y}$ CSAFs[37] (e.g. Figure 42(a)) and, therefore, must eventually disappear entirely as the Cr content decreases. The appearance of the kink on both samples shown in Figure 43(b) suggests that these features do, in fact, arise from a reproducible physical effect related to oxidation of $(Al_xFe_yNi_{1-x-y})_{1-z}Cr_z$ CSAFs in dry air at 427 °C, which is an interesting phenomenon revealed by our high-throughput approach.

The boundary shown in the composition diagrams in Figure 43(a) is a rigorous 2D representation of a continuous trajectory of N_{Al}^* in dry air at 427 °C, which we have directly measured through the $(Al_xFe_yNi_{1-x-y})_{1-z}Cr_z$ composition space. However, the value of *z* can be regarded as being roughly

constant for simplified comparison with the N^*_{Al} boundary that we have measured previously for $Al_xFe_yNi_{1-x-y}$ CSAFs in the same environment (see Chapter 3). This allows values of N^*_{Al} as a function of the Fe-to-Ni ratio to be compared directly for CSAFs with and without the addition of ~20 at.% Cr (i.e. for $z \cong 0.2$ and $z = 0$). Figure 44(a) shows this comparison with N^*_{Al} plotted as a function of N_{Fe} / (N_{Fe} + N_{Ni}). The error bars represent the estimated uncertainty arising from the accuracy of our visual determination of the real-space coordinates lying along the N^*_{Al} boundaries. The precise values of N_{Cr} measured along the $N_{\mathrm{Cr}} \cong 0.2$ boundary vary systematically between ~0.17 and ~0.23, and are shown in Figure 44(b). By comparing the N^*_{Al} boundaries in Figure 44(a), it can be seen that the addition of ~20 at.% Cr to an $Al_xFe_yNi_{1-x-y}$ CSAF does not appear to significantly affect the value of N^*_{Al} for oxidation in dry air at 427 °C when N_{Fe} / (N_{Fe}+ N_{Ni}) > 0.85. However, at N_{Fe} / (N_{Fe}+ N_{Ni}) ≅ 0.85, the value of N^*_{Al} abruptly decreases in the $(Al_xFe_yNi_{1-x-y})_{\sim 0.8}Cr_{\sim 0.2}$ CSAF and remains significantly lower than in the $Al_xFe_yNi_{1-x-y}$ CSAFs across the remainder of composition space. This abrupt decrease in the value of N^*_{Al} corresponds with the kink feature circled in Figure 43(b). While this is an interesting observation, its physical origins are not further considered here, as this case study is simply intended to demonstrate methods for high-throughput screening of alloy oxidation across continuous quaternary composition spaces.

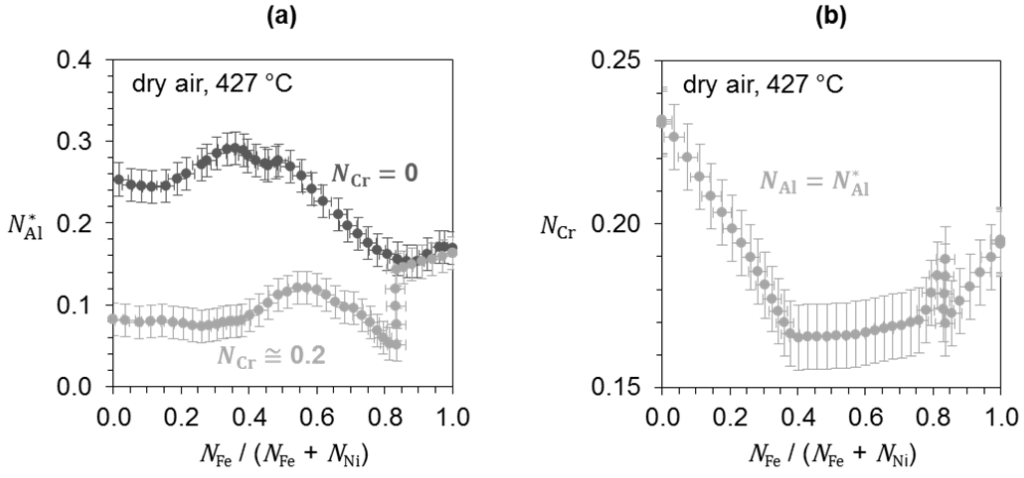

Figure 44. **(a)** A comparison of N^*_{Al} in dry air at 427 °C across all Fe-to-Ni ratios in $Al_xFe_yNi_{1-x-y}$ and $(Al_xFe_yNi_{1-x-y})_{\sim 0.8}Cr_{\sim 0.2}$, as determined by high-throughput CSAF experimentation. N^*_{Al} is significantly lower for $(Al_xFe_yNi_{1-x-y})_{\sim 0.8}Cr_{\sim 0.2}$ when N_{Fe} / (N_{Fe} + N_{Ni}) ≤ 0.85. **(b)** The precise values of N_{Cr} along the measured N^*_{Al} boundary in $(Al_xFe_yNi_{1-x-y})_{\sim 0.8}Cr_{\sim 0.2}$.

6.2.3. Conclusions

While the continuous composition range contained in a quaternary CSAF is, by definition, constrained to a 2D surface in the 3D composition space, the characterization and representation of this surface can pose a number of challenges. Provided a high degree of control over CSAF preparation, the ideal approach would be to prepare a quaternary CSAF spanning a composition range that falls on a plane through quaternary composition space and, therefore, can be represented by a single 2D composition diagram. This can be accomplished without coupling any of the CSAF components in a fixed ratio if the A_i (moles per unit surface area) gradient is constant for each component across the surface. For less ideal cases, a CSAF's composition distribution might still be modeled continuously across its surface, given a reasonable means of estimating $A_i(x,y)$ for each component. However, the ability to rigorously represent such model-predicted composition ranges using 2D diagrams can be complicated depending on the complexity of the function(s) describing $A_i(x,y)$. Well-characterized CSAFs can serve as ideal platforms for high-throughput screening of composition-property relationships across continuous quaternary alloy composition space, as demonstrated by our case study of oxidation using an $(Al_xFe_yNi_{1-x-y})_{\sim 0.8}Cr_{\sim 0.2}$ CSAF. In principle, many of the specific concepts discussed in this Chapter could also be extended to studies using quinary or higher-order CSAFs.

6.3. Experimental methods

6.3.1. $(Al_xFe_yNi_{1-x-y})_{1-z}Cr_z$ CSAF preparation

The $(Al_xFe_yNi_{1-x-y})_{1-z}Cr_z$ CSAFs were created under UHV conditions at ~5×10^{-10} Torr using the RSM tool[4] described in Chapter 1.2. Using the tool, the four CSAF components were co-deposited onto a 14×14 mm^2 polycrystalline-Mo substrate (2.5 mm thick, rms roughness <1.5 nm). The deposition faces of the substrates were initially sputtered for 20 min with a defocused, 2 kV Ar^+ beam (~5 μA sample current) to remove contaminants. The substrates were then annealed at 477 °C for 1 h, and cooled to room temperature. The Ar^+ sputtering was repeated immediately before the CSAFs were deposited. To create the CSAFs, the Al, Fe, Ni, and Cr were deposited onto the substrate simultaneously, each from a separate e-beam evaporator (≥99.98% pure source material). Before deposition, the QCM was used to measure the deposition rate from each source to determine appropriate power settings such that the Al,

Fe, and Ni had approximately equal maximum molar deposition fluxes that were ~4× and ~9× greater than that of the Cr for the $(Al_xFe_yNi_{1-x-y})_{\sim 0.8}Cr_{\sim 0.2}$ and $(Al_xFe_yNi_{1-x-y})_{\sim 0.9}Cr_{\sim 0.1}$ CSAF, respectively. The shadow mask above the Cr evaporator was removed to obtain uniform A_{Cr} across the CSAFs. The mask orientations and alignments used for the Al, Fe, and Ni evaporators were identical to those previously used to create full-range $Al_xFe_yNi_{1-x-y}$ CSAFs.[37,38] Each CSAF was deposited for 500 min, resulting in a total film thickness of ~100 nm. After deposition, the CSAFs were annealed at 427 °C for 2 h and cooled to room temperature in UHV. After the chamber was vented to atmosphere, the CSAFs were exposed for ~15 min to ambient air at room temperature while they were transferred to a *Tescan* Vega3 SEM for analysis of their composition distributions.

6.3.2. EDX mapping of $(Al_xFe_yNi_{1-x-y})_{1-z}Cr_z$ CSAF composition gradients

Immediately following the deposition of each CSAF, spatial mapping of its composition distribution was performed in a *Tescan* Vega3 SEM operated at ~1×10^{-4} Torr. EDX spectra were collected using an *Oxford Instruments* X-max 80 mm^2 detector controlled by INCA Energy software. The detector was calibrated once hourly with pure Ni. Individual spectra were measured across 50×50 μm^2 areas of the surface with 1 mm spacing on a regular grid. The spectra were measured from 0-10 keV (10 eV binning, >350,000 total counts) at a working distance of 15 mm with the SEM beam operating at 13.52 kV. The CSAF compositions (as shown in Figure 37) were determined by processing the collected spectra using the Oxford Instruments software package INCA ThinFilmID, which was used to account for inhomogeneous layering within the electron beam interaction volume. The spectra were quantified under the assumption that the $(Al_xFe_yNi_{1-x-y})_{1-z}Cr_z$ CSAF forms a flat layer which is homogenous and well-adhered to the Mo substrate (FIB-TEM results like those from Figure 34 in Chapter 4 have shown this to be an accurate approximation for similar $Al_xFe_yNi_{1-x-y}$ CSAFs). The composition measurements were repeated three times at each location and averaged to reduce noise.

6.3.3. Oxidation of $(Al_xFe_yNi_{1-x-y})_{1-z}Cr_z$ CSAFs

After initial analysis at $t_{ox} = 0$ h (deposited/annealed, ~15 min exposure to ambient atmosphere), each $(Al_xFe_yNi_{1-x-y})_{1-z}Cr_z$ CSAF was exposed in increments to dry air at 427 °C for a total time, t_{ox}. The exposures were performed in a tube furnace (quartz tube, ~2 cm in diameter and ~60 cm long), with one

end open to atmosphere and the other end connected to a gas-introduction manifold. The furnace was preheated prior to each exposure such that its temperature was stable at 427 ±1 °C while a continuous flow of ~1 slpm of dry air was applied through the tube using the manifold. The CSAF was loaded into the furnace in a ceramic boat (which was preheated with the furnace), such that only the bottom of the Mo substrate was in direct contact with the boat. The CSAF was removed from the furnace at the end of each incremental exposure, and the bottom of its substrate was placed in contact with aluminum foil to dissipate heat, cooling to room temperature in ~2 min.

6.3.4. EDX measurement of oxygen uptake in $(Al_xFe_yNi_{1-x-y})_{\sim 0.8}Cr_{\sim 0.2}$ CSAF

EDX measurements of C_O (the total amount of oxygen present across the entire CSAF cross section) as a function of position across the $(Al_xFe_yNi_{1-x-y})_{\sim 0.8}Cr_{\sim 0.2}$ CSAF were made after t_{ox} = 0, 1, 4, and 16 h. The spectra used to derive C_O were collected across 50×50 μm^2 areas of the CSAF surface centered at the points on the grid in Figure 40. In total, 344 different locations were sampled. The spectra used to derive C_O were measured from 0-10 keV (10 eV binning, >300,000 total counts) at a working distance of 15 mm with the SEM beam operating at 30 kV. Arbitrary values for C_O were calculated as the oxygen EDX signal scaled by the (much larger) Mo EDX signal from the substrate. As discussed in Chapter 4.2.4, the C_O values calculated in this way are approximately proportional to the total amount of oxygen present across the entire CSAF cross section because the depth sensitivity of 30 kV EDX is much greater than the CSAF thickness. Three individual measurements of C_O were made at each location for each t_{ox}, and averaged to reduce noise. The data shown in Figures 41 and 43(a) are the ΔC_O from t_{ox} = 1 to 16 h, i.e. $C_O(t_{ox} = 16\text{ h}) - C_O(t_{ox} = 1\text{ h})$.

Chapter 7. Thesis summary and recommendations for follow-up research

The work described in this thesis has outlined the development, implementation, and assessment of a high-throughput methodology for studying alloy oxidation across multicomponent composition space using CSAFs (Chapter 1.1) prepared with an RSM tool[4] (Chapter 1.2). Specifically, we have studied the oxidation of $Al_xFe_yNi_{1-x-y}$ in dry air at 427 °C[37] (Chapter 3), $Al_xFe_yNi_{1-x-y}$ in humid air at 427 °C[38] (Chapter 4), and $(Al_xFe_yNi_{1-x-y})_{\sim 0.8}Cr_{\sim 0.2}$ in dry air at 427 °C[40] (Chapter 6), where ($x = 0 \rightarrow 1$, $y = 0 \rightarrow [1 - x]$) in each case. Critical assessment of our methodology (Chapter 5) revealed that well-defined transitions in the oxidation behavior of the CSAFs occur at sharp boundaries in composition space, including the transition from internal oxidation to Al_2O_3 scale passivation at N_{Al}^{*}. In each of the studies described in Chapters 3, 4, and 6, the N_{Al}^{*} boundaries could be identified visually in real space across the surfaces of oxidized CSAFs based on their discoloration. The CDM developed to describe the composition gradients of CSAFs created with the RSM tool (Chapter 2) was used to determine the continuous composition-space trajectories of these real-space N_{Al}^{*} boundaries. Figure 45 shows a comparison of the three boundaries, with N_{Al}^{*} plotted as a function of N_{Fe} / (N_{Fe} + N_{Ni}). Relative to $Al_xFe_yNi_{1-x-y}$ oxidation in dry air, it was expected that adding humidity to the oxidizing environment should increase the value of N_{Al}^{*} (see Chapter 4.1), while adding Cr to the alloy should decrease the value of N_{Al}^{*} (see Chapter 1.4). Figure 45 shows that these expected trends are observed across most, but not all, of composition space. An inherent advantage of using CSAFs for combinatorial screening lies in their ability to reveal unexpected physical trends in composition-property relationships.

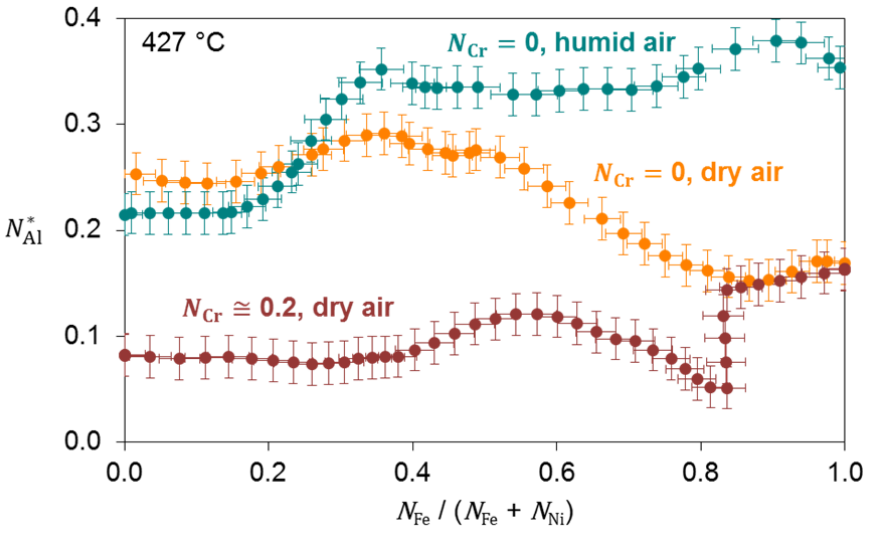

Figure 45. A comparison of the N^*_{Al} boundaries across all Fe-to-Ni ratios for $Al_xFe_yNi_{1-x-y}$ oxidation in dry air at 427 °C, $Al_xFe_yNi_{1-x-y}$ oxidation in humid air (10 mol% H_2O) at 427 °C, and $(Al_xFe_yNi_{1-x-y})_{\sim 0.8}Cr_{\sim 0.2}$ oxidation in dry air at 427 °C, as measured using ~100 nm-thick CSAFs.

Due to constraints associated with the e-beam evaporators in the RSM tool, the thickness of the CSAFs we have used in our oxidation studies has been limited to ~100 nm. For this reason, we were forced to study early-stage oxidation occurring at much lower temperatures and over much shorter times than are typically considered for practical applications of alumina-forming alloys. However, results like those shown in Figure 45 clearly demonstrate the potential value of using CSAF-based combinatorial methods to rapidly identify both compositional and environmental effects on multicomponent alloy oxidation. It is recommended that any follow-up to this work attempt to develop methods for performing oxidation studies of bulk-representative CSAFs at temperatures and in chemical environments of direct industrial relevance. In principle, this would require: 1) that both the thickness of the CSAFs and the lateral length of their composition gradients be large relative to the thickness of the oxide layers which are developed in the given environments, and 2) that the preparation of the CSAFs induce a grain structure similar to that of the bulk alloys of interest. Provided these challenges were addressed, the oxidation behavior of any spatially resolved region of a CSAF surface would be identical to that of a single-composition bulk alloy. Such CSAFs could then directly support the design of new alloys by allowing continuous measurement of relevant N^*_{Al} trajectories through ternary or higher-order composition spaces.

References

(1) Gebhardt, T.; Music, D.; Takahashi, T.; Schneider, J. M. Combinatorial Thin Film Materials Science: From Alloy Discovery and Optimization to Alloy Design. *Thin Solid Films* **2012**, *520* (17), 5491–5499.

(2) Zhao, J. C. Combinatorial Approaches as Effective Tools in the Study of Phase Diagrams and Composition-Structure-Property Relationships. *Prog. Mater. Sci.* **2006**, *51* (5), 557–631.

(3) Potyrailo, R.; Rajan, K.; Stowe, K.; Takeuchi, I.; Chisholm, B.; Lam, H. Combinatorial and High-Throughput Screening of Materials Libraries : Review of State of the Art. *ACS Comb. Sci.* **2011**, *13*, 579–633.

(4) Fleutot, B.; Miller, J. B.; Gellman, A. J. Apparatus for Deposition of Composition Spread Alloy Films: The Rotatable Shadow Mask. *J. Vac. Sci. Technol. A Vacuum, Surfaces, Film.* **2012**, *30* (6), 061511: 1–10.

(5) Prescott, R.; Graham, M. J. The Formation of Aluminum Oxide Scales on High-Temperature Alloys. *Oxid. Met.* **1992**, *38* (Nos. 3/4), 233–254.

(6) Wood, G.; Stott, F. Oxidation of Alloys. *Mater. Sci. Technol.* **1986**, *3*, 519–530.

(7) Zhang, Z. G.; Gesmundo, F.; Hou, P. Y.; Niu, Y. Criteria for the Formation of Protective Al_2O_3 Scales on Fe–Al and Fe–Cr–Al Alloys. *Corros. Sci.* **2006**, *48* (3), 741–765.

(8) Brady, M. P.; Yamamoto, Y.; Santella, M. L.; Walker, L. R. Composition, Microstructure, and Water Vapor Effects on Internal/External Oxidation of Alumina-Forming Austenitic Stainless Steels. *Oxid. Met.* **2009**, *72* (5-6), 311–333.

(9) Stott, F. H.; Wood, G. C.; Stringer, J. The Influence of Alloying Elements on the Development and Maintenance of Protective Scales. *Oxid. Met.* **1995**, *44* (1/2), 113–145.

(10) Young, D. J. *High Temperature Oxidation and Corrosion of Metals*; Elsevier Science Limited, 2008.

(11) Prescott, R.; Graham, M. J. The Oxidation of Iron-Aluminum Alloys. *Oxid. Met.* **1992**, *38* (1-2), 73–87.

(12) Chattopadhyay, B.; Wood, G. C. The Transient Oxidation of Alloys. *Oxid. Met.* **1970**, *2* (4), 373–399.

(13) Brady, M. P.; Gleeson, B.; Wright, I. G. Alloy Design Strategies for Promoting Protective Oxide-Scale Formation. *JOM* **2000**, *52* (1), 16–21.

(14) Stott, F. H.; Wood, G. C. Internal Oxidation. *Mater. Sci. Technol.* **1988**, *4* (December), 1072–1077.

(15) Zhao, W.; Gleeson, B. Steam Effects on the Oxidation Behaviour of Al_2O_3-Scale Forming Ni-Based Alloys. *Oxid. Met.* **2013**, *79* (5-6), 613–625.

(16) Pint, B. A.; DiStefano, J. R.; Wright, I. G. Oxidation Resistance: One Barrier to Moving Beyond Ni-Base Superalloys. *Mater. Sci. Eng. A* **2006**, *415* (1-2), 255–263.

(17) Pint, B. A.; Leibowitz, J.; DeVan, J. H. The Effect of an Oxide Dispersion on the Critical Al Content in Fe-Al Alloys. *Oxid. Met.* **1999**, *51* (1/2), 181–197.

(18) Kitajima, Y.; Hayashi, S.; Nishimoto, T.; Narita, T.; Ukai, S. Rapid Formation of α-Al_2O_3 Scale on an Fe–Al Alloy by Pure-Metal Coatings at 900 °C. *Oxid. Met.* **2009**, *73* (3-4), 375–388.

(19) Metting, C. J.; Bunn, J. K.; Underwood, E.; Smoak, S.; Hattrick-Simpers, J. Combinatorial Approach to Turbine Bond Coat Discovery. *ACS Comb. Sci.* **2013**.

(20) DeVan, J. H.; Tortorelli, P. F. The Oxidation-Sulfidation Behavior of Iron Alloys Containing 16-40 at% Aluminum. *Corros. Sci.* **1993**, *35* (5-8), 1065–1071.

(21) Delaunay, D.; Huntz, A. M. Mechanisms of Adherence of Alumina Scale Developed during High-Temperature Oxidation of Fe-Ni-Cr-Al-Y Alloys. *J. Mater. Sci.* **1982**, *17*, 2027–2036.

(22) Sakiyama, M.; Tomaszewicz, P.; Wallwork, G. Oxidation of Iron-Nickel Aluminum Alloys in Oxygen at 600–800° C. *Oxid. Met.* **1979**, *13* (4).

(23) Wood, G. C.; Chattopadhyay, B. Transient Oxidation of Ni-Base Alloys. *Corros. Sci.* **1970**, *10* (December 1969), 471–480.

(24) Pérez, P.; Jiménez, J.; Frommeyer, G.; Adeva, P. Oxidation Behaviour of a Ti–46Al–1Mo–0.2Si Alloy: The Effect of Mo Addition and Alloy Microstructure. *Mater. Sci. …* **2000**, *284*, 138–147.

(25) Jedlinski, J.; Glazkov, A.; Konopka, M.; Borchardt, G.; Tscherkasova, E.; Bronfin, M.; Nocun, M. An XPS/SEM/EDX Study of the Early Oxidation Stages of the Fe-19Cr-5Al (+ Y) Alumina-Forming Alloys. *Appl. Surf. …* **1996**, *103*, 205–216.

(26) Giggins, C.; Pettit, F. Oxidation of Ni-Cr-Al Alloys Between 1000° and 1200° C. *J. Electrochem. Soc.* **1971**, 1782–1790.

(27) Huang, J.; Fang, H.; Fu, X.; Huang, F.; Wan, H.; Zhang, Q.; Deng, S.; Zu, J. High-Temperature Oxidation Behavior and Mechanism of a New Type of Wrought Ni–Fe–Cr–Al Superalloy up to 1300 ° C. *Oxid. Met.* **2000**, *53* (3/4), 273–287.

(28) Nicholls, J. R.; Hancock, P.; Al Yasiri, L. H. Optimising Oxidation Resistance of MCrAl Coating Systems Using Vapour Phase Alloy Design. *Mater. Sci. Technol.* **1989**, *5* (August), 799–805.

(29) Yamamoto, Y.; Brady, M. P.; Santella, M. L.; Bei, H.; Maziasz, P. J.; Pint, B. A. Overview of Strategies for High-Temperature Creep and Oxidation Resistance of Alumina-Forming Austenitic Stainless Steels. *Metall. Mater. Trans. A* **2011**, *42A* (April), 922–931.

(30) Brady, M.; Yamamoto, Y.; Santella, M.; Maziasz, P.; Pint, B.; Liu, C.; Lu, Z.; Bei, H. The Development of Alumina-Forming Austenitic Stainless Steels for High-Temperature Structural Use. *JOM* **2008**, July, 12–18.

(31) Tawancy, H. M.; Sridhar, N. High-Temperature Oxidation Behavior of a Ni-Cr-Al-Fe-Y Alloy. *Oxid. Met.* **1992**, *37* (3/4), 143–166.

(32) Mu, N.; Jung, K.; Yanar, N. M.; Pettit, F. S.; Holcomb, G. R.; Howard, B. H.; Meier, G. H. The Effects of Water Vapor and Hydrogen on the High-Temperature Oxidation of Alloys. *Oxid. Met.* **2013**, *79* (5-6), 461–472.

(33) Wallwork, G. R.; Hed, A. Z. Some Limiting Factors in the Use of Alloys at High Temperatures. *Oxid. Met.* **1971**, *3* (2), 171–184.

(34) Wagner, C. Reaktionstypen Bei Der Oxydation von Legierungen. *Zeitschrift für Elektrochemie* **1959**, *63*, 772.

(35) Maak, F. Untersuchungen Über Die Oxydation von Kupfer-Beryllium-Legierungen Bei Erhöhter Temperatur. *Zeitschrift für Met.* **1961**, *52*, 545.

(36) Gesmundo, F.; Viani, F. Transition from Internal to External Oxidation for Binary Alloys in the Presence of an Outer Scale. *Oxid. Met.* **1986**, *25* (5/6), 269–282.

(37) Payne, M. A.; Miller, J. B.; Gellman, A. J. High-Throughput Characterization of Early Oxidation across $Al_xFe_yNi_{1-x-y}$ Composition Space. *Corros. Sci.* **2015**, *91*, 46–57.

(38) Payne, M. A.; Miller, J. B.; Gellman, A. J. High-Throughput Characterization of the Effects of H_2O Vapour on Early Oxidation across $Al_xFe_yNi_{1-x-y}$ Composition Space. *Corros. Sci.* **2016**, *106*, 61–81.

(39) Payne, M. A.; Miller, J. B.; Oliveros, M. E.; Perez, G.; Gouvea, C. P.; Archanjo, B. S.; Achete, C. A.; Gellman, A. J. Assessment of a High-Throughput Methodology for the Study of Alloy Oxidaition Using $Al_xFe_yNi_{1-x-y}$ Composition Gradient Thin Films. *ACS Comb. Sci.* **2016**, *submitted*.

(40) Payne, M. A.; Miller, J. B.; Gellman, A. J. High-Throughput Screening across Quaternary Alloy Composition Space: Oxidation of $(Al_xFe_yNi_{1-x-y})_{\sim 0.8}Cr_{\sim 0.2}$. *ACS Comb. Sci.* **2016**, *submitted*.

(41) Pettit, F. S. Oxidation Mechanisms for Nickel-Aluminum Alloys at Temperatures Between 900° and 1300°C. *Trans. Metall. Soc. AIME* **1967**, *239* (September), 1296–1305.

(42) Russ, J. C. *Fundamentals of Energy Dispersive X-Ray Analysis*; Butterworths & Co Ltd., 1984.

(43) Boggs, W. The Oxidation of Iron-Aluminum Alloys from 450° to 900° C. *J. Electrochem. Soc.* **1971**, *242* (1961), 906–913.

(44) Dharmaraj, N.; Prabu, P.; Nagarajan, S.; Kim, C. H.; Park, J. H.; Kim, H. Y. Synthesis of Nickel Oxide Nanoparticles Using Nickel Acetate and Poly(vinyl Acetate) Precursor. *Mater. Sci. Eng. B* **2006**, *128* (1-3), 111–114.

(45) Li, X.; Dhanabalan, A.; Wang, C. Enhanced Electrochemical Performance of Porous NiO–Ni Nanocomposite Anode for Lithium Ion Batteries. *J. Power Sources* **2011**, *196* (22), 9625–9630.

(46) Chen, L.-J.; Li, G.-S.; Qi, P.; Li, L.-P. Thermal Decomposition of Ammonium Perchlorate Activated via Addition of NiO Nanocrystals. *J. Therm. Anal. Calorim.* **2008**, *92* (3), 765–769.

(47) de Faria, D. L. A.; Silva, S. V.; de Oliveira, M. T. Raman Microspectroscopy of Some Iron Oxides and Oxyhydroxides. *J. Raman Spectrosc.* **1997**, *28*, 873–878.

(48) Lübbe, M.; Gigler, A. M.; Stark, R. W.; Moritz, W. Identification of Iron Oxide Phases in Thin Films Grown on Al_2O_3(0001) by Raman Spectroscopy and X-Ray Diffraction. *Surf. Sci.* **2010**, *604* (7-8), 679–685.

(49) Schlueter, C.; Lübbe, M.; Gigler, a. M.; Moritz, W. Growth of Iron Oxides on Ag(111) — Reversible Fe_2O_3/Fe_3O_4 Transformation. *Surf. Sci.* **2011**, *605* (23-24), 1986–1993.

(50) Landon, J.; Demeter, E.; Nilay, I.; Keturakis, C.; Wachs, I. E.; Vasic, R.; Frenkel, A. I.; Kitchin, J. R. Spectroscopic Characterization of Mixed Fe-Ni Oxide Electrocatalysts for the Oxygen Evolution Reaction in Alkaline Electrolytes. *ACS Catal.* **2012**, *2*, 1793–1801.

(51) Shi, Y.; Ding, J.; Shen, Z. X.; Sun, W. X.; Wang, L. Strong Uni-Directional Anisotropy in Disordered NiFe2O4. *Solid State Commun.* **2000**, *115*, 237–241.

(52) Ahlawat, A.; Sathe, V. G.; Reddy, V. R.; Gupta, A. Mossbauer, Raman and X-Ray Diffraction Studies of Superparamagnetic $NiFe_2O_4$ Nanoparticles Prepared by Sol–gel Auto-Combustion Method. *J. Magn. Magn. Mater.* **2011**, *323* (15), 2049–2054.

(53) Weimer, A. W.; Arifin, D.; Liang, X.; Aston, V.; Lichty, P. Solar-Thermal ALD Ferrite-Based Water Splitting Cycle. *DOE Annu. Prog. Rep.* **2012**, *II.E.4* (DE-FC36-05GO15044), 64–67.

(54) Laguna-Bercero, M. a; Sanjuán, M. L.; Merino, R. I. Raman Spectroscopic Study of Cation Disorder in Poly- and Single Crystals of the Nickel Aluminate Spinel. *J. Phys. Condens. Matter* **2007**, *19* (18), 186217.

(55) Sundman, B. An Assessment of the Fe-O System. *J. Phase Equilibria* **1991**, *12* (1), 127–140.

(56) Aminzadeh, A.; Sarikhani-fard, H. Raman Spectroscopic Study of Ni / Al_2O_3 Catalyst. *Spectrochim. Acta* **1999**, *55* (Part A), 1421–1425.

(57) Trunov, M. a.; Schoenitz, M.; Zhu, X.; Dreizin, E. L. Effect of Polymorphic Phase Transformations in Al_2O_3 Film on Oxidation Kinetics of Aluminum Powders. *Combust. Flame* **2005**, *140* (4), 310–318.

(58) Zhao, W.; Gleeson, B. Assessment of the Detrimental Effects of Steam on Al_2O_3-Scale Establishment. *Oxid. Met.* **2015**, *83* (5-6), 607–627.

(59) Saunders, S. R. J.; Monteiro, M.; Rizzo, F. The Oxidation Behaviour of Metals and Alloys at High Temperatures in Atmospheres Containing Water Vapour: A Review. *Prog. Mater. Sci.* **2008**, *53* (5), 775–837.

(60) Solferino, G.; Anderson, A. J. Thermal Reduction of Molybdite and Hematite in Water and Hydrogen Peroxide-Bearing Solutions: Insights on Redox Conditions in Hydrothermal Diamond Anvil Cell (HDAC) Experiments. *Chem. Geol.* **2012**, *322-323*, 215–222.

(61) Saleem, S. S. Infrared and Raman Spectroscopic Studies of the Polymorphic Forms of Nickel, Cobalt and Ferric Molybdates. *Infrared Phys.* **1987**, *27* (5), 309–315.

(62) Yi, H. C.; Guan, S. W.; Smeltzer, W. W.; Petric, A. Internal Oxidation of Ni-Al and Ni-Al-Si Alloys at the Dissociation Pressure of NiO. *Acta Met. mater.* **1994**, *42* (3), 981–990.

(63) Heuer, A. H.; Hovis, D. B.; Smialek, J. L.; Gleeson, B. Alumina Scale Formation: A New Perspective. *J. Am. Ceram. Soc.* **2011**, *94*, s146–s153.

(64) Heuer, A. H.; Nakagawa, T.; Azar, M. Z.; Hovis, D. B.; Smialek, J. L.; Gleeson, B.; Hine, N. D. M.; Guhl, H.; Lee, H.-S.; Tangney, P.; et al. On the Growth of Al_2O_3 Scales. *Acta Mater.* **2013**, *61* (18), 6670–6683.

(65) Stott, F.; Wood, G.; Whittle, D.; Bastow, B.; Shida, Y.; Martinezvillafane, a. The Transport of Oxygen to the Advancing Internal Oxide Front during Internal Oxidation of Nickel-Base Alloys at High Temperature. *Solid State Ionics* **1984**, *12*, 365–374.

(66) Park, J. W.; Altstetter, C. J. The Diffusion and Solubility of Oxygen in Solid Nickel. *Metall. Trans. A* **1987**, *18* (1), 43–50.

(67) Gust, W.; Hintz, M.; Lodding, a; Odelius, H.; Predel, B. Impurity Diffusion of Al in Ni Single Crystals Studied by Secondary Ion Mass Spectrometry (SIMS). *Phys. status solidi …* **1981**, *187*, 187–194.

(68) Green, A.; Swindells, N. Measurement of Interdiffusion Coefficients in Co-Al and Ni-Al Systems between 1000 and 1200°C. *Mater. Sci. Technol.* **1985**, *1* (February), 101–103.

(69) Meijering, J. L. Internal Oxidation in Alloys. In *Advances in Materials Research*; Herman, H., Ed.; John Wiley & Sons, Inc., 1971; pp 1–81.

(70) Rapp, R. A. The Transition from Internal to External Oxidation and the Formation of Interruption Bands in Silver-Indium Alloys. *Acta Metall.* **1961**, *9*, 730–741.

(71) Zhao, W.; Kang, Y.; Orozco, J. M. A.; Gleeson, B. Quantitative Approach for Determining the Critical Volume Fraction for the Transition from Internal to External Oxidation. *Oxid. Met.* **2014**, *83* (3-4), 187–201.

(72) Bunn, J. K.; Fang, R. L.; Albing, M. R.; Mehta, A.; Kramer, M. J.; Besser, M. F.; Hattrick-Simpers, J. R. A High-Throughput Investigation of Fe–Cr–Al as a Novel High-Temperature Coating for Nuclear Cladding Materials. *Nanotechnology* **2015**, *26*, 1–9.

(73) Konig, D.; Eberling, C.; Kieschnick, M.; Virtanen, S.; Ludwig, A. High-Throughput Investigation of the Oxidation and Phase Constitution of Thin-Film Ni-Al-Cr Materials Libraries. *Adv. Eng. Mater.* **2015**, 1–9.

(74) Turchanin, M.; Kolchugina, N.; Watson, A.; Kroupa, A.; MSIT®. *The Assessed Phase Diagram of the Al-Fe System*; Effenberg, G., Ed.; SpringerMaterials, 2013.

(75) Saltykov, P.; Cornish, L.; Cacciamani, G.; MSIT®. *The Assessed Phase Diagram of the Al-Ni System*; Effenberg, G., Ed.; SpringerMaterials, 2004.

(76) Priyadarshini, D.; Kondratyuk, P.; Picard, Y. N.; Morreale, B. D.; Gellman, A. J.; Miller, J. B. High-Throughput Characterization of Surface Segregation in Cu_xPd_{1-x} Alloys. *J. Phys. Chem. C* **2011**, *115* (20), 10155–10163.

(77) Russek, S. E.; Bailey, W. E.; Alers, G.; Abraham, D. L. Magnetic Combinatorial Thin-Film Libraries. *IEEE Trans. Magn.* **2001**, *37* (4), 2156–2158.

(78) Chang, K. S.; Aronova, M. A.; Lin, C. L.; Murakami, M.; Yu, M. H.; Hattrick-Simpers, J.; Famodu, O. O.; Lee, S. Y.; Ramesh, R.; Wuttig, M.; et al. Exploration of Artificial Multiferroic Thin-Film Heterostructures Using Composition Spreads. *Appl. Phys. Lett.* **2004**, *84* (16), 3091–3093.

(79) Kölpin, H.; Music, D.; Laptyeva, G.; Ghadimi, R.; Merget, F.; Richter, S.; Mykhaylonka, R.; Mayer, J.; Schneider, J. M. Influence of Si and N Additions on Structure and Phase Stability of $Ge_2Sb_2Te_5$ Thin Films. *J. Phys. Condens. Matter* **2009**, *21*, 1–8.

(80) Oh, B. Y.; Park, J. C.; Lee, Y. J.; Cha, S. J.; Kim, J. H.; Kim, K. Y.; Kim, T. W.; Heo, G. S. Combinatorial Study of WInZnO Films Deposited by RF Magnetron Co-Sputtering. *J. Solid State Chem.* **2011**, *184* (9), 2462–2465.

(81) Heo, G. S.; Park, J. C.; Oh, B. Y.; Kim, S. K.; Lee, Y. R.; Shin, D. C. Combinatorial Growth and Analysis of Ti-In-Zn-O Films Deposited by Radio-Frequency and Direct-Current Magnetron Co-Sputtering System. *Thin Solid Films* **2012**, *520* (24), 7083–7086.

(82) Hu, C.-S.; Luo, Z.-L.; Sun, X.; Pan, G.-Q.; He, Q.; Wen, W.; Zhou, X.-T.; Takeuchi, I.; Gao, C. Strain Induced Metastable Phase and Phase Revolution in $PbTiO_3$-$CoFe_2O_4$ Nanocomposite Film. *Chinese Phys. Lett.* **2014**, *31* (1), 017701.